Kukla, Konrad K. (2010) *Concrete at high temperatures: hygro-thermo-mechanical degradation of concrete.* PhD thesis.

Civil Engineering Department
Faculty of Engineering
The University of Glasgow

Concrete at high temperatures Hygro-thermo-mechanical degradation of concrete

Submitted in fulfilment of the requirements for
the Degree of Doctor of Philosophy

Konrad Kukla

March 2010

Adviser:

Dr. Christopher J. Pearce

"No Damage, No Glory!"

Nenad Bićanić, 2002

Abstract

The main aim of the presented work is the development of a reliable and coherent solution approach to investigate thermo-hygro-mechanical behaviour of concrete, especially under severe heating conditions. The work focuses on the development and extension of an existing analytical, numerical and constitutive model developed at the University of Glasgow. This is then used as a predictive modelling tool to investigate the response of concrete structures subject to combined thermo-mechanical loads.

The thesis focuses initially on the coupled heat and mass transport model. A novel alternative formulation for sorption isotherms, that is applicable to both normal and high strength concrete, is developed. Furthermore, the effect of the slip flow effect is included and several state equations, including relative permeability and saturation vapour pressure, are adopted. Additionally, the effect of polypropylene fibres as a spalling prevention technique is modelled via a modification of the intrinsic permeability formulation. The transport model is further coupled with a damage-based mechanical model for concrete.

The fully coupled thermo-hygro-mechanical model is presented through validation and verification problems and case studies. The model is implemented in a finite element formulation and behaves in a robust manner. The predictions of moisture state for the benchmark problems of drying and heating compare well with experimental results. Classical behaviour associated with heated concrete, such as moisture clog, gas pressure build-up, etc. are all captured by the presented model. The thesis concludes by considering the analysis of prestressed concrete pressure vessel.

Acknowledgement

After putting the last dot in the last chapter, it made me realise that my research would not be as good as it is right now without support and assistance of certain people.

Therefore, I would like to express my deep gratitude to my supervisor Dr Chris J. Pearce, for inspiration and support.

Additionally, help and support of Professor Nenad Bićanić and Dr Colin T. Davie need to be acknowledged and thanked for.

I also wish to thank my colleagues and friends from the Civil Engineering Department of Glasgow University and Halcrow Group Ltd. for advice and moral support.

I also would like to thank my family for a sincere belief in me.

And last but foremost, I dedicate my thesis to my wife, who supported me throughout the entire process of my PhD experience. Without her help and encouragement, this study would not have been completed.

Contents

Contents

Nomenclature

c mass of cement per m of concrete

C_i specific heat of the phase i (for $i = L, S, V$)

D total damage parameter

D_i diffusion coefficient of dry air in water vapor ($i{=}AV$) or water vapor in dry air ($i{=}VA$) within the porous concrete

$\dot{E}_{FW}$ rate of evaporation of free water

H_G enthalpy of gaseous mixture at currnet temperature

H_G^0 enthalpy of gaseous mixture at ambient temperature

h_q convective heat trensfer coefficient

h_{qr} combined convection and radiation heat transfer coefficient

h_r radiative heat trensfer coefficient

$\mathbf{J}_i$ mass flux of phase i (for $i = A, FW, G, L, V$)

K intrinsic permeability of the dry concrete

k thermal conductivity of concrete

k_i relative permeability of phase i (for $i = L, G$)

P_C capillary pressure

P_i partial pressure of phase i (for $i = A, G, L, V$)

P_{Pore} pore pressure, see equation (6.48)

P_{Sat} saturation vapour pressure

Contents

RH relative humidity

R_i gas constant for phase i (for i=A, V)

r^* mean radius of curvature

RVE Representative Volume Element

S degree of saturation with free water

S_B degree of saturation with adsorbed water

SSP solid saturation point

T absolute temperature in K

T_{cr} temperature at the critical point of water $(374.15^{o}C)$

T_{∞} temperature of the surrounding

$\mathbf{v}_i$ component of velocity of phase i (for $i = B, G, L$)

w_1 saturation water content at 298.15K

β coefficient of water vapour mass transfer on the boundary

γ_{wa} surface tension between water and air

$\widetilde{\varepsilon}$ equivalent strain

ε_i volume fraction of phase i (for $i = A, D, FW, G, L, S, V$)

ε_L volume fraction of a liquid water

$\dot{\varepsilon}^c$ creep strain rate

$\dot{\varepsilon}^e$ elastic strain rate

$\dot{\varepsilon}^{ft}$ free thermal strain rate

$\dot{\varepsilon}^{pl}$ plastic strain rate

$\dot{\varepsilon}^{tm}$ thermo-mechanical strain rate

Contents

λ_D specific heat of dehydration

λ_E specific heat of evaporation

μ_i dynamic viscosity of the phase i (for $i = A, G, L, V$)

$\underline{\rho C}$ heat capacity of concrete

ρ_i density of phase i (for $i = A, FW, G, L, S, V$)

$\tilde{\rho}_{G,\infty}$ vapour content of the surrounding

$\widetilde{\rho}_i$ mass of a phase i per unit volume of gaseous material (for $i = A, G, V$)

$\tilde{\rho}_V^0$ initial vapour content

p_{wl} density of water

ϕ concrete porosity

χ thermal damage parameter

ω mechanical damage parameter

Subscripts :

A dry air phase

B physically bound, adsorbed water

D chemically bound water released by dehydration

FW free water

L liquid water phase

M moisture (free water and water vapor phases)

S solid phase

V water vapour phase

1. Introduction

Concrete is the most widely used construction material in the world. Although concrete engineering is more than one hundred years old and concrete is thought to be a well-understood construction material, in the light of recent extreme events, including accidents, arson and terrorism, attention has refocused on the performance of concrete in the fire safety assessment of the buildings and tunnels. The exposure of concrete to high temperature can jeopardise significantly the structural integrity and load bearing capacity of the structure. Fire represents possibly one of the most severe conditions encountered during the life-time of a structure and, when all other measures for containing a fire have failed, structural integrity represents "the last line of defence" [43]. Thus, the provision of appropriate safety measures is one of the most important requirements in modern structural design. Therefore, it is necessary that the designer is provided with all the required information on behaviour of concrete exposed to elevated temperatures.

In fire engineering, the severity of fire is measured in terms of the burn time and the maximum temperatures achieved, which can be up to 1400°C under certain conditions. These conditions are determined by fire compartment parameters, such as geometry, ventilation and thermal properties. Additional conditions are distribution, amount and nature of fuel. All of the above may lead to concrete temperatures of over 1000°C in the surface layers of concrete. Although concrete compares well to other construction materials such as steel or timber in fire performance, when comparing combustion and thermal diffusivity, exposure to elevated temperatures results in degradation of its mechanical properties and reduction of cross-section area through spalling. Spalling ranges from superficial damage of surface layers

1. Introduction

to explosive events leading to extensive loss of material and exposure of reinforcement, and therefore remains one of the main issues to be addressed in the case of building and tunnel fires. For example, during the 1994 Great Belt tunnel fire, up to 75% of the lining thickness of the concrete segment was lost in multiple layered explosive spalling (see Figure 1.1). Also the Channel Tunnel fire in 1996 (see Figure 1.2) demonstrated the structural, safety, and economic consequences of a 10-h fire that reached temperatures of 1000°C, when thermal spalling of the concrete liner resulted in severe structural damage over a significant length of the tunnel. The liner surface was delaminated almost 200 mm deep and the steel reinforcement lost up to 40 % of its yield strength due to the heat. After subsequent investigations, no real consensus emerged as to the exact mechanism underlying the observed spalling phenomenon. However, it is widely agreed that the behaviour of concrete under severe heating is greatly dependent on its composite structure and in particular on the physical and chemical composition of the cement paste and the type of concrete used. Explosive spalling is significantly more likely to occur in High Strength Concrete, due to its dense micro-structure and thus, low permeability [50]. This parameter results in reduced fluid transport under fire conditions, which increases pore pressures and the risk of spalling. Therefore, the importance of the transport of fluids needs to be highlighted. Additionally, it can be stated that High Strength Concrete has enhanced mechanical properties, but reduced fire performance comparing with Normal Strength Concrete.

When concrete is exposed to high temperatures, fluid evaporates and it is transported away from the heat source and then it re-condenses in the cooler region. The concrete ahead of the drying front rapidly becomes over-saturated and forms a "moisture-clog", according to Harmathy [29], which inhibits the escape of the subsequent water vapour from the advancing drying front. Consequently, there is a rapid built-up of vapour pressure ahead of the drying front. Depending on the rate of heating, permeability and many other factors change and as a result tensile strength can be exceeded by the vapour pressure, which can lead to progressive fracturing of the concrete layers away from the bulk material. It is argued that high pore pressures act only as the trigger for the explosive spalling and do not necessarily provide the energy for the explosion. This reasoning is based

Figure 1.1.: The Great Belt tunnel lining damaged after the 1994 fire

on the fact that when a crack initiates there is a sudden increase in pore volume and thus an equally sudden decrease in pore pressure. The required energy for the explosion is supplied by the stored strain energy associated with the thermal strains [7].

To summarise, following Khoury et al.[40] it can be stated that the two important phenomena which need to be addressed, when concerned about an explosive spalling of concrete at high temperatures, are the moisture state and the mechanical behaviour of the concrete at elevated temperatures. That is why when modelling concrete, it is necessary to incorporate not only the mechanical and thermal responses, but also the changes in content, flow intensity and diffusion of all present fluids, including evaporation and condensation.

Literature overview. Recently, there have been significant efforts in computational modelling of concrete at high temperatures, which are presented in this section, but there are still very few simulation codes which are capable of predicting the coupled thermal hygral and mechanical behaviour of concrete structures.

Figure 1.2.: Chanel Tunnel after 1996 fire

One of the most important early publications, which considered transport alongside thermo-mechanical modelling is Bazant's publication from 1997[5], which follows [7]. It presents the evolution of distributions of pore pressure and thermal stresses in rapidly heated concrete. The difficulties, which are caused by the jumps in permeability and water content under thermal gradients, are discussed in detail. Additionally, the mechanisms of explosive spalling are discussed and conclusions are made to the pore pressure influence. As a result, the role of pore pressure is considered to be a trigger in explosive thermal spalling of high strength concrete. Bazant argues that the main driving force during this process is the release of the stored energy due to the thermal strains. Therefore, the author considers that coupling with damage or fracture mechanics is necessary to describe the full process. The paper is finalised with an introduction of a simplified analysis of pore pressure distribution, based on the calculations of the movement of the drying and wetting fronts.

Among the most important contributions is the model developed by Tenchev et al. [65]. This approach is comprehensive and is fully generalised for 3-D. However, it includes some strong assumptions and excludes various

phenomena that might be vital for this kind of analysis, which will be explored in detail in this thesis. First, because of the simplified assumption that pore and liquid pressures are equal, the capillary pressure, by definition, is always equal to zero. However, despite the above definition, the model employs a constant of small value for the relative permeability of the liquid phase, in case of initiation of the effect of capillary suction on moisture transport. In addition to these inconsistencies in Tenchev's model, the absorbed water flux is ignored. This can be a significant factor [15], although the flux may be low when considering the overall transport of moisture in concrete. These issues will be discussed in greater detail later in the thesis. Nevertheless, despite Tenchev's model assumptions, its contribution is significant and results in a finite element formulation, which can be easily used and developed.

The Tenchev's model was the foundation for the Glasgow model, presented by Davie et al.[15]. The modifications and improvements of the Glasgow model focused on improving the mechanical and hygral formulations. The mechanical formulation was not considered in the original Tenchev's model. Therefore, an extension to mechanical damage was introduced here to capture spalling phenomena. A detailed description of this extension is presented in Chapter 6 of this thesis.

Tenchev's assumption that the capillary pressure $P_C = 0$, restricts its application to rapid heating. The Glasgow model significantly enriched the fluid transport component of Tenchev's model with consideration of both capillary pressure and adsorbed water flux. One consequence of these modifications is that a broad spectrum of heating scenarios can be considered. However, one of the crucial aspects of both models is that they make use of the sorption isotherms proposed by Bazant [7], which are derived under specific assumptions and restricted to normal strength concrete. Further extension of the Glasgow model to account for more generalised sorption isotherms was the basis for the work presented in this thesis.

Gawin et al.[22, 23, 24, 25, 27] proposed a more sophisticated model for the analysis of deformations of concrete subjected to transient temperature and pressure. The multi-physics model has been developed in stages over several years and it considers chemical, hygral, thermal and mechanical aspects. The proposed constitutive model includes both thermo-chemical

1. Introduction

and mechanical damage and it is introduced into a general coupled mathematical model of hygro-thermo-chemo-mechanical behaviour of concrete structures. The performance of the model was demonstrated in simulating the thermo-mechanical loading of concrete cylinders. The model allows for a realistic risk assessment of thermal spalling. It considered the effects of pore pressure build-up and accumulation of strain energy, together with material degradation and cracking. There is a good agreement between numerical simulations and experimental results. However, in the model one of the primary variables is capillary pressure, which causes some problems in the situation of elevated temperatures. At the critical point of water ($T>T_{crit}$), there is no capillary water in the pores of concrete and only the gas phase of water exists. Consequently, at that stage there is no capillary pressure. This problem was overcome in a pragmatic way, but the authors explanation in not altogether clear. The mathematical model presented by Gawin et al. for analysis of hygro-thermo-chemo-mechanical behaviour of concrete, as a multi-porous material at high temperatures seems convincing and numerical simulations shows good accordance with presented experimental results.

Khoury et al. [40] developed a model called HITECO as part of the European research project entitled 'Understanding and industrial application of High Performance Concretes in High Temperatures Environment'. The authors concentrated on the physical model more extensively, providing an interpretation of the physical meaning of the transport mechanism, phase changes, and mechanical properties involved in the process. The mathematical model presented is largely similar to those of Gawin [22, 23, 24, 25, 27]. In conclusion, the publications of Khoury and Gawin together formulate a good scheme for such problems. The model discussed in those publications shows reasonable prediction of the behaviour of concrete at high temperatures, in general, and in particular for the assessment of explosive spalling.

Recently, Gawin et al. [26] present a reduced version of their model, whereby the fully coupled hygro-thermo-chemo-mechanical model is simplified and some quantitative assessment of the risk of spalling is shown, with comparison to experimental results.

Another recent paper on this subject, by Chung & Consolazio [12], represents an important contribution. In this publication, the development of a finite difference model that simulates coupled heat and mass transport

in reinforced concrete exposed to fire is presented. This thermo-hygro-mechanical model for concrete is comprehensive, but only few numerical problems are discussed. Some of the associated ideas presented are further discussed in this thesis as alternatives to existing solutions.

More recent paper by Dwaikat and Kodur [18] represents an interesting and potentially important attempt to develop a simplified thermo-hygral model for concrete subject to fire conditions. The authors are clearly stating that the simplified model is presented to make a more tractable framework for practical applications. A short list of the existing models, similar to the one introduced above, is presented and discussed. In conclusion, an explicit statement is made on the applicability of the model and better practicality than the listed existing models. However, it is not clarified whether and why the proposed model is superior to the existing models, especially that it does not take into account the mechanical component.

Engineering practice. A different point of view on the subject is presented in the Eurocodes. In parts of the various material codes related to fire situations, like EN 1992-1-2, EN 1993-1-2 or EN 1994-1-2, fire resistance may be determined through either simple calculations, advanced models or tabulated data. The specific requirements are regulated using National Annexes, based on the type and height of the structure. The proper design procedure provided in the Eurocodes is based on various standards, as presented in the Algorithm 1.1. First the designer has to consider a design fire scenario that is appropriate to a considered fire situation, which provides a design fire load. Next, the structural applied load for the fire limit state needs to be determined. This is followed by the calculation of the load effects at the fire limit state. All these steps determine the relevant dimensions to meet the requirements identified previously.

The presented algorithm provides, for simple calculation methods, an estimate of the deterioration in material properties at elevated temperature together with an estimate of the fire loading for the fire limit state. The resistance of the material is calculated based on the reduction factors appropriate to the design thermal exposure and compared to the load effects present at the time of fire.

Advanced computational methods, typically involve the use of finite ele-

Algorithm 1.1 Simplified fire design procedure based on BS EN 1992-1-2:2004
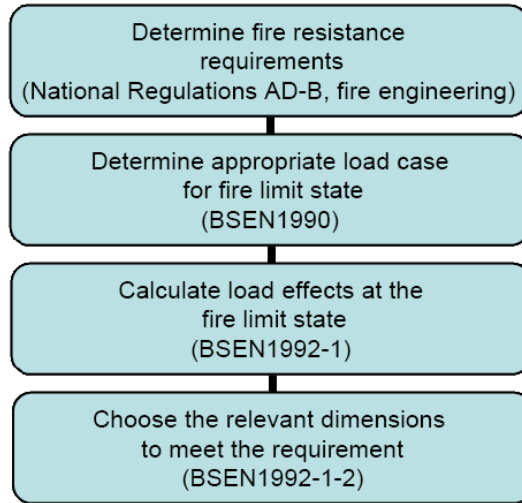
ment models with thermo-mechanical response, with input parameters based on the simpler calculation requirements. The influence of moisture content and its migration is suggested to be neglected. Explosive spalling is considered to be avoided by setting appropriate initial conditions requirements for moisture content to a low value, which is specified in UK National Annex to be 3%.

This assumed approach is claimed to be of a conservative nature. However, the underlying transport phenomena are neglected and it is questionable whether this approach might be fully able to capture all the important physical aspects of the system. In addition, as build-up of gas pressure is suspected to play a significant role in the concrete failure modes when exposed to fire conditions it seems important to include the effect of moisture in the modelling approach. Furthermore, the Eurocodes do not require coupling of the thermo and mechanical performance.

Summary and motivations. Spalling of concrete remains one of the main issues to be addressed in the case of fires in buildings and tunnels. Successful modelling of this phenomenon depends not only on the accurate prediction of the temperature distribution in structural concrete but on its mechanical response to the heating and boundary restraint conditions and the migration of moisture and associated pore pressures.

Furthermore, in nuclear reactor vessels, concrete provides additional protective barrier, which during accidental conditions, when the pressure vessel liner is compromised, can slow down radiation effects. In essence, concrete acts as a biological shield. In order to achieve proper design and construction it is necessary to know the moisture state of the concrete within the nuclear pressure vessel under both service and accident conditions. The maintenance of its shielding performance is important throughout the whole life of the structure.

In order to fully understand both of these phenomena, it is vital to understand all the mechanisms taking place and their complex interactions. That is why, the main focus of this thesis is the development of a reliable but straightforward solution approach to investigate thermo-hygro-mechanical behaviour of concrete, especially under severe heating conditions. The development and extension of the existing analytical, numerical and constitutive 'Glasgow' model from Davie et al.[15] is presented and used to calculate the distribution of primary variables, strains and stresses to produce the response of the structure under fire conditions or from severe heating to elevated temperatures. The presented model will be referred to as the 'Enhanced Glasgow model'.

Additional motivation is focused on the design of the optimal material meso-structure and, as a consequence, the design of new materials. One of the examples presented in this thesis in Chapter 5 is the introduction of polypropylene fibres into the concrete mix. As a result, concrete permeability is altered during fire conditions, which reduces the possibility of explosive spalling. The Enhanced Glasgow model, presented in this thesis, is expected to be a useful tool in a process of the design of new materials with optimised meso structure under extreme heating conditions.

It will be demonstrated that the theoretical background for the model is based on the work of Davie et al. [15], Tenchev et al. [65], Bear [8] and Bachmat [9], and influenced by the works of Schrefler, Gawin and Khoury [23, 40, 63].

Outline of the thesis. The motivations, mentioned in this chapter, are followed by an overview of concrete and its behaviour at elevated temperatures in Chapter 2. There is also an introduction to modelling of such phenomena

using a continuum approach. The detailed description of the transport model is provided in Chapter 3, where the principal research contributions of this thesis are presented (Section 3.4). The important validation process is based on a benchmark problem of heated concrete and experimental problems of drying and heated concrete, as presented in Chapter 4. This is followed by an extension of the material model to concrete with polypropylene fibres in Chapter 5. The discussion of existing spalling prevention solutions, experimental work and a numerical example are provided in the same chapter. Chapter 6 provides the description of the mechanical part of the formulation with a focus on damage mechanics and coupling of the mechanical model with the thermo-hygral model. Consequently, Chapter 7 provides additional computational examples using the full Enhanced Glasgow Model. The first example (Section 7.1) is a prediction of fully coupled thermo-hygral and mechanical behaviour of concrete column during fire. The second one (Section 7.2) is a two-dimensional numerical prediction, examined this time through the life cycle of a concrete pressure vessel from nuclear reactor during real life work conditions.

Conclusions and possible future research directions are presented and discussed in the final Chapter 8.

2. Concrete at high temperature

Concrete, under normal atmospheric conditions, is typically exposed to temperatures below 50°C. However, in fire conditions, concrete can be exposed to temperatures of up to 1200°C in less than 2 hours. The intensity and severity of exposure depends on type of fire, the type and size of structure and whether the fire is localised or fully developed. For fully developed building or tunnel fires, standard fire curves are representative for design purposes. The standard time/temperature curve is provided by national (in the UK BS476) or European (EN 13501) standards and it is presented in Equation (2.1) and Figure 2.1, where Θ_g is the gas temperature in °C and t is time in minutes.

$$\Theta_g = 20 + 345 log_{10}(8t + 1) \qquad (2.1)$$

It can be clearly seen that the design curve reaches 1000°C in less than 90 minutes. Therefore, the response of the structures under such fire conditions is of a great importance for engineers.

However, some structures can be regularly exposed to high temperatures as part of the functional requirement (in power plants, refineries) or the exposure time may extend beyond several hours (fires in tunnels). Therefore, it is important to be able to predict not only immediate behaviour of the structure, but also the long time thermo-hygro-mechanical state and provide enough information about changes in material properties and the mechanisms causing those changes. The obtained information can give a
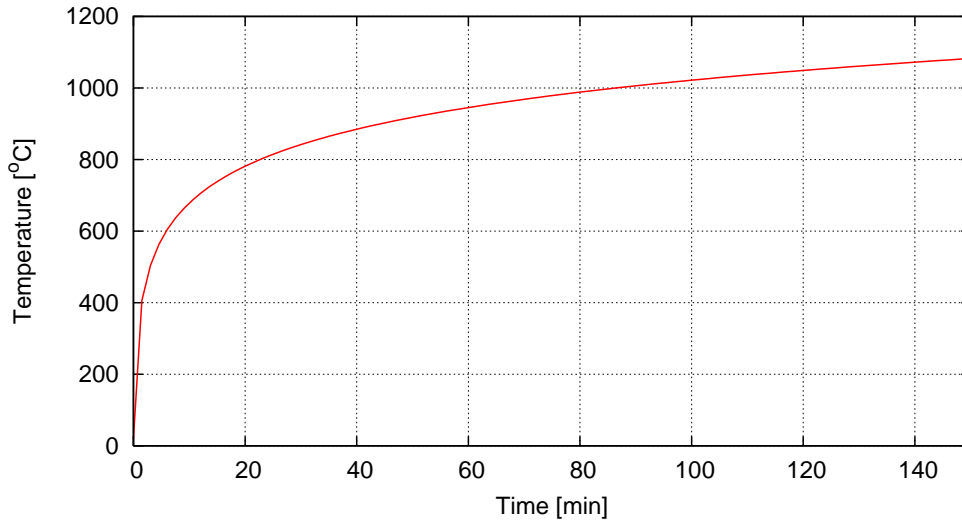
Figure 2.1.: Standard fire curve

valuable insight into future design of new materials and structures. Consequently, such design methods could be also used during refurbishment or renovation of the existing structures.

That is why it is important to identify and understand the physical and chemical processes that occur in concrete. Consequently, in this chapter the important material factors that affect concrete behaviour are discussed, especially the behaviour at elevated temperatures. The understanding of these processes is than incorporated into introduction of concrete modelling.

2.1. Properties

Concrete is a complex composite material and consists mainly of aggregates bonded together by a softer matrix of hardened cement paste surrounding the aggregates in a weak inter-facial transition zone. Its structure is highly porous containing up to 40% of capillary pores, which are between 1nm to 1mm in diameter, and up to 28% gel pores, which are typically less than 2.6 nm in diameter [52]. Those pores can be fully or partially filled up with dry air, adsorbed water, free water or water vapour.

During hydration and hardening, concrete develops certain physical and chemical properties. The mechanical strength and durability are considered to have an important role in the design process. By the definition propo-

sed by the American Concrete Institute, concrete durability is its resistance to weathering action, chemical attack, abrasion and other degradation processes.

Concrete properties and concrete response to the influencing factors, such as loading, temperature and moisture, depend on the properties of the concrete constituents. It can be stated that the concrete micro structure derives its macro properties through combined properties of different aggregate types and the cement paste. The large number of different aggregate types are suitable to be used within concrete maintained under ambient temperatures. However, during fire conditions, when heat is conducted and advected, many changes occur in a physical structure, chemical composition and fluid content. Therefore, the mechanical properties of concrete, in particular strength and stiffness, when exposed to high temperatures are significantly altered. This is discussed in the following sections.

Generally, it can be said that concrete has good properties with respect to fire resistance. As an example, concrete is non-combustible and it does not emit toxic fumes. Additionally, it has a resistance to flame penetration as well as lower heat conductivity than alternative construction materials like steel or timber and as such it is being used as a protective layer for structural steel. However, the high temperature gradients and the hygral conditions introduced during fire conditions, can result in concrete spalling, which is discussed in detail in section 2.1.4. Consequently, the reduction of cross-section area results in reduced load-carrying capacity and potentially structural failure.

Therefore, a short description of all processes, which occur during severe heating scenario are discussed in the next section. It is followed by a review of relevant material properties, which are separated into two groups. The physical and thermal properties are discussed together as they are independent of loading history to some extent. This is followed by mechanical properties, which influence the stress state of the material. Afterwards, concrete failure mechanisms are presented and discussed.

2.1.1. Brief description of processes during heating

The compatibility between the cement paste and the different types of aggregates at ambient temperatures, is distorted when exposed to high temperatures. Following Bazant and Kaplan [7], it is possible to distinguish several stages for a Portland cement based concrete made with quartzite, limestone and basalt aggregates, when exposed to fire conditions.

The first process is water evaporation at about 100°C, which is followed by the dehydration of cement gel at about 180°C, that weakens the bond within the solid skeleton. The decomposition of concrete binding product, calcium hydroxide, into calcium oxide and water, which starts at around 400°C, is a reversible process that is most rapid at 500°C. These are followed by expansion due to the $\alpha - \beta$ inversion of silicon dioxide within quartzite and basalt aggregates, or due to thermal incompatibility of the limestone constituents, which occur between 450°C and 700°C. These transformations cause a volume increase through thermal expansion of aggregates. These processes are followed by the decomposition of the calcium silicate hydrates in cement paste starting at 700°C. Finally, the decarbonation of concrete and melting of the aggregates is the last stage at the level of 800°C. The melting reaction is most evident in the quartzite and basalt aggregate concretes.

Alternatively, all the processes can be briefly described from physical point of view. Therefore, during the high temperature exposure, heat is transported by conduction and advection within the porous medium and by convection and radiation at the external surfaces. This results in an increase of the temperature, starting from the heat source inwards. This leads to changes in the pore structure and hence also to its physical structure with respect to time. All of these processes are strongly influenced by the actual loading as well as by the moisture content and temperature profiles. The physical properties of the fluids inside the concrete pore structure are temperature dependent and both liquid water and gas are transported due to pressure driven flow (Darcy flow) and concentration driven flow (Fick's flow). During the hydration and dehydration processes, large quantities of heat are absorbed and released by concrete. The permeability, which depends on moisture content, temperature gradient and the pore structure itself, increases suddenly over 160°C, due to these significant changes. Therefore, the mechanical properties are altered and structural integrity can be

compromised.

2.1.2. Physical and thermal properties

The thermal and physical properties of concrete are important for a variety of reasons. Thermal conductivity and diffusivity are important when the development of temperature gradients, thermal strains and cracking are considered. The knowledge of specific heat is required when thermal insulation of concrete is relevant. The thermal expansion of concrete is relevant during the assessment of thermal gradients, as well as during the design processes of expansion and contraction joints. All these properties need to be known when the effects of fire are considered.

Therefore, this section describes the bulk physical and thermal properties of concrete, rather than its constituents, when exposed to elevated temperatures.

Density of concrete decreases slightly with increasing temperature. When concrete is heated, there is a loss in weight caused by the evaporation of both free and combined water. However, following Purkiss [60], this loss is not generally considered to be enough to cause substantial changes in density. Therefore, for structural calculations the density of concrete must be taken as its ambient value over the entire temperature range. For thermal calculations, some guidance is suggested in Eurocode 2 [1]. The variation of density with temperature is presented in section 3.3.2 of [1] and it is described to be influenced by water loss and is defined as set of four linear functions for range between 20°C and 1200°C.

Specific heat capacity is the measure of the heat energy required to increase the temperature of a unit mass of a material by 1°C. Following Neville [52], it is noted that the different types of aggregate have little affect on concrete specific heat. However, it is considerably increased by an increase in the moisture content. Additionally, it is known that the specific heat increases with increase in temperature and with decrease in concrete density.

Thermal conductivity is a measure of the ability of the material to conduct heat and is defined as the ratio of the flux of heat to temperature gradient. It is predominantly affected by the aggregate type and the moisture content. Due to the fact that air has a low conductivity, the saturated concrete has higher conductivity. Additionally, the conductivity of water is half of the conductivity of the cement paste, so the lower the water cement ratio in the mix the higher the conductivity of the hardened concrete. A detailed formulation, that depends on the aggregate types is presented in Appendix D.

Thermal diffusivity represents the rate at which temperature changes within a mass can take place and it is relevant to the thermal conductivity, density and heat capacity. It determines the temperature gradient during transient heating problem. Following Neville [52], this is defined as:

$$\delta = \frac{k_{eff}}{\rho C} \tag{2.2}$$

Coefficient of thermal expansion depends on both the composition of the mix and on its hygral state at the time of the temperature change. Concrete, as with most engineering materials, has a positive coefficient of thermal expansion. The influence from the mix proportions of the concrete arise from the fact that both the cement paste and the aggregates have dissimilar thermal coefficients. Following Neville [52], the linear coefficient of thermal expansion of hydrated cement paste varies from about $11 \cdot 10^{-6}$ to $20 \cdot 10^{-6}$ per °C and generally it is higher than the coefficient of aggregates. The temperature dependent variations of coefficient of thermal expansion is presented in Figure 2.2, which is reproduced after Purkiss [60]. It can be noted that it is not linear with respect to temperature.

2.1.3. Mechanical properties

This section presents concrete mechanical properties at high temperatures. They are usually described by elastic stiffness, compressive strength, tensile strength and fracture energy. The full material behaviour can be characterised by a constitutive law of stress-strain relationship, which can provide
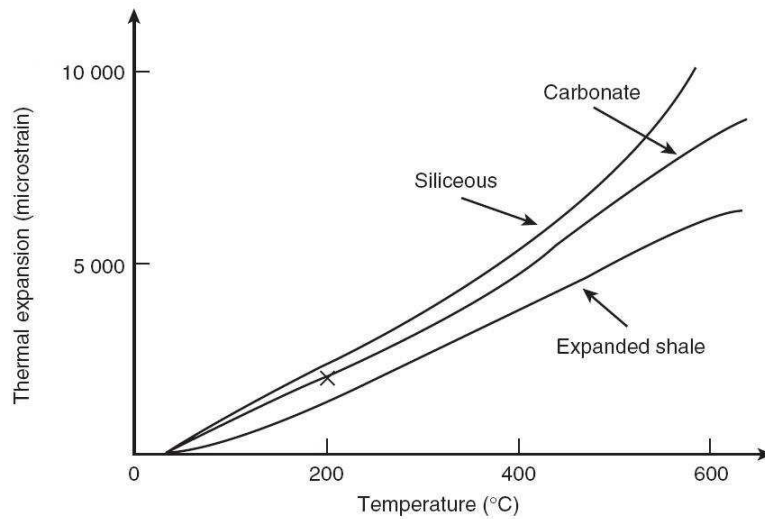
Figure 2.2.: Thermal expansion reproduced after Purkiss [60]

full concrete behaviour at elevated temperatures. Additionally, strains are influenced by shrinkage and creep.

Young's modulus. The modulus of elasticity of concrete is strongly affected by temperature. With reference to Neville [52], the pattern of influence of temperature on the modulus of elasticity is shown in Figure 2.3. There is little change in this modulus up to the temperature of around 100°C, but it starts to reduce when the temperature is in excess of 120°C. This reduction might be connected with the evaporation of liquid, which may lead to the relaxation of bonds and damage induced by the thermal incompatibilities between the aggregates and the cement matrix. When the specimen is pre-loaded during the heating cycle, it is noted that the temperature effects on Young's modulus are smaller [60]. Such results can be seen in Figure 2.4, which is extracted from Nielsen and Bicanic [53]. These effects might be explained due to the pre-stress effects that keep the cracks closed.

Stress-strain effects. According to Purkiss [60], the first researcher to establish the complete stress–strain curve for concrete under temperature loading was Furamura (1966), whose results showed that, besides the compressive strength and elastic modulus being reduced, the slope of the descending branch (i.e. ductility) of the curve is also reduced. The reproduction
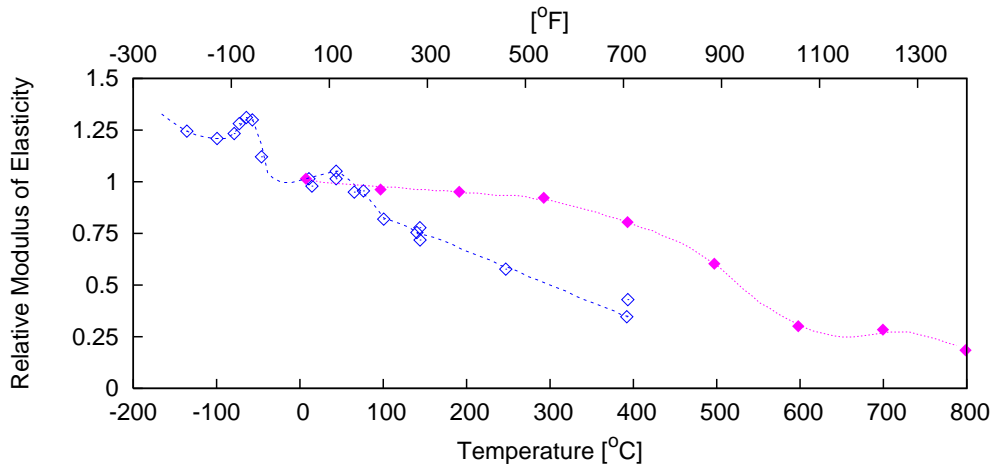
Figure 2.3.: Modulus of elasticity changes due to rise in temperature, reproduced from Neville [52]

of these stress–strain curves can be seen in Figure 2.5. The stress–strain curve is affected by the aggregate-cement ratio and aggregate size. Similarly to Young's modulus effects, the specimen, when pre-loaded during heating cycle, is less affected by temperature.

Tensile strength and fracture energy   There are limited data available on tensile strength whether based on direct tensile strength or splitting strength. Following Stabler [64] early works by Thelandersson and Harada can be presented as an example of cylinder splitting tests of pre-heated concrete. However, these tests were carried out after the concrete had cooled down to room temperature. Recently, works by Felicetti and Gambarova [19] indicate that for direct tension tests, the tensile strength at 600°C drops linearly to about a quarter of the ambient strength. Additionally, the fracture energy is defined as the area under the stress-displacement curve over a crack. Therefore, the tensile strength test provide the fracture energy information. As an example, the experiment carried out at Glasgow University as part of an MAECENAS EU project [73] for high strength concrete with a basalt aggregate indicate a phenomenological dependency of the fracture energy on temperature.

Creep and shrinkage.   Under a constant sustained load, the initial instantaneous elastic deformations are followed by gradual increase. This effect
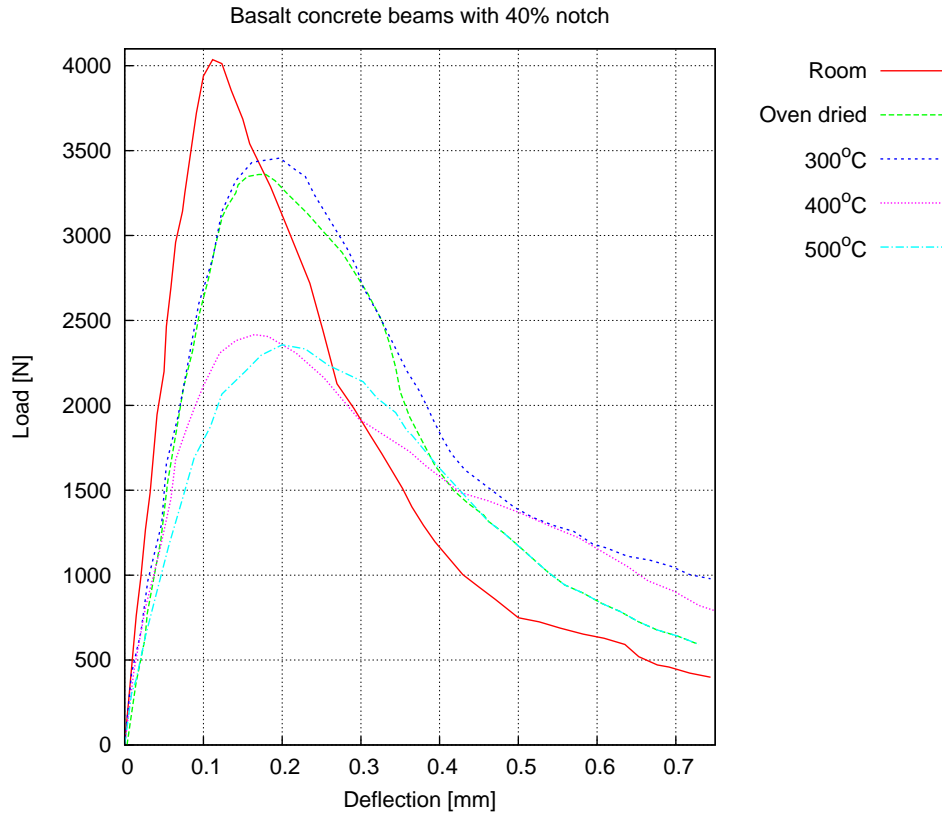
Figure 2.4.: Residual load vs. deflection curve for various maximum temperatures, reproduced from Nielsen and Bicanic [53].

is called creep and at ambient temperature, can be defined as the increase in strain under a sustained stress. The creep of concrete at elevated temperatures is very much greater than that at ambient conditions, due to the additional creep mechanisms. Therefore, a careful consideration must be taken in the analysis of safety related concrete structures, like in the nuclear industry.

In addition to that, concrete gradually shrinks as a result of drying, which in turn can be induced by heating. These time-dependent deformations are larger than the initial elastic deformations.

Creep can be categorised as basic creep, drying creep and transient thermal creep. Drying creep is associated with strain induced shrinkage. The transient thermal creep corresponds to thermally induced deformations under load. Creep strains at different stress levels and temperatures are shown in Figure 2.6, where the results of Anderberg and Thelandersson (1976) are
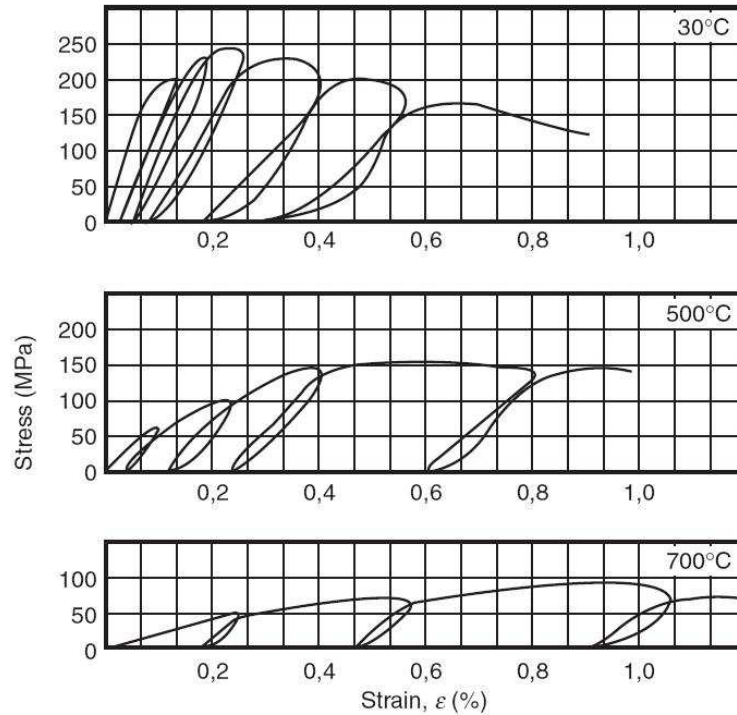
Figure 2.5.: Stress–strain curves for concrete with no pre-load at elevated temperatures (Furamura, 1966), reproduced from Purkiss [60].

reproduced after Purkiss[60].

2.1.4. Failure of concrete when exposed to elevated temperatures

In the event of fire, concrete structures are affected by various processes, as described previously in section 2.1.1. This leads to degradation of the material and potentially spalling of the near-surface concrete layers. Depending on its origin, spalling can be classified [71] into:

1. aggregate spalling (splitting of aggregates)

2. corner spalling (i.e., corners of columns or beams fall off)

3. surface spalling (surface layers of concrete fall off or burst out of the structural element),

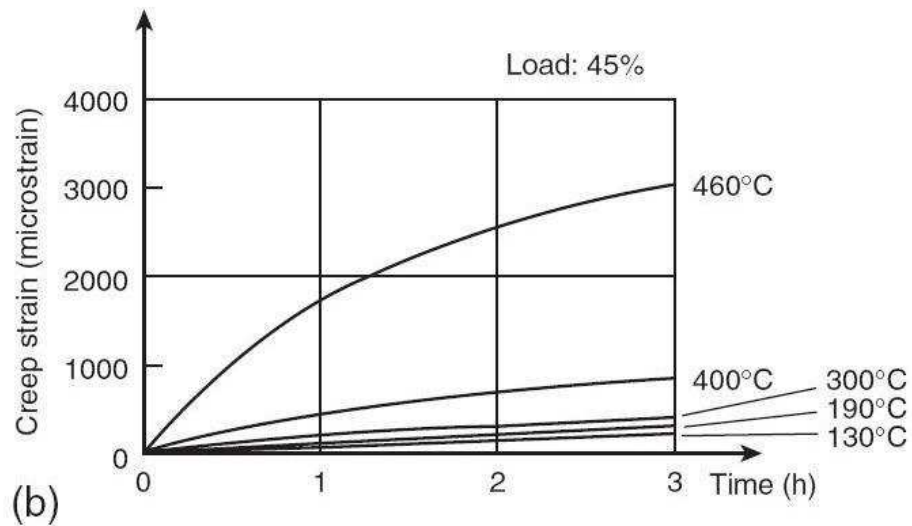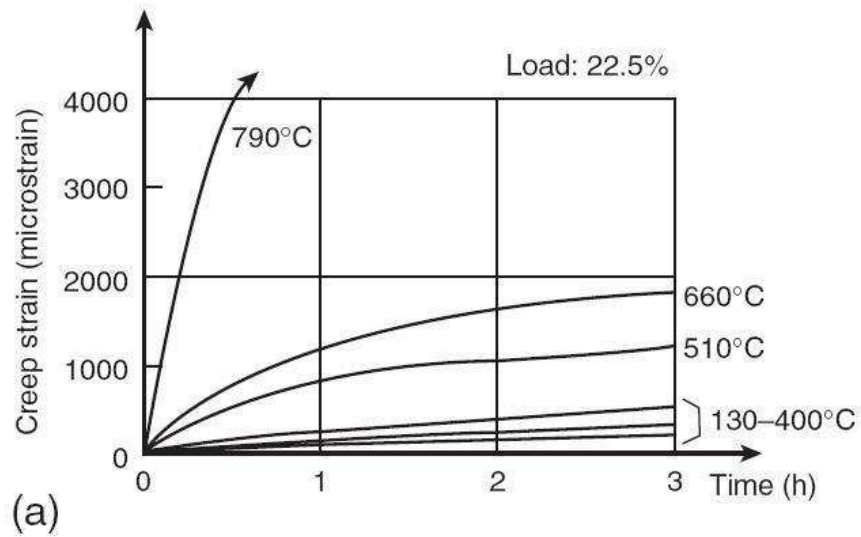and based on physical mechanisms, spalling can be divided into:

Figure 2.6.: Isothermal creep data for concrete at elevated temperatures reproduced after Purkiss [60]

2. Concrete at high temperature

1. progressive spalling (or sloughing-off, where concrete pieces fall out of the structural element)

2. explosive spalling (violent burst-out of concrete pieces characterised by sudden release of energy).

Spalling has been studied for several years, both experimentally and theoretically, but there is still a lack of full understanding of this important phenomenon. Nonetheless, it is believed that there are two aspects driving spalling. On the one hand, the thermal stresses resulting from high strains caused by high temperature gradients (e.g. [5, 39, 35, 67]). On the other hand, the build-up of high pore pressure close to the heated surface as a result of a vaporisation of water (e.g. [33, 12, 35]). During the fire situation, the combined action of pore pressure and thermal stresses results in explosive spalling. Cracks develop parallel to the surface when the sum of the stresses exceeds the tensile strength of the material. As a result, a sudden release of energy and an uncontrollable failure of the heated surface region take place. An example of such combined effects is illustrated in Figure 2.7.

The up-to-date results of the afore-mentioned research show that there are several factors that affect HSC more than NSC, mainly due to permeability effects. Among others, initial moisture content, porosity and permeability of concrete, type of aggregates, shape and dimensions of structures seem to be playing a significant role in these phenomena, as well as concrete strength (both compressive and tensile) and the rate of temperature increase. Based on recent experimental results (see Figure 2.8) by Zeiml et al.[71] the origin of spalling is still open for debate. According to some numerical studies (e.g. [24]) the thermo-mechanical processes are considered to initiate cracking and spalling, but the driving force, or the biggest contributor in the acceleration of spalled-off pieces seems to be the gas pressure that is built up from liquid during heating, which is called the thermo-hygral process. However, work done by Bazant [6] seems to lead to contradictory conclusions, that the thermo-hygral process triggers the fracture and crack opening, but this leads to release of gas pressure. Therefore, the thermo-mechanical part of this behaviour plays a crucial role in explosive spalling. Nonetheless, there is no consensus as to, which of these processes represent principal drivers, but as it is important to be able to predict all of these phenomena, an

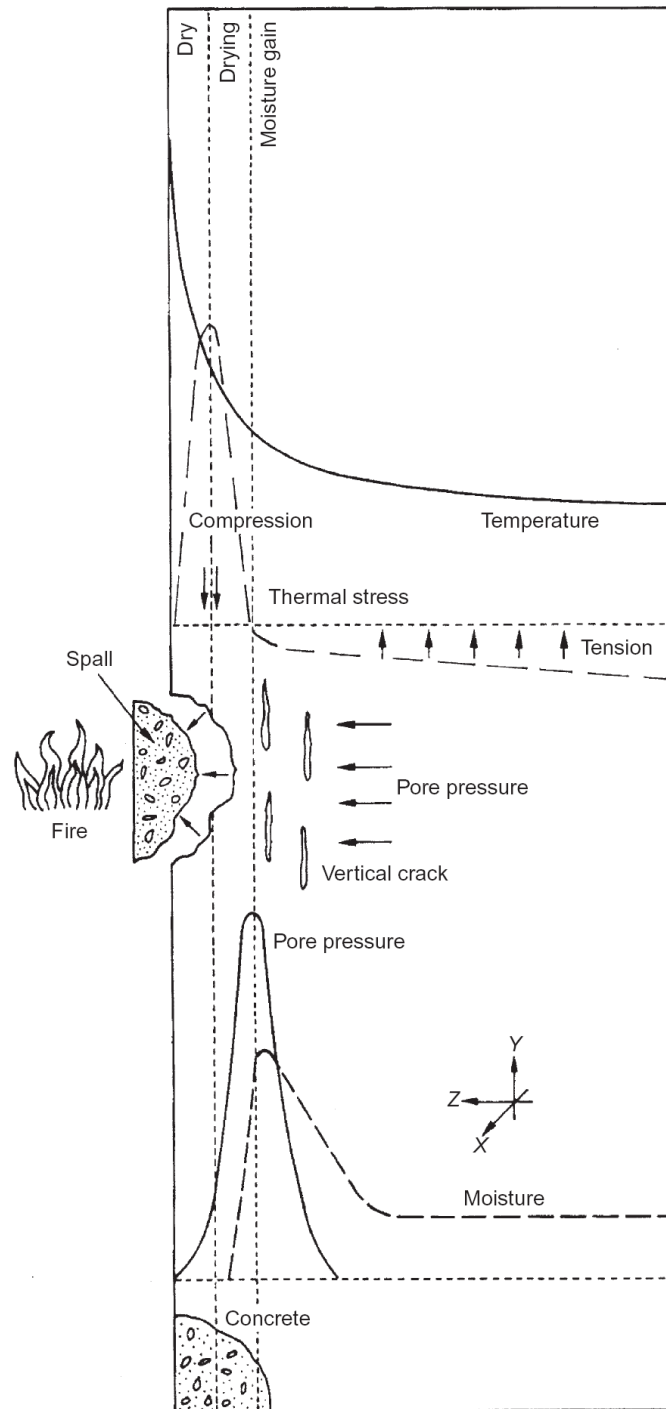Figure 2.7.: Combined pore pressure and thermal stress spalling mechanism extracted from Khoury [36]
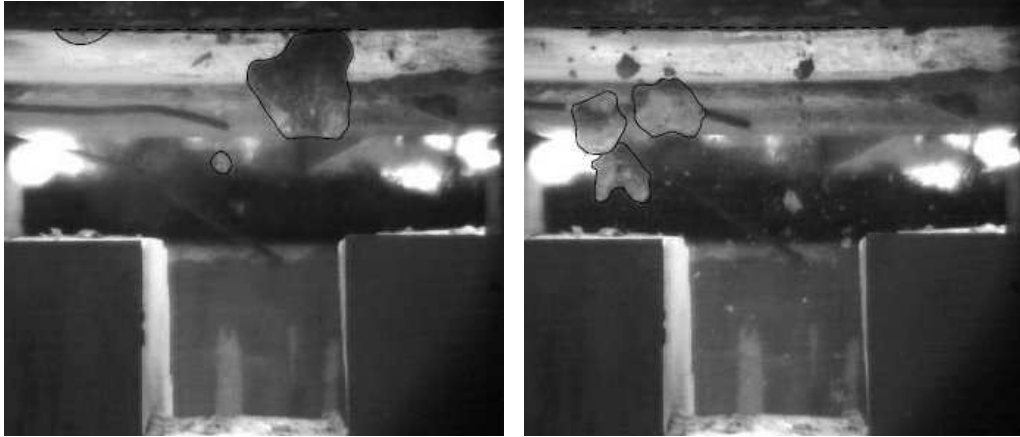
Figure 2.8.: High-speed camera images from spalling experiment at 12 ms (left) and 160 ms (right) from Zeiml and Lackner [71]

appropriate thermo-hygro-mechanical model needs to be considered.

2.2. Modelling

As already stated, the objective of this thesis is to develop a mathematical model of a multi-phase continuum that describes heat transfer, mass transport and mechanical behaviour in heated concrete at macroscopic level. The description of the hygro-thermo-mechanical behaviour of concrete will be within a multiphase porous medium framework. Therefore, the introduction to this approach is presented in the next section. This is followed by the formulation of the mathematical model, where the full set of equations is introduced.

2.2.1. Modelling concrete as a porous medium

It has already been mentioned that concrete has a very porous structure and therefore, it should be modelled as a porous medium. Consequently, an introduction to modelling of porous media is presented in this section.

There is a large variety of natural and artificial porous materials, including soil, sand, rock, ceramic, foam, rubber, bread, bones and concrete. The porous material consists of the main part of the body, which is occupied by a solid phase, which is referred to as the solid matrix and the rest of the body, which is called the void space and is mostly occupied by a combination
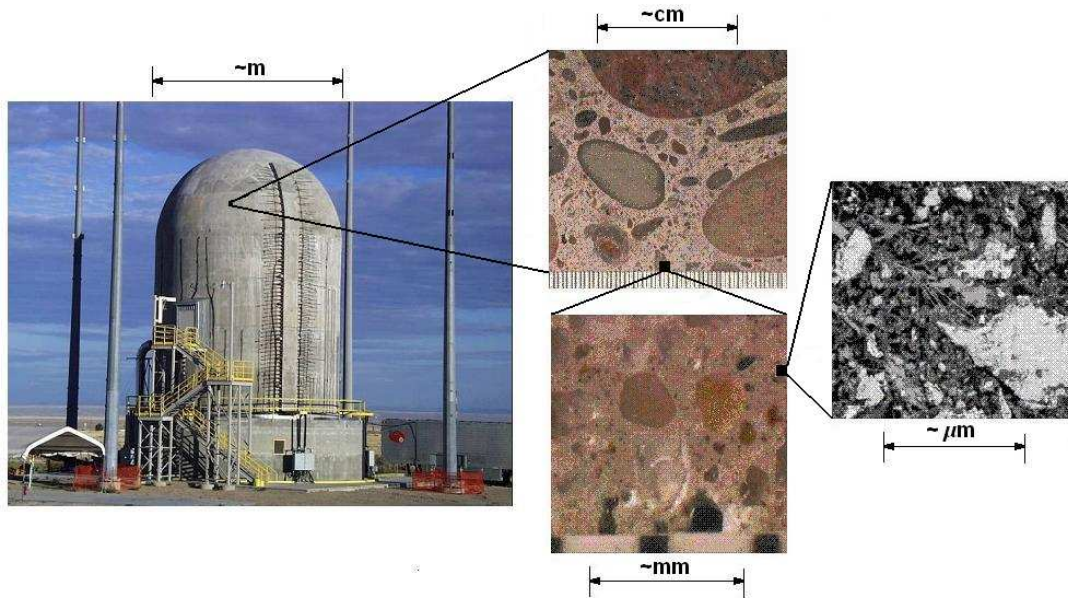
Figure 2.9.: Different scales of concrete and its micro-structure

of fluid phases, such as gas or water.

The heterogeneous nature of concrete determines much of its overall bulk behaviour. On the macroscopic scale (macro-scale) concrete can be considered as a homogeneous material. At a lower level of observation, the so-called meso-scale, distinct phases of aggregates, matrix and single cracks can be distinguished. At the micro- and nano-scale, the structure is also heterogeneous, as can be seen in Figure 2.9.

Another distinct characteristic of porous media is that the solid matrix is distributed through the domain. This implies that wherever a sufficiently large sample is taken within the domain, it will always contain both a solid phase and a void space. Therefore, it is considered valid that a porous medium at the macroscopic scale can be described using a small part of the specimen, which in turn is large enough to contain all the considered phases. This provides a general concept of a Representative Volume Element (RVE), whose size, on one hand, has to be small enough to be considered as infinitesimal and on the other hand it must be large enough to give average quantities without fluctuations [46]. In this work, the phases identified are shown inside the RVE in Figure 2.10. The solid concrete matrix is accompanied by the adsorbed water, which is located on the boundary between the solid matrix and liquid phase. The adsorbed water can be seen as a
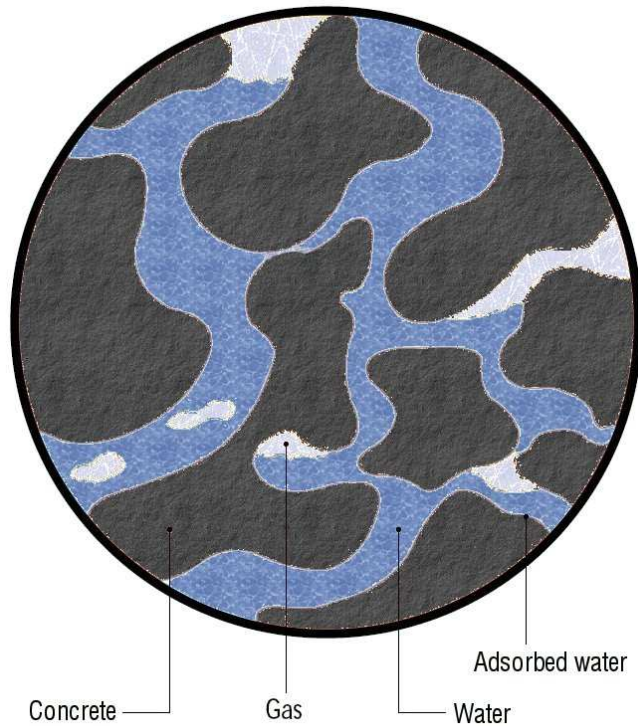
Figure 2.10.: Representative volume element.

part of the solid phase, until the dehydration process starts. Within the specimen pore space, two phases can be distinguished, the liquid phase and the gas phase. The gas phase consists of dry air and a water vapour. As mentioned before, the adequate RVE needs to include all of the mentioned phases.

Based on Bear and Bachmat [9] it can be pointed out that the following tasks need to be carried out to achieve a well-posed formulation of the problem of transport in any porous medium:

1. Formulation of the conceptual physical model, which is followed by the proper mathematical description of all the phenomena in the considered porous domain.

2. Expression of the fluxes of any extensive quantity of any phase in terms of the macroscopic state variables and transport coefficients.

3. Formulation of the set of equations that is required to solve any given transport problem in a specified porous medium domain, using the constitutive relations and necessary state functions.

4. Formulation of the initial and boundary conditions of the given transport problem, that are necessary and sufficient to guarantee a unique solution of the equations arising from 3.

Although the list of tasks presented above seems straightforward, it is not easy to express an appropriate transport formulation using discrete modelling at the microscopic level, due to the lack of information on the interphase boundaries. Moreover, it is convenient to adopt the hypothesis that the material is continuous throughout the domain that it occupies. This allows description of such model through the set of variables which are continuous and differentiable functions of the spatial coordinates and of time. This kind of approach fits the framework of Continuum Mechanics and Thermodynamics. Moreover, it can be used to formulate a proper continuum model and also it can be extended to a multiphase system such as a porous medium. Within such a system, the various phases, which are separated by abrupt interfaces, are assumed to behave as separate, but overlapping continua that fill up the entire domain and interacting with each other. Such an approach needs some general assumptions (similar to Khoury et al. [40]), which are presented below.

First of all, the idealisation of concrete as a porous medium can only be made at the macro-level, where an RVE can be established. At the current stage of this work, this will be the primary and the only level of investigation, with a possible introduction to multi-scale approach discussed in Chapter 8. All global conservative laws apply to the multiphase mixtures as a whole, according to a mixture process. This corresponds to the idea that all transport phenomena of all constituents inside the RVE need to be smeared according to mixture theories and integrated using the concept of volume fractions. This leads to macroscopic variables, which are used in Governing Equations and correspond to experimental quantities. A detailed description of such a theory is presented in [9, 46], where the main idea is that the substitute continua (like liquid, gas and solid) fill the entire domain simultaneously, instead of the real fluids and the solid, which fill only part of the domain. This introduces the reduced density for each continuum, which is obtained through the volume fraction. Volume fractions are defined as the ratio between the volume of material to be distributed and the volume of the considered domain, such that:

$$\sum_{i=1}^{k} \varepsilon_i = 1 \tag{2.3}$$

where ε_i is a volume fraction of phase component i and k is maximum number of all components within the RVE.

Furthermore, an average quantity has to be independent of the size of the RVE and to be continuous in space and time.

The physical model and related conservation and thermodynamics equations can be written for the fully three-dimensional system, based on the assumed level of investigation and space averaging theories. However, at this stage only two-dimensional problems are considered, since 3-D structures require significant computational power. It is worth mentioning, that although the problems presented in the thesis are restricted to 2-D, the formulation has been generalised for 3-D.

Additionally, with regards to the system of equations, all the solid and fluid components from the governing equations at the given time need to be in thermodynamic equilibrium, which means that the state variables associated with the system do not change at a given time. This is analogous with the mechanics of the structure, but in thermodynamic case the system in equilibrium can move to another equilibrium state under the change of thermodynamic forces and conditions.

The material properties are assumed to be temperature and/or pressure dependent. For the applications mentioned in the introductory chapter the range of interest is from the room temperature up to the extreme fire conditions, which leads to a range from 20°C to 1200°C.

As the temperature is rising, the properties of the gas and liquid phases approach one another. At one point a critical temperature is approached, when only one phase can be distinct, a homogeneous super-critical fluid. This critical point for water is established at 374°C. Therefore, the modelling of water as a liquid is up to the critical point and above this temperature water is treated as vapour only. A typical diagram of the phase changes for liquid, solid and gas can be seen in Figure 2.11.

The next step in modelling of transport processes is the distinction between the phases involved. There are three main phases in the model: solid, liquid and gas. The solid phase is that of the solid skeleton of the concrete
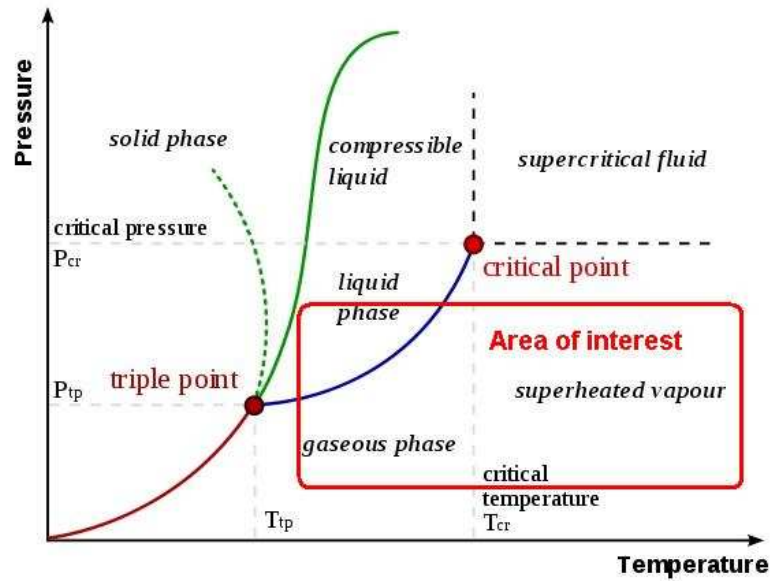
Figure 2.11.: Phase change diagram from [70]

matrix, which is considered a dry phase, but contains the chemically bound water. The remaining phases consist of additional sub-phases. The liquid phase is composed of free water and physically bound water. The free water is located within the capillary pores and is present for levels of saturation up to 100%, where physically bound or adsorbed water is present in the gel pores for levels of saturation up to solid saturation point.

Within the gas phase, there are three phases which consist of dry air, water vapour and a mixture of those two, called moist air.

With respect to transport mechanisms within the model, transport of heat, liquid and gas are involved. Heat can be conducted and advected through the porous media. On the surface, heat can be convected and radiated. The temperature gradient induces the heat flow down the gradient. As a result the moisture gradient and pore pressure gradient start to build up and contribute to the diffusion and Darcy flow, which lead to hydration or dehydration processes and to loss of moisture and mass. Overall, these processes are causing changes in the pore structure, which influences the transport parameters. Therefore, a model which couples these thermo, hygro and mechanical components is needed.

During the heating process all the phase changes are strongly influenced by temperature and for simplicity in the mathematical modelling reversibi-

lity is assumed. This is incorporated into the model along the mass conservation equations, where the conservation of solid, liquid and gas phases is introduced for all the discussed constituents.

2.2.2. Introduction to the mathematical model

To formulate a mathematical model for concrete at high temperatures, all the presented material characteristics and physical concepts, its behaviour and failure modes are necessary. The required components of the mathematical model of the Enhanced Glasgow Model are summarised below and explained in more detail in Chapters 3 and 6.

Standard mathematical models consist of several important formulations. First of all, a definition of domain of influence and its boundaries is required. Then, the state variables, which can describe all the phases need to be selected. At the same time, the differential equations, based on the state variables and describing the ideas from the physical model, are required. Subsequently, the formulation of the relevant constitutive and state equations, for all relevant quantities is needed. If appropriate, the formulation of external sources and sink functions, in terms of state variables is introduced. Finally, to obtain well-posed problem, it is important to formulate initial and boundary conditions needed for the system closure.

In case of concrete at high temperatures, the general laws of conservation must be obeyed. These are the mass conservation equations for the liquid phases and the energy conservation, which represents the laws of the first principle of thermodynamics. Heat transport, including conduction, advection, heat capacity and phase changes, is considered in a single energy conservation equation within the concrete domain. All the constitutive relationships of the concrete, which are mainly derived directly from experimental data, need to describe the real behaviour of the material. At last, all the state equations need to be thermodynamically consistent and allow the dry air and moisture to be treated as ideal gases. Additionally, the transport of these gases is divided into a pressure driven flow, according to Darcy's law and concentration driven flow, due to Fick's law. The transport of absorbed water is taken into account in the definition of the relative permeability of liquid. Different types of boundary conditions will be consi-

dered, fixed, sealed conditions, time-dependent temperatures and fluxes of liquid and gas, or a combination of the above. A detailed description of the thermo-hygro phenomena is presented in Chapter 3.

Furthermore the solid is deformable, resulting in coupling of the fluid, the solid and the thermal fields. Therefore, the full description of the behaviour of concrete at high temperatures can be obtained, when the mechanical response of the structure is included. The mechanical behaviour of porous media can be described using the effective stress principle. The effective stress is defined as the stress which controls the mechanical response, volume change and strength behaviour in a porous medium, independent of the magnitude of the pore pressure. Therefore, the coupling of thermo-hygral model with mechanical model is based on the definition of Bishop's effective stress formulation [10] with the addition of pore pressure effects.

For the mechanical response the additive decomposition of the total strain rate with elastic strain rate, free thermal strain rate, creep strain rate and thermo-mechanical strain rate is assumed. Each of the rates correspond to a different phenomenon. The free thermal strain rate is associated with free thermal expansion as previously explained in section 2.1.3 and it depends on the content of the concrete mix and its moisture state. The creep strain rate and thermo-mechanical strain rate can be combined to form the load induced thermal strain. Together they are based on the concrete response to load induced stress state.

Additionally, the damage effects, which are both thermally and mechanically induced, need to be considered. Due to the fact that the entire model is within the continuum mechanics framework, the damage concept is based on continuum damage mechanics. Such a formulation represents a rational framework for dealing with the evolution of mechanical properties during progressive failure and rupture of a material. Within this framework, the thermo-mechanical damage is seen as temperature-dependent scalar quantity, with the microstructure of the material usually transformed under the influence of thermal gradients, which may lead to progressive damage. The mechanical damage is usually classified as brittle or ductile damage, due to the dislocation, slip planes or microcracks.

In this thesis, the thermo-mechanical damage model is under the assumption that the material remains isotropic and that damage affects Young's
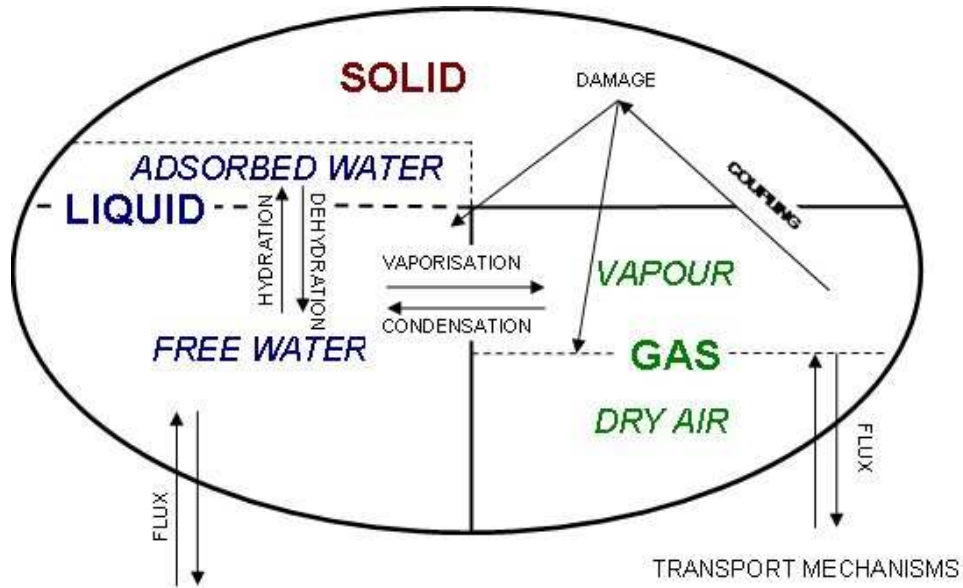
Figure 2.12.: Flow-chart of the model

modulus and bulk modulus equally. Poisson's ratio is not affected by damage. The description of the damaged material is based on two internal variables: a mechanically induced damage component ω and a thermally induced damage component χ. Those two components are used due to the fact that there are different processes through which damage occurs. Mechanical damage is associated with the load/stress induced damage. Thermal damage represents damage that occurs during heating of material. A detailed description of the thermo-mechanical phenomenas and its coupling with the transport model is presented in Chapter 6.

A short overview of the mentioned processes included in the 'Enhanced Glasgow model' is presented in the flow chart form in Figure 2.12. The flow chart is limited to the important aspects of the model and the detailed description of these processes is provided in the following chapters.

2.3. Summary

To summarise, concrete is a complex composite material, which properties are driven by cement paste, aggregate properties and moisture content. Its behaviour can be described within porous media framework. When subjected to thermal conditions, all its physical, thermal and mechanical proper-

ties are strongly influenced by temperature. Consequently, the Enhanced Glasgow model incorporates all the presented properties, its interactions and thermal dependencies.

Additionally, concrete, when subjected to fire conditions, is in danger of explosive spalling. Therefore, a heat and moisture transport description is complemented with mechanical behaviour including damage effects.

The formulation is presented gradually and at first, it is restricted to the thermo-hygral part of the formulation and it does not include any reference to the mechanical part. A full description of this formulation is presented in Chapter 3. Addition of the mechanical behaviour is introduced at a later stage, in the first part of Chapter 6. Up to that point only the transport model of Enhanced Glasgow Model is considered, discussed and validated.

3. Modelling of transport phenomena in concrete at high temperature

The construction of the transport model for concrete, as discussed previously in section 2.2, is very complex. The model needs to handle all of the important phenomena, most of which are nonlinear, including their coupled interactions. A continuum approach for the bulk material behaviour is adopted. The main advantages of such an approach are:

- no need to specify the exact configuration of the inter-phase boundaries,

- the model describes the process in terms of differentiable quantities,

- macroscopic quantities describe the material response and can be verified experimentally.

Clearly, there are some disadvantages resulting from the loss of detailed information about inter-phase boundaries and actual variations of quantities within the domain. Furthermore, the continuum approach requires additional coefficients, relating the statistical/experimental properties with average quantities.

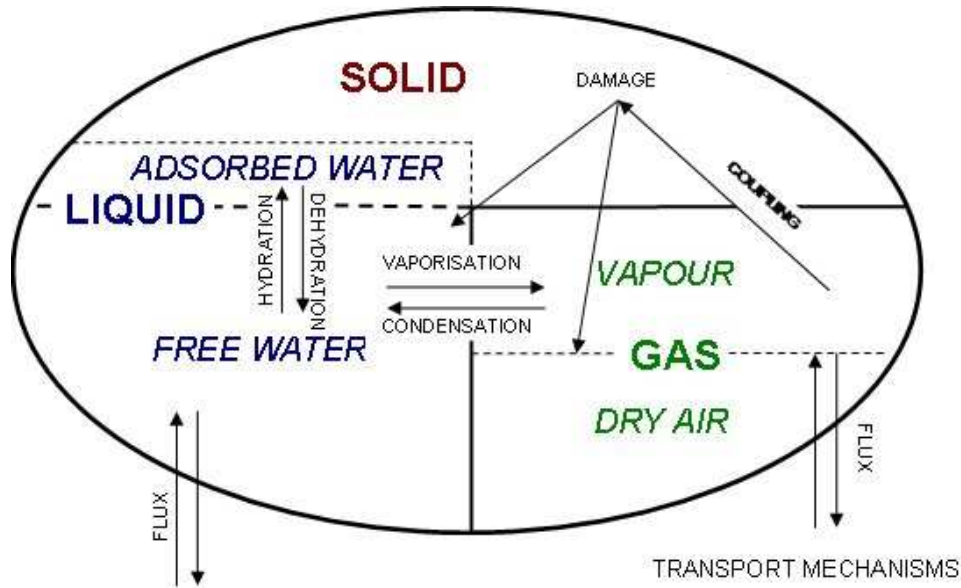This Chapter describes transport phenomena in concrete at high temperatures.

Figure 3.1.: Flow-chart of the model

3.1. Mathematical formulation

The complex problem of heat and moisture transport in porous materials is a coupled phenomenon. In addition to conductive heat transfer moisture migration contributes to convective heat transfer. Mass transport itself is created by the pore pressure gradient developed through the process of water evaporation and heat movement. Most of the material properties of the different phases (solid, liquid and gas) are temperature dependent which leads to transient problems with strong nonlinearities.

3.1.1. Conservation equations

The transport problem is governed by the heat and mass conservation equations. The overview of the model, which was already presented in Figure 2.12, is repeated here in Figure 3.1, where in addition to the solid phase (S), the liquid (L) and gas (G) phases are distinguished. The liquid phase comprises free water (FW) and adsorbed water (D) and the gas phase comprises water vapour (V) and 'dry' air (A). The adsorbed water is a part of the concrete solid matrix, which is released during the dehydration process. These distinct phases are presented within the RVE in Figure 3.2, which is repeated here from Chapter 2.
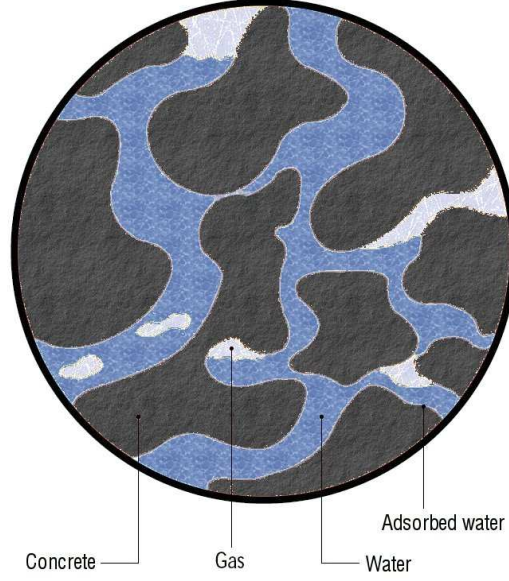
Figure 3.2.: Representative volume element.

Following [15], the mass conservation equation for free water (3.2) and water vapour (3.1) and dry air (3.3) are given as:

$$\frac{\partial \left(\varepsilon_{FW}\rho_L\right)}{\partial t} = -\nabla \mathbf{J}_{FW} - \dot{E}_{FW} + \frac{\partial \left(\varepsilon_{D}\rho_L\right)}{\partial t} \tag{3.1}$$

$$\frac{\partial \left(\varepsilon_{G}\widetilde{\rho}_V\right)}{\partial t} = -\nabla \mathbf{J}_V + \dot{E}_{FW} \tag{3.2}$$

$$\frac{\partial \left(\varepsilon_{G}\widetilde{\rho}_A\right)}{\partial t} = -\nabla \mathbf{J}_A \tag{3.3}$$

where ε_i is the volume fraction of a phase i, ρ_i is the density of a phase i per unit volume of the whole material, $\widetilde{\rho}_i$ is the mass of a phase i per unit volume of gaseous material, $\mathbf{J}_i$ is the mass flux of a phase i, $\dot{E}_{FW}$ is rate of free water evaporation, t is time and $i = L, FW, V, A, D$ are respectively liquid, free water, water vapour, dry air and adsorbed water phase. It can be noted that the term describing the change in dehydrated water content is present within the Free water equation (3.1) since chemically bound water is assumed to be initially released as liquid water.

Furthermore, it is worth noting that the evaporation term is present in both the liquid (3.1) and gas (3.2) conservation equations but with different

signs.

The energy conservation equation is given in Equation (3.4).

$$\left(\underline{\rho C}\right)\frac{\partial T}{\partial t} = -\nabla \cdot \left(-k\nabla T\right) - \left(\underline{\rho C}\mathbf{v}\right) \cdot \nabla T - \lambda_E \dot{E}_{FW} - \lambda_D \frac{\partial \left(\varepsilon_D \rho_L\right)}{\partial t} \quad (3.4)$$

where, $\underline{\rho C}$ is the heat capacity of concrete, k is the thermal conductivity of concrete, $\underline{\rho C}\mathbf{v}$ is the energy transferred by fluid flow, λ_E is the latent heat of evaporation, λ_D is the latent heat of dehydration and T is the absolute temperature.

In order to eliminate the evaporation term in (3.1) and (3.2), these equations are combined to get a system of three governing equations of Dry Air (3.3), Moisture (3.6), and Energy conservation (3.7).

$$\frac{\partial \left(\varepsilon_G \widetilde{\rho}_A\right)}{\partial t} = -\nabla \cdot \mathbf{J}_A \quad (3.5)$$

$$\frac{\partial \left(\varepsilon_G \widetilde{\rho}_A\right)}{\partial t} + \frac{\partial \left(\varepsilon_{FW} \rho_L\right)}{\partial t} - \frac{\partial \left(\varepsilon_D \rho_L\right)}{\partial t} = -\nabla \cdot \left(\mathbf{J}_{FW} + \mathbf{J}_V\right) \quad (3.6)$$

$$\begin{aligned}\left(\underline{\rho C}\right)\frac{\partial T}{\partial t} - \lambda_E \frac{\partial \left(\varepsilon_{FW} \rho_L\right)}{\partial t} + \left(\lambda_D + \lambda_E\right) \frac{\partial \left(\varepsilon_D \rho_L\right)}{\partial t} &= \\ \nabla \cdot \left(k\nabla T\right) + \lambda_E \nabla \cdot \mathbf{J}_{FW} - \left(\underline{\rho C}\mathbf{v}\right) \cdot \nabla T \quad (3.7)\end{aligned}$$

This formulation is consistent with that derived in Tenchev et al. [65], and is employed for the model discussed in this thesis. A complete and well posed formulation requires, in addition to boundary and initial conditions, constitutive relations and thermodynamic properties of the phases involved, which will be presented in following sections.

3.1.2. Constitutive equations

The governing equations comprise appropriate formulations of the relevant constitutive equations. The mass fluxes of dry air (3.8), water vapour (3.9) and liquid (3.10) can be expressed in terms of pressure driven flow and concentration driven flow, under the assumptions that Darcy's and Fick's laws are applicable and that the diffusion of absorbed water on the surface

of the solid cement paste skeleton is negligible [7, 11].

$$\mathbf{J}_A = \varepsilon_G \widetilde{\rho}_A \mathbf{v}_G - \varepsilon_G \widetilde{\rho}_G D_{AV} \triangledown \left(\frac{\widetilde{\rho}_A}{\widetilde{\rho}_G} \right) \tag{3.8}$$

$$\mathbf{J}_V = \varepsilon_G \widetilde{\rho}_V \mathbf{v}_G - \varepsilon_G \widetilde{\rho}_G D_{VA} \triangledown \left(\frac{\widetilde{\rho}_V}{\widetilde{\rho}_G} \right) \tag{3.9}$$

$$\mathbf{J}_{FW} = \varepsilon_{FW} \rho_L \mathbf{v}_L \tag{3.10}$$

where D_{AV} and D_{VA} are the diffusion coefficients (Dry air in water vapour and water vapour in dry air, respectively). Based on Cengel [11] they are assumed to be the same for the purpose of this thesis. The velocities of the gas (3.11) and liquid (3.12) phases results from pressure driven flow, as given by Darcy's law.

$$\mathbf{v}_G = -\frac{K k_G}{\mu_G} \triangledown P_G \tag{3.11}$$

$$\mathbf{v}_L = -\frac{K k_L}{\mu_L} \triangledown P_L \tag{3.12}$$

where K is the intrinsic permeability of the dry concrete, k_i is the relative permeability of the i-th phase, μ_i is its dynamic viscosity and P_i is the corresponding pressure, where $i = (L)$iquid, (G)as.

The dry air and water vapour are assumed to behave as ideal gases, so based on the ideal gas law, their pressures are presented in equations (3.13) and (3.14). There is an associated law of partial pressures, called the Dalton's law. It states that the total pressure exerted by a gaseous mixture is equal to the sum of the partial pressures of each individual component in a gas mixture (3.15), so they are considered to be additive.

$$P_A = R_A \widetilde{\rho}_A T \tag{3.13}$$

$$P_V = R_V \widetilde{\rho}_V T \tag{3.14}$$

$$P_{total} = \sum_{i=1}^{n} p_i \Rightarrow P_G = P_A + P_V \Rightarrow \widetilde{\rho}_G = \widetilde{\rho}_A + \widetilde{\rho}_V \tag{3.15}$$

Finally, in addition to the volume fractions for both liquid and gas (3.16), there is a need for an additional equation, to complete the model, for the free water content as a function of the relative humidity and temperature (3.17).

$$\sum_{j=1}^{k} \varepsilon_i = \phi \qquad (3.16)$$

where $i = FW, A, V$, and ϕ is a porosity.

$$\varepsilon_{FW} = \varepsilon_{FW}\left(RH, T\right) \qquad (3.17)$$

This crucial constitutive equation required to complete the model for elevated temperature will be referred to as sorption isotherm and will be discussed in more detail in section 3.4.

In conclusion, there are 15 unknown variables:

$$T, \ P_V, \ P_A, \ P_G, \ \widetilde{\rho}_V, \ \widetilde{\rho}_A, \ \widetilde{\rho}_G, \ \varepsilon_{FW}, \ \varepsilon_G, \ \dot{E}_{FW}, \ \mathbf{J}_{FW}, \ \mathbf{J}_V, \ \mathbf{J}_A, \ \mathbf{v}_G, \ \mathbf{v}_L$$

and 15 equations. The rate of evaporation, $\dot{E}_{FW}$, is eliminated by substitution of equations (3.1) into (3.2), which results in a reduction of the system of governing equations to three and the reduction of whole system into 14 equations and 14 unknown variables. The summary of the unknown variables and the corresponding equations is presented in Table 3.1.

3.2. Numerical formulation

The system of equation can be written in a number of equivalent ways depending on the choice of primary variables, which to some extent is a matter of convenience. Here, the chosen set of the primary unknown variables consists of the temperature (T), the gas pressure (P_G) and the vapour content ($\tilde{\rho}_V$). This is consistent with both formulations presented in Davie et al. [15] and Tenchev et al. [65]. Different sets of variables ((T, P_A, P_V), ($T, \tilde{\rho}_A, \tilde{\rho}_V$)) were reported to be checked in [65] with conclusions that the results are almost identical. After establishing the set of primary variables it is possible to obtain the simplest notation of the system (3.18) by solving the above differential equations in terms of primary

Summary		
Equation no	unknowns	Physical meaning
3.3	$\varepsilon_G, \widetilde{\rho}_A, \mathbf{J}_A$	Air Mass Conservation
3.6	$\varepsilon_{FW}, \varepsilon_G, \mathbf{J}_{FW}, \mathbf{J}_V, \widetilde{\rho}_A$	Moisture Mass Conservation
3.7	$\varepsilon_{FW}, \mathbf{J}_{FW}, T$	Energy Conservation
3.8	$\mathbf{J}_A, \mathbf{v}_G, \widetilde{\rho}_A, \widetilde{\rho}_G$	Dry Air Flux
3.9	$\mathbf{J}_V, \mathbf{v}_G, \widetilde{\rho}_V, \widetilde{\rho}_G$	Vapour Flux
3.10	$\mathbf{J}_{FW}, \mathbf{v}_L, \varepsilon_{FW}$	Liquid Flux
3.11	$\mathbf{v}_G, P_G$	Gas Velocity
3.12	$\mathbf{v}_L, P_L$	Liquid Velocity
3.13	$\widetilde{\rho}_A, T$	Air pressure
3.14	$\widetilde{\rho}_V, T$	Gas Pressure
3.15	P_V, P_A, P_G	Dalton's law of partial pressures
3.15	$\widetilde{\rho}_V, \widetilde{\rho}_A, \widetilde{\rho}_G$	Modified Dalton's law
3.16	$\varepsilon_{FW}, \varepsilon_G$	Volume Fractions
3.17	ε_{FW}, T	Sorption Isotherm
14 equations	14 unique unknowns	

Table 3.1.: Summary of transport formulation

variables $\mathbf{u} = \left(\begin{array}{ccc} T & P_G & \tilde{\rho}_V \end{array} \right)^T$, and this is presented in Appendix B. The three governing equations (3.3, 3.6, 3.7) can be expressed in a simplified form as:

$$\mathbf{C\dot{u}} - \bigtriangledown \cdot (\mathbf{K} \bigtriangledown \mathbf{u}) = 0 \qquad (3.18)$$

Where the matrices $\mathbf{C}$ and $\mathbf{K}$ are presented in Equation (3.19).

$$\mathbf{C} = \left(\begin{array}{ccc} C_{TT} & C_{TP} & C_{TV} \\ C_{AT} & C_{AP} & C_{AV} \\ C_{MT} & C_{MP} & C_{MV} \end{array} \right), \ \mathbf{K} = \left(\begin{array}{ccc} K_{TT} & K_{TP} & K_{TV} \\ K_{AT} & K_{AP} & K_{AV} \\ K_{MT} & K_{MP} & K_{MV} \end{array} \right) \qquad (3.19)$$

The components of these matrices are presented in Appendix A.

A Finite Element formulation for the solution to these governing equations can be achieved by using the standard Galerkin Weighted Residual formulation (eg. Zienkiewicz & Taylor [74]). First equation (3.18) is multiplied by a set of test functions $\boldsymbol{V}$ for the primary variables and integrated over the domain, to give:

3. Modelling of transport phenomena in concrete at high temperature

$$\int_{\Omega} \mathbf{V} \cdot (\mathbf{C\dot{u}} - \triangledown (\mathbf{K} \triangledown \mathbf{u})) dV = 0 \tag{3.20}$$

where

$$\mathbf{V} = \begin{pmatrix} \nu_T & 0 & 0 \\ 0 & \nu_A & 0 \\ 0 & 0 & \nu_M \end{pmatrix} \tag{3.21}$$

The weak form of the governing equations is obtained by application of Green's theorem to Equation (3.20). Considering only two-dimensional vector fields, Green's theorem is equivalent to the following two-dimensional analogue of the divergence theorem:

$$\int_{\Omega} (\triangledown \varphi) \, d\Omega = \oint_{\partial \Omega} (\varphi \boldsymbol{n}) \, dS \tag{3.22}$$

where $\boldsymbol{n}$ is the boundary normal.

Letting $\varphi = \boldsymbol{V} \cdot (\mathbf{K} \triangledown \mathbf{u})$, application of Green's theorem to the problem at hand, yields

$$\int_{\Omega} \mathbf{V} \cdot \mathbf{C\dot{u}} dV + \int_{\Omega} \triangledown \mathbf{V} \cdot (\mathbf{K} \triangledown \mathbf{u}) \, dV - \int_{\partial \Omega} \mathbf{V} \cdot \mathbf{K} \mathbf{q_n} dS = 0 \tag{3.23}$$

where

$$\triangledown \mathbf{V} = \begin{pmatrix} \triangledown \nu_T & 0 & 0 \\ 0 & \triangledown \nu_A & 0 \\ 0 & 0 & \triangledown \nu_M \end{pmatrix} \tag{3.24}$$

and

$$\mathbf{q_n} = \begin{pmatrix} \frac{d}{dn}T & \frac{d}{dn}P_G & \frac{d}{dn}\tilde{\rho}_V \end{pmatrix}^T \tag{3.25}$$

Switching to matrix-vector notation, the primary variables $\mathbf{u}$ and the test functions $\mathbf{V}$ are discretised as:

3.   Modelling of transport phenomena in concrete at high temperature

$$\begin{aligned}
\mathbf{u} &= \mathbf{Na} \\
\mathbf{V} &= \mathbf{Nb}
\end{aligned} \tag{3.26}$$

where $\mathbf{N}$ are the shape functions for the primary variables. Equation (3.26) can be further expanded as

$$\mathbf{u} = \begin{pmatrix} T \\ P_G \\ \rho_v \end{pmatrix} = \begin{pmatrix} h_T & 0 & 0 \\ 0 & h_P & 0 \\ 0 & 0 & h_{\rho_V} \end{pmatrix} \begin{pmatrix} a_T \\ a_A \\ a_M \end{pmatrix} = \mathbf{Na} \tag{3.27}$$

Inserting Equation (3.27) into Equation (3.23) and requiring that the result holds for all admissible $\mathbf{b}$ gives:

$$\int_\Omega \mathbf{N^T C N \dot{a}} d\Omega + \int_\Omega \bigtriangledown\mathbf{N^T} \left(\mathbf{K} \bigtriangledown \mathbf{Na} \right) d\Omega - \int_{\partial\Omega} \mathbf{N^T} \left(\mathbf{K q_n} \right) dS = 0 \tag{3.28}$$

Given the nonlinear nature of the second component of Equation (3.28), where the divergence of primary variable can be seen, a Newton-Raphson solution method is adopted and (3.28) must be linearised. To this end, the discretised primary variables are expressed as:

$$\mathbf{a}^k = \mathbf{a}^{k-1} + \mathbf{da} \tag{3.29}$$

with k and k-1 indicating the Newton iteration numbers. Substituting these decompositions into the discrete set of equations(3.28) yields:

$$\int_\Omega \mathbf{N^T C N \dot{a}} d\Omega + \int_\Omega \bigtriangledown\mathbf{N^T} \left(\mathbf{K} \bigtriangledown \mathbf{N} \left(\mathbf{a}^{k-1} + \mathbf{da} \right) \right) d\Omega - \int_{\partial\Omega} \mathbf{N^T} \left(\mathbf{K q_n} \right) dS = 0 \tag{3.30}$$

To carry out the time integration of Equation (3.30), a central difference scheme is adopted. For a given time interval $\triangle t = t_i - t_{i-1}$ the primary variables at time t are defined via linear interpolation as

$$\mathbf{a}(t) = \alpha_d \mathbf{a}_i + (1 - \alpha_d) \, \mathbf{a}_{i-1} \tag{3.31}$$

3. Modelling of transport phenomena in concrete at high temperature

where $\alpha_d = (t - t_{i-1})/\triangle t$, $\mathbf{a}_i$ and $\mathbf{a}_{i-1}$ are the discrete primary variables at the start and end of the times step respectively. Furthermore:

$$\dot{\mathbf{a}} = \frac{1}{\triangle t}\left(\mathbf{a}_i - \mathbf{a}_{i-1}\right) \tag{3.32}$$

Substitution of the decomposition of the arrays (3.29) into (3.31) and (3.32) gives:

$$\mathbf{a}(t) = \alpha_d\mathbf{a}_i^{k-1} + \alpha_d\mathrm{d}\mathbf{a} + (1 - \alpha_d)\mathbf{a}_{i-1} \tag{3.33}$$

and

$$\dot{\mathbf{a}} = \frac{1}{\triangle t}\left(\mathbf{a}_i^{k-1} + \mathrm{d}\mathbf{a} - \mathbf{a}_{i-1}\right) \tag{3.34}$$

Substitution of (3.33) and (3.34) into the weak form of the governing Equation (3.35) yields:

$$\int_\Omega \frac{1}{\triangle t}\mathbf{N}^{\mathrm{T}}\mathbf{C}\mathbf{N}\left(\mathbf{a}_i^{k-1} + \mathrm{d}\mathbf{a} - \mathbf{a}_{i-1}\right)d\Omega \quad +$$

$$\int_\Omega \bigtriangledown\mathbf{N}^{\mathrm{T}}\left(\mathbf{K}\bigtriangledown\mathbf{N}\left(\mathbf{a}^{k-1} + \mathrm{d}\mathbf{a}\right)\right)d\Omega \quad -$$

$$\int_{\partial\Omega}\mathbf{N}^{\mathrm{T}}\left(\mathbf{K}\mathbf{q_n}\right)dS \quad = \quad 0 \tag{3.35}$$

This can alternatively be expressed as:

$$\bar{\mathbf{K}}\mathrm{d}\mathbf{a} = \mathbf{f}^{ext} - \mathbf{f}^{int} \tag{3.36}$$

or

$$\begin{pmatrix} \bar{K}_{TT} & \bar{K}_{TP} & \bar{K}_{TV} \\ \bar{K}_{AT} & \bar{K}_{AP} & \bar{K}_{AV} \\ \bar{K}_{MT} & \bar{K}_{MP} & \bar{K}_{MV} \end{pmatrix} \begin{pmatrix} \mathrm{d}\mathbf{a}_T \\ \mathrm{d}\mathbf{a}_A \\ \mathrm{d}\mathbf{a}_M \end{pmatrix} = \begin{pmatrix} \mathbf{f}_T^{ext} - \mathbf{f}_T^{int} \\ \mathbf{f}_A^{ext} - \mathbf{f}_A^{int} \\ \mathbf{f}_M^{ext} - \mathbf{f}_M^{int} \end{pmatrix} \tag{3.37}$$

where

3. Modelling of transport phenomena in concrete at high temperature

$$\bar{\mathbf{K}} = \begin{pmatrix} \bar{K}_{TT} & \bar{K}_{TP} & \bar{K}_{TV} \\ \bar{K}_{AT} & \bar{K}_{AP} & \bar{K}_{AV} \\ \bar{K}_{MT} & \bar{K}_{MP} & \bar{K}_{MV} \end{pmatrix} =$$
$$= \int_{\Omega} \left(\frac{1}{\triangle t} \mathbf{N}^{\mathrm{T}} \mathbf{C} \mathbf{N} + \alpha_d\left(t\right) \cdot \bigtriangledown^{\mathrm{T}} \mathbf{N} \left(\mathbf{K} \bigtriangledown (\mathbf{N})\right) \right) dV \qquad (3.38)$$

specifically

$$\bar{K}_{TT} = \int_{\Omega} \left(\frac{1}{\triangle t} N_T^{\mathrm{T}} C_{TT} N_T + \alpha_d\left(t\right) \cdot \bigtriangledown N_T^{\mathrm{T}} \left(K_{TT} \bigtriangledown (N_T)\right) \right) dV \qquad (3.39)$$

where the force vectors are for example defined as:

$$\mathbf{f}_T^{ext} = \int_{\partial\Omega} \mathbf{N}_T^{\mathrm{T}} K_{TT} \mathbf{q}_n dS \qquad (3.40)$$

$$\begin{aligned} \mathbf{f}_T^{int} = \ & \triangle t \left(K_{TT} \triangle \mathbf{a}_T^{k-1} + K_{TP} \triangle \mathbf{a}_A^{k-1} + K_{TV} \triangle \mathbf{a}_M^{k-1} \right) \\ & + C_{TT} \triangle \mathbf{a}_T^{k-1} + C_{TP} \triangle \mathbf{a}_A^{k-1} + C_{TV} \triangle \mathbf{a}_M^{k-1} \qquad (3.41) \end{aligned}$$

All other terms follow a similar pattern.

3.3. Boundary and initial conditions

The problem boundary conditions can be described as either prescribed (Dirichlet) or natural (Neumann) boundary conditions. For the thermal problem a generic natural boundary conditions can be described as (3.42):

$$k\frac{\partial T}{\partial n} - \left(H_G - H_G^0\right)\mathbf{J}_G \cdot \mathbf{n} + \left(H_G - H_G^0\right)\beta\left(\tilde{\rho}_G - \tilde{\rho}_{G,\infty}\right) +$$
$$\lambda\mathbf{J}_L \cdot \mathbf{n} + h_{qr}\left(T - T_\infty\right) \quad = 0 \quad (3.42)$$

where, the H_G and H_G^0 are the enthalpy of the gaseous mixture at current and ambient conditions, respectively. β is the coefficient of water vapour mass transfer on the boundary, h_{qr} is the combined convection and radiation heat transfer coefficient, $\tilde{\rho}_{G,\infty}$ and T_∞ are the vapour content and temperature of the surrounding and $\mathbf{n}$ is the vector normal to the boundary.

The first term from the left is the heat energy transferred to the boundary surface from inside the body by conduction. The second term is the energy accumulated in the gaseous mixture, which enters the boundary from inside of the concrete. The third term is the heat energy accumulated in the gaseous mixture, which escapes from the boundary to environment. The fourth one is the heat energy used for evaporation of liquid water. The fifth one is the heat energy dissipated by convection and radiation to the surrounding medium.

In order to simplify the problem, it may be reasonably assumed that the concrete surface exposed to the atmosphere, will dry out and consequently there will be no or negligible amount of liquid flux across the boundary escaping to the atmosphere, i.e. $\mathbf{J}_L = 0$. For further simplicity, the flux of the gaseous material transferred to the boundary from inside the concrete is assumed to be equal to the gaseous material dissipated from the boundary into the surrounding environment. Based on this assumption the mass conservation for the gaseous phase on the boundary can be established as (3.43).

$$\mathbf{J}_G \cdot \mathbf{n} - \beta\left(\tilde{\rho}_G - \tilde{\rho}_{G,\infty}\right) = \mathbf{0} \quad (3.43)$$

Given these assumptions, the energy conservation equation for the boun-

dary (3.42) using (3.43) can be rewritten as (3.44).

$$\frac{\partial T}{\partial n} = -\frac{h_{qr}}{k}(T - T_\infty) \tag{3.44}$$

The gas pressure at the boundary is assumed to be equal to the atmospheric pressure, so based on that the gradient of gas pressure across the boundary will be zero (3.45).

$$\frac{\partial P_G}{\partial n} = 0 \tag{3.45}$$

Taking into account that the flux of the vapour transferred to the boundary from inside the concrete is assumed to be equal to the vapour dissipated from the boundary into the surrounding environment, the mass conservation of water vapour on the boundary may be written as shown in Equation (3.46).

$$\mathbf{J}_V \cdot \mathbf{n} - \beta(\tilde{\rho}_V - \tilde{\rho}_{V,\infty}) = \mathbf{0} \tag{3.46}$$

Following [15, 65] and the derivation from Appendix A, the final equations for boundary conditions are presented in (3.47).

$$
\left\{ \begin{array}{c} \frac{\partial T}{\partial n} \\ \frac{\partial P_G}{\partial n} \\ \frac{\partial \tilde{\rho}_V}{\partial n} \end{array} \right\} = \left[\begin{array}{ccc} K_{TT} & 0 & 0 \\ 0 & 0 & 0 \\ K_{VT} & 0 & K_{VV} \end{array} \right]^{-1} \left\{ \begin{array}{c} h_{qr}T_\infty \\ P_{g,\infty} \\ \beta\tilde{\rho}_{V,\infty} \end{array} \right\} -
$$
$$
\left[\begin{array}{ccc} K_{TT} & 0 & 0 \\ 0 & 0 & 0 \\ K_{VT} & 0 & K_{VV} \end{array} \right]^{-1} \left[\begin{array}{ccc} h_{qr} & 0 & 0 \\ 0 & 0 & 0 \\ 0 & 0 & \beta \end{array} \right] \left\{ \begin{array}{c} T \\ P_g \\ \tilde{\rho}_V \end{array} \right\} \tag{3.47}
$$

where K_{TT}, K_{VT} and K_{VV} are first introduced in section 3.2.

In order to establish initial conditions for the model, the internal values of temperature and gas pressure can be experimentally measured and input into the problem definition. However, vapour mass content $\tilde{\rho}_V$, is not a measured quantity and there is a need to express it with respect to a measured data. Therefore, the ideal gas equation for vapour is repeated in (3.48). It can be substituted into the expression for relative humidity $RH = \frac{P_V}{P_{Sat}}$. The equation (3.49) is the final product of the manipulations

and it represents the initial vapour mass content as a function of relative humidity and temperature, which can be experimentally obtained.

$$P_V = \tilde{\rho}_V R_V T \tag{3.48}$$

$$\tilde{\rho}_V^0 \left(RH, T \right) = \frac{RH \cdot P_{Sat} \left(T \right)}{R_V T} \tag{3.49}$$

The discretised weak form of the governing equations and constitutive equations with initial and boundary conditions defines the problem. However, there is a need for state variables of phases and concentrations of components in the different phases. Therefore, all the complementary equations and variables are presented in the next section 3.4.

3.4. State equations, heat and mass transfer and thermal properties

3.4.1. Sorption isotherms

As mentioned before in section 3.1.2 the crucial constitutive equation required to complete the model for elevated temperature is a function, which relates the free water content with relative humidity and temperature (3.17).

At equilibrium, the relationship between free water content and relative humidity of a material can be displayed graphically by a curve, the so called moisture sorption isotherm. For each relative humidity value, a sorption isotherm indicates the corresponding free water content value at a given, constant temperature. If the composition or temperature of the material changes, then its sorption behaviour also changes. Because of the complexity of sorption processes, the isotherms cannot be determined by calculation, but must be recorded experimentally for each product. Usually, it can be experimentally measured with respect to capillary pressure and a level of saturation. This section will present a logical description of the connection between free water content and relative humidity, using capillary pressure as a function of saturation. A short diagram that presents this formulation missing link is presented in Figure 3.3.

First, following Bear [8] we can consider a water that fully fills the void space of a porous media. The process of gradual drainage from the top of the specimen is illustrated in Figure 3.4, where successive stages of this process are numbered from 1 till 5. At first, at 1 stage the specimen is fully saturated, which means that the pore structure is 100% filled with water. Next, when the fluid is drained from the surface of the sample and air is introduced on top of that there is a water-air interaction and menisci can form at interface 2. The radius of curvature at every point on a meniscus depends on the pressure difference between water pressure and air pressure. This difference can be written using Laplace formula for a capillary pressure:

$$P_C = P_A - P_L = \frac{2}{r^*}\gamma_{wa} \qquad (3.50)$$

where γ_{wa} is surface tension and r^* is mean radius of curvature.
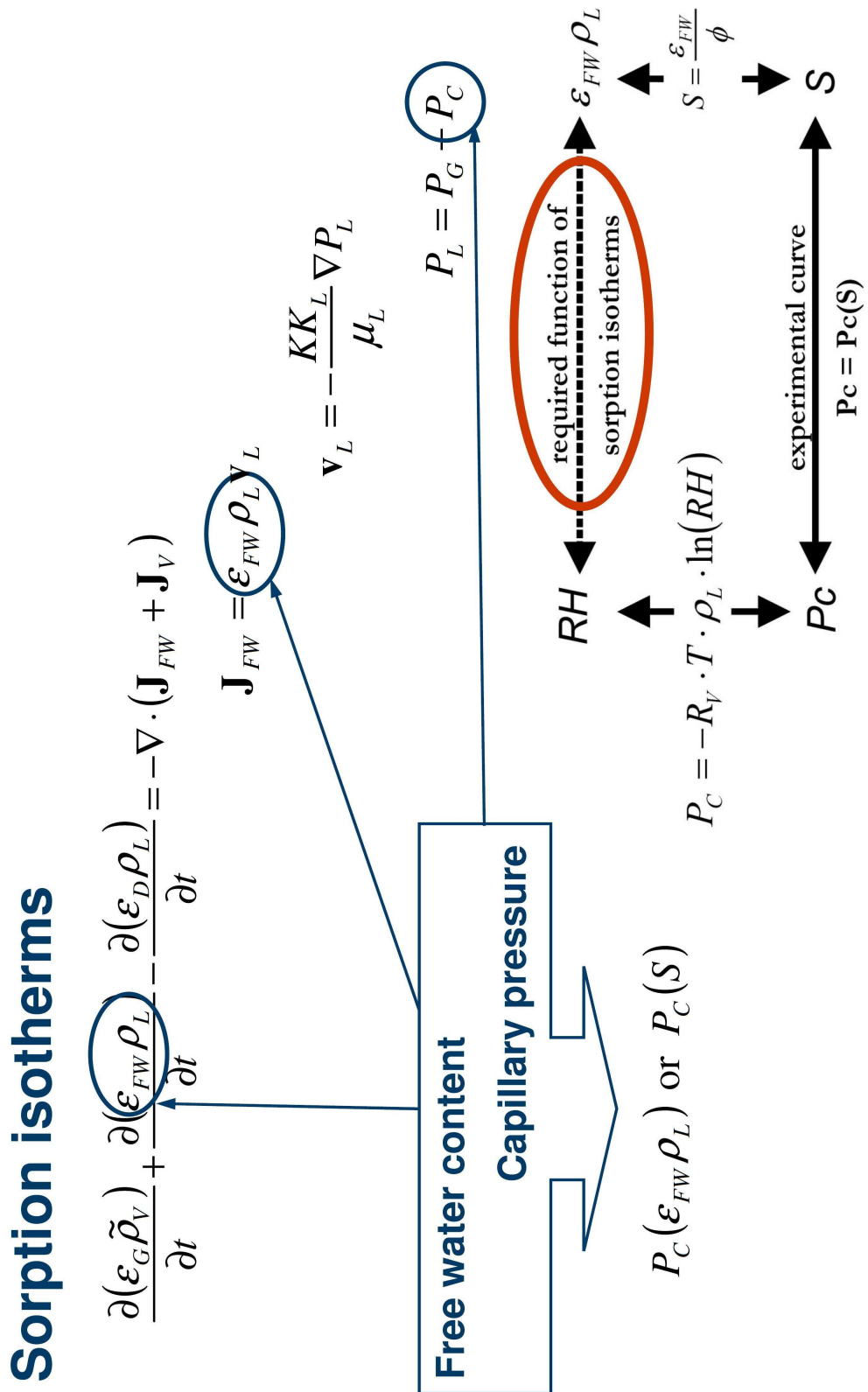
Figure 3.3.: Sorption isotherms diagram

1 - full water level

2 - initial drainage

3 - capillary action

4 - non-equilibrium capilars

5 - equilibrium state
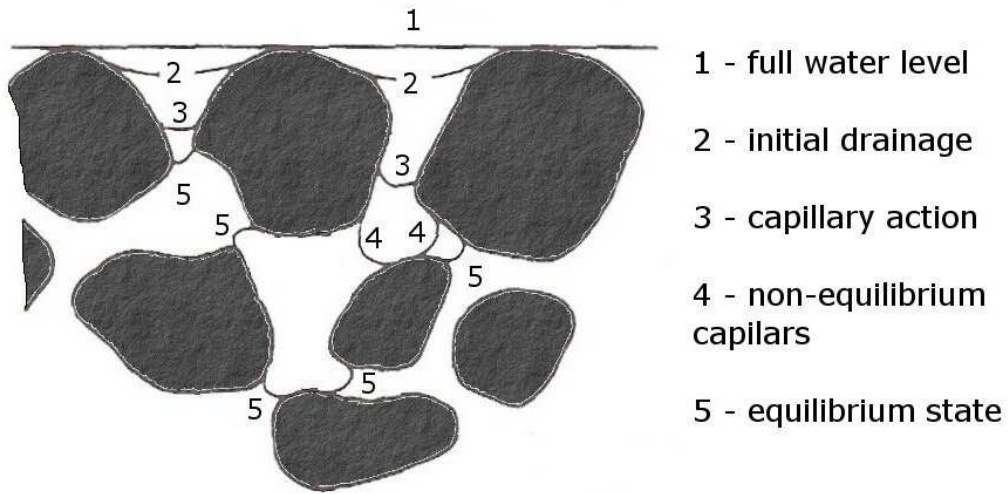
Figure 3.4.: Gradual drainage, reproduced from [8]

The above equation (3.50) indicates that the greatest capillary pressure that can be maintained by the local interface, corresponds to the smallest radius of curvature (stage 3). On the other hand the channels which support a larger radius (stage 4), because of the reduced boundary area, are in a non equilibrium stage and the water needs to continue to retreat until the local equilibrium position is obtained (stage 5), or until almost complete withdrawal of the liquid. The complete withdrawal of the liquid corresponds to the fully unsaturated specimen when the pore structure is completely filled with gas. The relationship, which describes the quantity of fluid present in the void space, is a function of the saturation (S) and is called a sorption/desorption curve. Initially, it will be expressed with respect to capillary pressure, what is presented below:

$$P_C = P_C\left(S\right) \tag{3.51}$$

For a given porous medium, the capillary pressure curve is derived experimentally. Various authors have proposed analytical expressions for describing the general shape of these curves, which needs a proper fitting into the experimental results. In this regard, Bear [9] presented a list of references to some important formulations, like Brooks and Correy (1964), Brutsaert (1966), Van Genuchten (1980) and Vauclin et al. (1979). An important formulation, from the point of view of high temperatures approach, is the one

presented by Bazant [7]. Indeed it gave the basis for the sorption isotherms used in both Tenchev et al. [65] and Davie et al. [15], and is presented in the next subsection. This is described as semi-empirical, although the theoretical extension to the experimental data is difficult to follow and somewhat unclear. It will also be shown that the response of concrete is very sensitive to the sorption isotherms during heating. Therefore, an alternative formulation to the Bazant's sorption isotherms is further investigated. Baroghel-Bouny et al. [3] presented very clear experimental results for the sorption curves for Normal (NSC) and High Strength Concrete (HSC) at room temperatures. These results have been extended by Pesavento [59] to include temperatures effects, although the physical justification for the modified formulation is unclear. Here the approach proposed by Leverett [45] is adopted, in which the variation of the sorption curves for different types of the same material is restricted to the variation in the mean pore size of the porous medium and the surface tension of the fluid. Consequently, it was possible to extend Baroghel-Bouny's [3] formulation at room temperature by recognising the temperature dependence of the porosity, permeability and surface tension. This is further elucidated in subsection 3.4.1.2, after the discussion on Bazant's formulation, which is next.

3.4.1.1. Bazant's formulation

Bazant [7] stated in his book that, *'while the general form of the field equations is clear, there is more uncertainty about the material properties'*. In his isotherm formulation the main idea is to have two different formulae for the unsaturated (3.52) and the saturated (3.53) state, with an intermediate section - transition zone - for the relative humidity between 0.96 and 1.04.

$$w = c \left(\frac{w_1}{c} RH \right)^{\frac{1}{m(T)}}, \text{ for } RH \leq 0.96 \tag{3.52}$$

$$w = (1 + 3\epsilon^v) \frac{\phi}{v}, \text{ for } RH \geq 1.04 \tag{3.53}$$

where RH is relative humidity, c is a mass of cement per m^3 of concrete, w_1 is a saturation water content at 298.15K, v is a specific volume of water as a function of temperature and pressure and ϵ^v is the linear volumetric strain of concrete.

Bazant Sorption Isotherms fot NSC
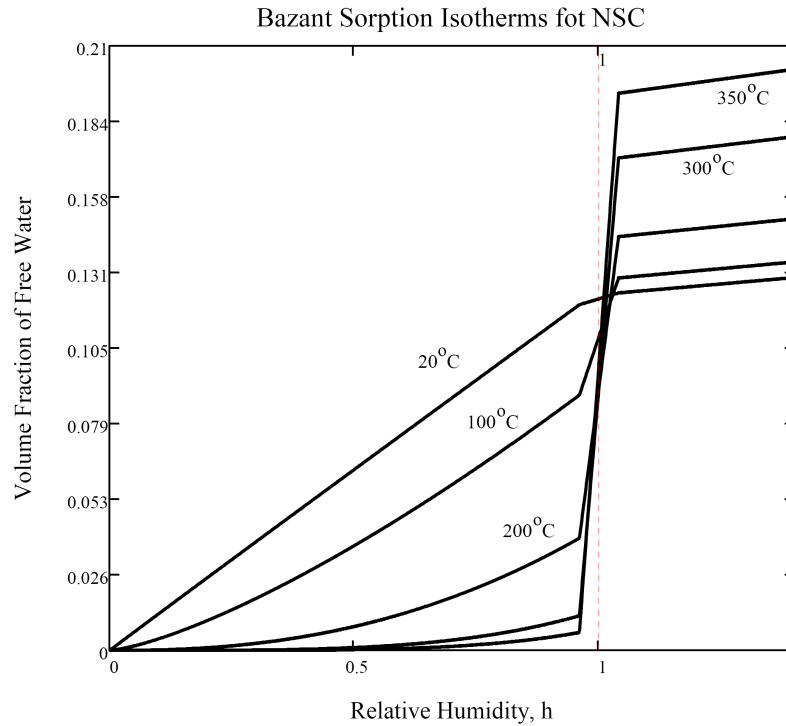
Figure 3.5.: Sorption Isotherms by Bazant [7]

The transition zone, between the saturated and the unsaturated zone, is introduced due to different distribution of pore sizes, where different pore pressure can build up at the same time. This relies on the fact that the transition from unsaturated to saturated state is not an abrupt one, except for the extreme case of homogeneous pore size. The formulation allows relative humidity and saturation to exceed 100%, which from physical point of view is difficult to justify. Furthermore, this approach does not distinguish different water phases but all moisture is considered in the voids of concrete. Up to a certain temperature level the moisture content is considered as liquid, but after a critical point of water, moisture can only be considered as vapour.

Therefore, it is unclear whether this relationship is correct for the proposed type of modelling, especially for a multiphase system in the areas of temperature build-up close to the critical point of water. Furthermore, Bazant's formulation was intended for normal strength concrete, but in fire engineering the focus of attention is frequently on high strength concrete, as discussed in Chapter 1.

52

	Mix	
	NSC	HSC
a(MPa)	18.6237	46.9364
b	2.2748	2.0601
ϕ	0.122	0.082

Table 3.3.: Parameters for Equation (3.54) and corresponding porosity (ϕ) for different concrete mixes based on [3].

3.4.1.2. Leverett based sorption isotherms [45, 57]

Baroghel-Bouny et al. [3] undertook a series of important experiments at room temperature in order to establish a common expression for the sorption curve of both NSC & HSC (3.54). The final form of this expression was given as:

$$P_C\left(S\right) = a\left(S^{-b} - 1\right)^{1-1/b} \tag{3.54}$$

where a and b are coefficients that vary depending upon the concrete mix (see Table 3.3).

The degree of saturation with free water can be described using volume fraction of a liquid water, ε_{FW}, and the porosity, ϕ, as given in Equation (3.55). This relationship can be used to reformulate equation (3.54) into the form of (3.56).

$$S = \frac{\varepsilon_{FW}}{\phi} \tag{3.55}$$

$$P_C\left(\varepsilon_{FW}\right) = a\left(\left(\frac{\varepsilon_{FW}}{\phi}\right)^{-b} - 1\right)^{1-1/b} \tag{3.56}$$

This relationship can be expressed in a more convenient form in terms of relative humidity, using Kelvin's equation:

$$P_C = -ln\left(h\right)\rho_L R_V T \tag{3.57}$$

Substitute of this into (3.56) gives:
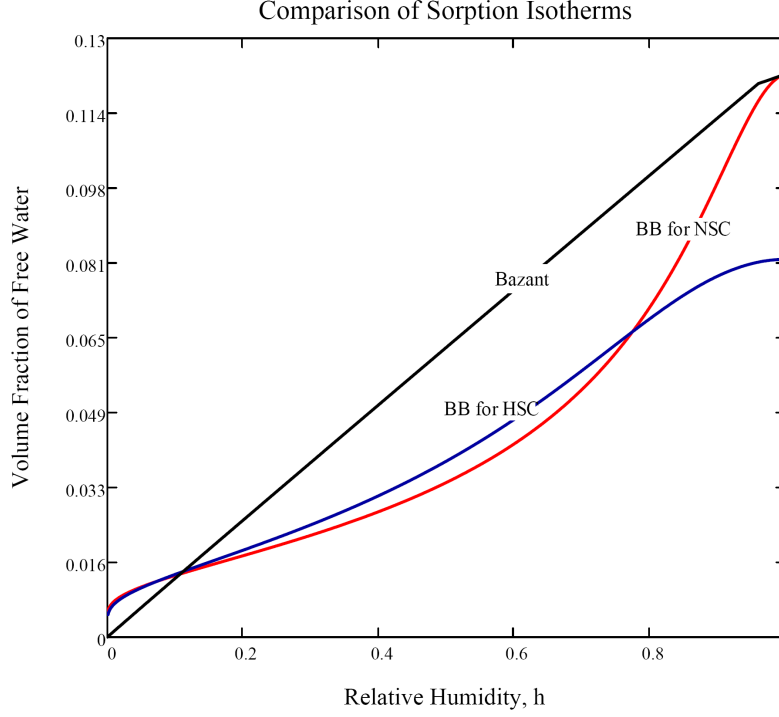
Figure 3.6.: Sorption Isotherms at room temperature for NSC and HSC

$$-ln\left(h\right)\rho_L R_V T = a\left(\left(\frac{\varepsilon_{FW}}{\phi}\right)^{-b} - 1\right)^{1-1/b} \qquad (3.58)$$

or

$$\varepsilon_{FW} = \varepsilon_{FW}\left(h\right) \qquad (3.59)$$

This relationship (3.59) is shown in Figure 3.6 for both concrete mixes described in Chapter 2, with the parameters established by Baroghel-Bouny et al. [3] and presented in Table 3.3. Additionally, the Bazant sorption isotherm at 20℃ is drawn on the same graph. It can be clearly seen that Bazant's formulation is linear for the relative humidity between range 0 to 100%. It is distinctively different to the equivalent Baroghel-Bouny sorption isotherm for NSC. Baroghel-Bouny's formulation is higher at the low relative humidity up to 10% and lower at the rest of the range. The final value at 100% of relative humidity is the same, as both formulations are based on the same amount of porosity.

The main difference between NSC and HSC formulations is the final value at the 100% relative humidity level. However, this is enforced by the level of porosity for these two types of concrete. Although, for the levels of relative humidity up to almost 75% the two graphs look very similar, one of them cannot be used in place of the other.

Temperature dependent capillary pressure curves - sorption isotherms
The formulation for the capillary pressure curve presented by Baroghel-Bouny et al. [3] is applicable only at ambient temperature. For the model to be applicable to elevated temperatures regime, it is necessary to introduce temperature dependency to the Equation (3.59). However, there is very little experimental data, on which it would be possible to build up an extension of this formulation to include high temperature effects. One of the exceptions is the aforementioned work by Bazant [7], where the previous formulation was explained and compared to experimental results. Pesavento [59] presented a temperature dependency, based on Bazant's results and using Baroghel-Bouny et al. [3] formulation (3.54), although some physical aspects of this modified formulation are unclear. Hence, an alternative and potentially more rational approach is presented here.

Leverett [45] adopted a semi-empirical approach, which relates the capillary pressure not only to the degree of saturation but also to the properties of both the fluid and porous media:

3.   Modelling of transport phenomena in concrete at high temperature

$$P_C(S) = \gamma J(S) \sqrt{\frac{\phi}{K}} \qquad (3.60)$$

where the Leverett J-function is expressed as:

$$J(S) = \frac{P_C(S)}{\gamma} \sqrt{\frac{K}{\phi}} \qquad (3.61)$$

Leverett showed for several data for the unconsolidated sands that the dimensionless function reduces to a common curve called the J-function (3.61), which could be interpreted as a scaling factor for the reference capillary pressure curve. This function incorporates the effects of inter-facial tension (γ) and uses a simple expression for the average pore radius ($\sqrt{\frac{K}{\phi}}$).

Leverett [45] described experimental determination of this curvature - saturation relation for unconsolidated sands. In order to extend this approach to concrete, the appropriate J-function can be obtained by incorporating the previously presented Baroghel-Bouny formulation (3.54) into the Leverett J-function and keeping all the parameter at room temperature of 20°C:

$$J_{BB}(S) = \frac{P_C(S)}{\gamma_0} \sqrt{\frac{K_0}{\phi_0}} = \frac{a\left((S)^{-b} - 1\right)^{1-1/b}}{\gamma_0} \sqrt{\frac{K_0}{\phi_0}} \qquad (3.62)$$

where γ_0, K_0 and ϕ_0 are respectively surface tension, permeability and porosity at temperature of 20°C.

Although a unique J-function that is the same for all types of concrete mixtures is not applicable, as the formulation is based on Baroghel-Bouny approach, it is here hypothesised that the J-function (3.62) remains unchanged for elevated temperatures. Indeed it is assumed that throughout the temperature range, the temperature dependency of the capillary pressure curve can be accounted for via the temperature dependency of the properties of the fluid and of the porous medium itself, through the surface tension ($\gamma(T)$), porosity ($\phi(T)$) and permeability ($K(T)$). To sum up, Equation (3.62) can be substituted into (3.60) and rewritten to indicate temperature dependency as follows:

Sorption Isotherms fot NSC
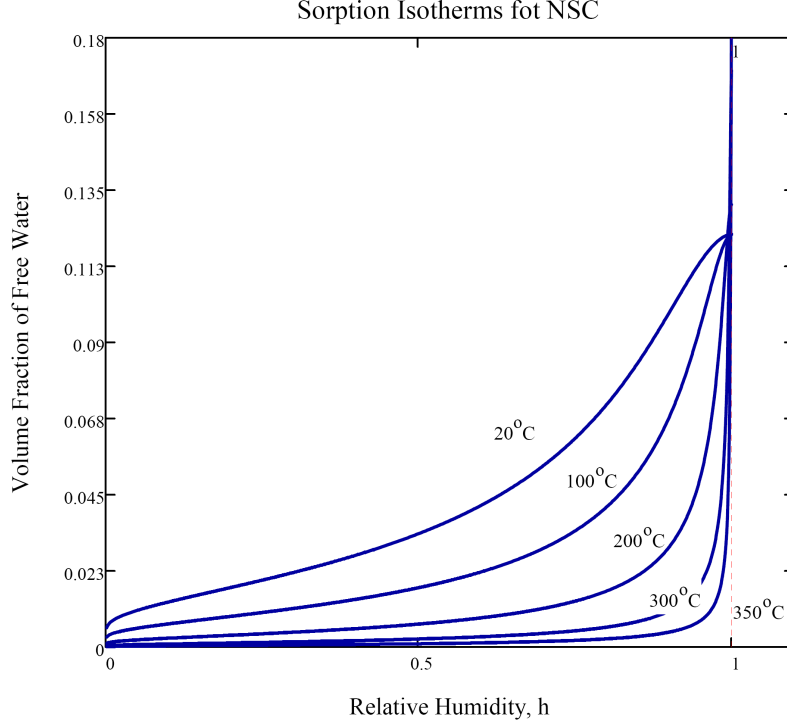
Figure 3.7.: New sorption isotherms for NSC for various temperatures.

$$P_C\left(S\right) = \gamma\left(T\right) J_{BB}\left(S\right) \sqrt{\frac{\phi\left(T\right)}{K\left(T\right)}} \tag{3.63}$$

Finally, combining Equation (3.63) with Kelvin's equation (3.57), yields the critical relationship (3.64) between the free water content and the relative humidity required to complete the model for elevated temperatures.

$$\varepsilon_{FW} = \varepsilon_{FW}\left(h, T\right) \tag{3.64}$$

The new sorption isotherms are shown for the appropriate concrete mix in Figure 3.7 for NSC and in Figure 3.8 for HSC for different temperatures. The isotherms are based on several temperature dependent properties, including porosity, intrinsic permeability and surface tension. The temperature dependency of the surface tension of water in contact with its vapour is well known (see e.g. [7, 47]) and is given by Equation (3.65) and shown in Figure 3.9. The function starts at the value of $72.8\frac{\text{mN}}{\text{m}}$ for 20°C and is approaching 0 when the temperature is approaching to the critical point of water. The
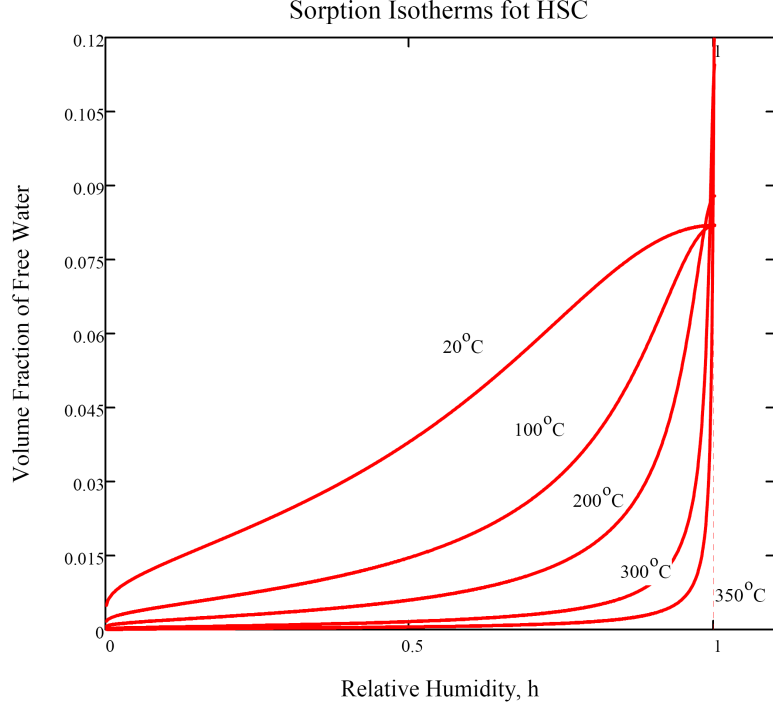
Figure 3.8.: New sorption isotherms for HSC for various temperatures.

rest of the parameters need some more insight and explanation, which will be provided in the following sections (3.4.2, 3.4.3).

$$\gamma = 235.8 \left(1 - \frac{T}{T_{cr}}\right)^{1.256} \left[1 - 0.625 \left(1 - \frac{T}{T_{cr}}\right)\right] \frac{\text{mN}}{\text{m}} \qquad (3.65)$$

where T_{cr} is a temperature at the critical point of water, and both temperatures are expressed in degrees Kelvin.

When comparing the sorption isotherms for the two types of concrete, NSC and HSC, a similar behaviour can be observed up to certain level of relative humidity. However, at the high concentration of relative humidity their behaviour is completely different. This is demonstrated in Figure 3.10. The HSC function seems to be stabilising, whereas the NSC function records sudden increase. Such difference in behaviour is important, when looking into details at fire situation. During the fire conditions there is an increase in water content ahead of the drying front, which corresponds to the high relative humidity level. Thus, a different behaviour of each type of concrete is expected when quickly heated to extreme temperatures.
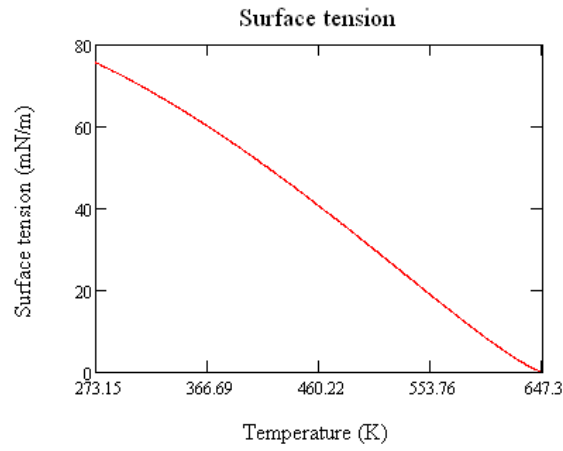
Figure 3.9.: Temperature dependency of surface tension of water
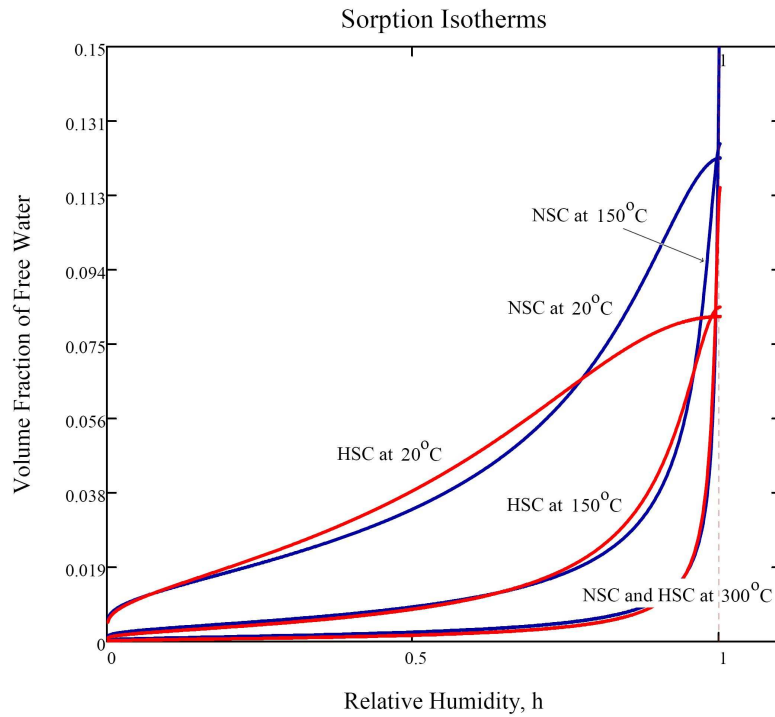
Figure 3.10.: Comparison of Sorption isotherms for HSC and NSC for various temperatures.

3.4.2. Permeability

In the single phase flow, the intrinsic permeability, K, is a measure of a porous material's ability to transport fluid, and in Darcy's law it represents the constant of proportionality:

$$V = -K\nabla P \qquad (3.66)$$

In the multiphase flow, the relative permeability k_i is a dimensionless parameter and is a measure of the effects of permeability of each phase i and varies between 0 and 1. Darcy's law adopted for two phase flow is presented in equations (3.11) and (3.12), which are repeated for clarity below:

$$\mathbf{v}_G = -\frac{Kk_G}{\mu_G}\bigtriangledown P_G$$

$$\mathbf{v}_L = -\frac{Kk_L}{\mu_L}\bigtriangledown P_L$$

The aim of this section is to show the importance of the intrinsic permeability of concrete, as well as the relative permeability of both gas and liquid. Observed differences in experimental measurements of permeability values will be discussed in the following section and possible explanation will be proposed. Afterwards, new functions of relative gas and liquid permeability will be introduced and compared to previously used ones [68] and to experimental data.

3.4.2.1. Intrinsic permeability

Despite the fact that intrinsic permeability (K) is supposed to be an intrinsic material property of porous media (not dependent on fluid), several experimental data [2, 69, 17, 48, 12] shows that its values for concrete can vary, depending on whether air or water is used for its measurements (see for example Figure 3.11). It seems that an intrinsic permeability established using a liquid depends on the media only. However, gases display a permeability that also depends on the type of the gas and the pressure difference across the media. This variation with the type and pressure of the gas is known as slippage or more accurate as *slip flow effect* or the *Klinkenbergs'*
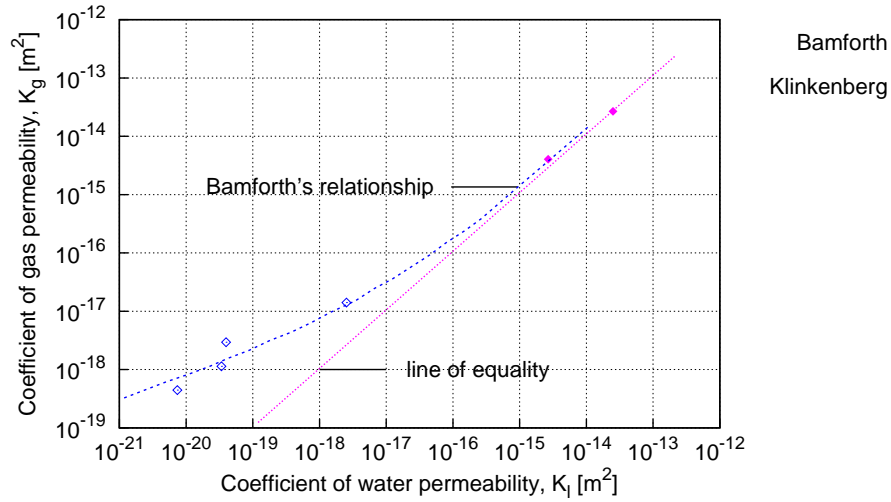
Figure 3.11.: Relationship between gas and water permeability for concrete reproduced from Bamforth [2]

effect [42].

Slip flow effect.   This effect was originally detected with gas flow through capillary tubes (see Figure 3.12). Gas molecules, travelling through capillary tube, collide with each other and with the walls. When a significant number of molecular collisions are with the wall rather than with other gas molecules, the gas permeability is increased by this additional flux due to the gas flow at the wall surface, which is called 'slip flow' effect. Its significance increases when the diameter of the capillary tubes approaches the mean free path of the gas molecule. Therefore, it is expected to have greater effect on low permeability porous media, e.g. concrete and HSC in particular. This effect results in a deviation from the intrinsic liquid-based permeability.

One of the reasons why this effect is not captured in the formulation presented so far may be a consequence of Darcy's law. This is based on the laminar flow theory, which implies that there are non-slip boundary conditions on the interface of solid and fluid, thus zero fluid velocity at the boundaries.

It seems essential to take into account the effect of slippage into the existing model to obtain proper results. Klinkenberg [42] shows that this phenomenon was found to be quite significant for low permeability mate-
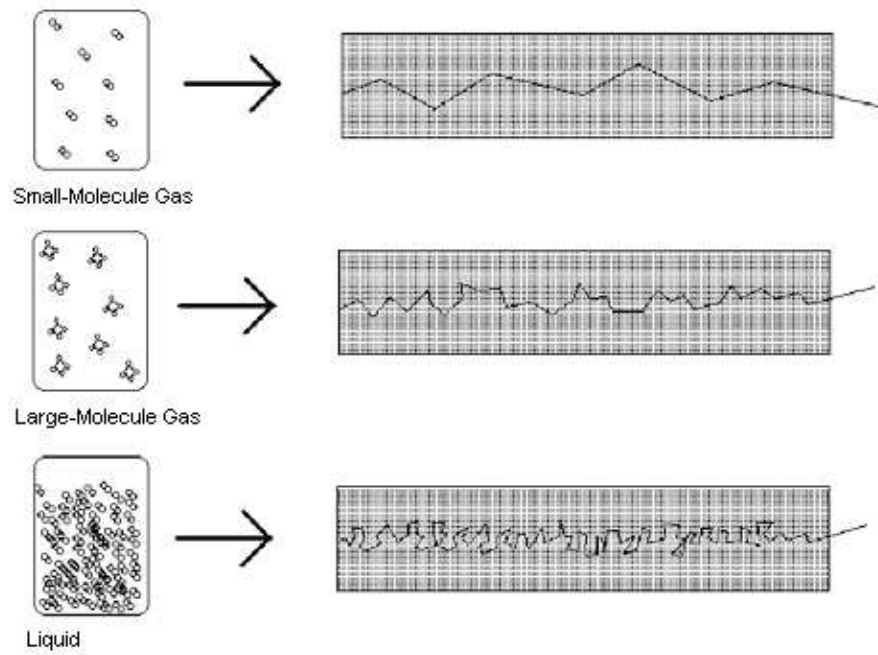
(a) different type of moisture
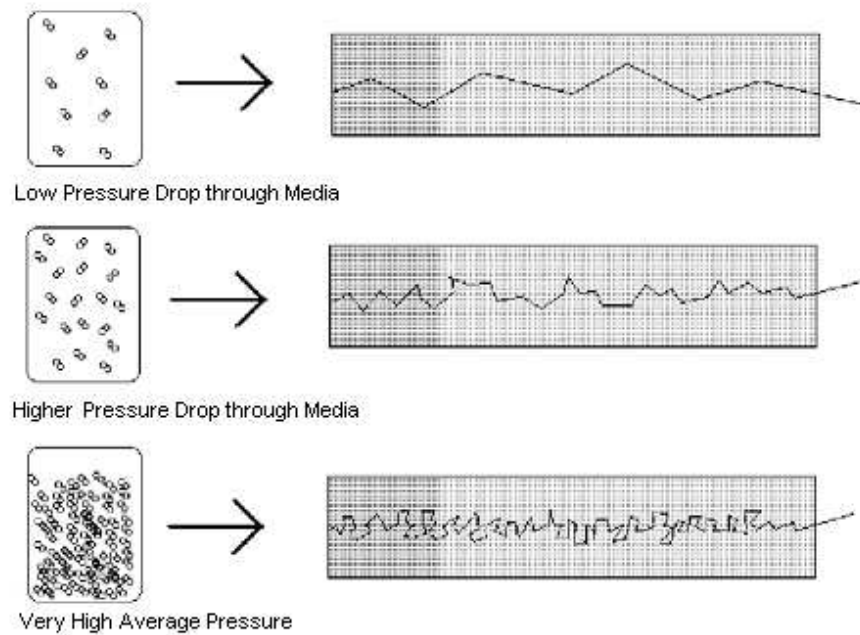
(b) different pressures

Figure 3.12.: The gas flow through capillary tubes, reproduced from Kelley [34]

rials. First, he made experiments with several capillary tubes with different diameters and than he dealt with different types of soils and granulates. Afterwards, he presented the formula (3.67) with the slip correction factor b, whereby the intrinsic permeability for a gas K_G is presented as a modification to the intrinsic permeability for a liquid, K_L:

$$K_G = K_L \left(1 + \frac{b}{P_{AVG}} \right) \tag{3.67}$$

where P_{AVG} is the average pore pressure and b is a constant for a given gas and a given porous medium.

As concrete is a low permeability medium it seems appropriate to use this kind of approach. Bamforth [2], who undertook experiments on concrete samples and presented a single relationship for b (3.68) that is applicable for both his and Klinkenberg results. Slightly different constant b (3.69), which is proposed by Chung [12], is based on the experimental results from Bamforth [2], Klinkenberg and Whitting[69]. Therefore, this more comprehensive approach is incorporated in the Enhanced Glasgow model.

$$b = 1.635 \cdot 10^{-8} K_L^{-0.5227} \, [Atm] \tag{3.68}$$

$$b = e^{(-0.5818 ln(K_G) - 19.1213)} \, [Atm] \tag{3.69}$$

The effect of different values for b on intrinsic permeability are shown in Figure 3.13.

Relationship (3.69) was incorporated into the Enhanced Glasgow Model. At initial time step, gas permeability is assumed to be equal to the liquid permeability (K_G without taking account of slippage effect), then b is determined through (3.69), and finally new K_G is obtained:

$$K_G^{new} = K_G^{initial} \left(1 + \frac{b(K_G^{initial})}{P_G} \right) \tag{3.70}$$

Figure 3.13 shows that for K_G above the level of 10^{-14} the gas slippage effect is negligible.

All the benchmark problems presented and discussed in Chapter 4, use this approach. The intrinsic permeability for two types of concrete were ob-
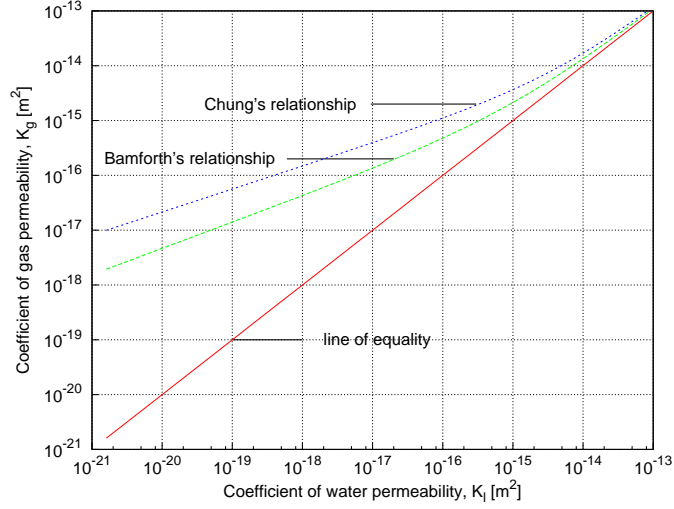
Figure 3.13.: Slippage effect

tained through comparison of the published experimental results and computed results. These values were than used during subsequent computations of the other benchmark problems.

Damage is a measure of the deterioration of the elastic moduli due to the evolution of the mesostructure, resulting in increasing pore space. Here, a scalar damage model is adopted and the scalar damage parameter comprises both mechanical and thermal damage. A multiplicative decomposition of damage is adopted, following Stabler [64] and Gawin et al. [22]:

$$D = 1 - (1 - \chi)(1 - \omega) \tag{3.71}$$

where ω is mechanical damage and χ is thermal damage.

The dependence of the elastic moduli E on damage can be expressed as:

$$E = (1 - D)E_0 \tag{3.72}$$

where E_0 is the undamaged elastic moduli.

Although there is very limited data in the literature on the influence of temperature on intrinsic permeability, due to difficulty in obtaining reliable experimental data (with exception of Schneider [62]), there is some work relating intrinsic permeability to damage.

One of these approaches is presented by Gawin et al. [23]:

$$K = K_0 \cdot 10^{A_K(T-T_0)} \left(\frac{P_G}{P_0} \right)^{B_K} \cdot 10^{\alpha\omega} \tag{3.73}$$

where A_K and B_K are constants depending on the type of concrete, K_0 is the undamaged intrinsic permeability, T_0 represents room temperature, α is a scaling parameter, ω is a mechanical damage parameter.

In (3.73) the effect of thermal and mechanical damage are accounted for differently than the approach presented at the beginning of this section.

Therefore, a more straightforward approach is adopted in this work, based on the work of Bary [4], where intrinsic permeability depends on total damage D:

$$K = K_0 \cdot 10^{\alpha D} \tag{3.74}$$

where D is a total damage parameter, α is a scaling parameter, χ is a thermal damage parameter and ω is a mechanical damage parameter.

Although this relationship depends on total damage, it has been calibrated with experimental data, assuming thermal damage only. To achieve this, the thermal damage parameter is described as a function of temperature:

$$\chi = 2 \cdot 10^{-3} \left(T_{max} - T_0 \right) - 1 \cdot 10^{-6} \left(T_{max} - T_0 \right)^2 \tag{3.75}$$

where T_0 represents room temperature and T_{max} is the maximum temperature reached.

This relationship has been derived from experimental data on the effect of temperature on the elastic modulus of concrete [55]. After substituting (3.75) into (3.71), with $\omega = 0$, (6.46) can be compared against available experimental data [62] for intrinsic permeability as a function of temperature, using a scaling parameter $\alpha = 4$ [31]. This is presented in Figure 3.14.

3.4.2.2. Relative permeability [12, 48]

The complete description of the moisture multiphase flow inside heated concrete also requires a proper description of the interactions between the moisture phases. To model this interaction phenomena, there is a need for an accurate definition of the relative permeabilities for gas and liquid. The functions used within the original Glasgow model are based on van

3.   Modelling of transport phenomena in concrete at high temperature
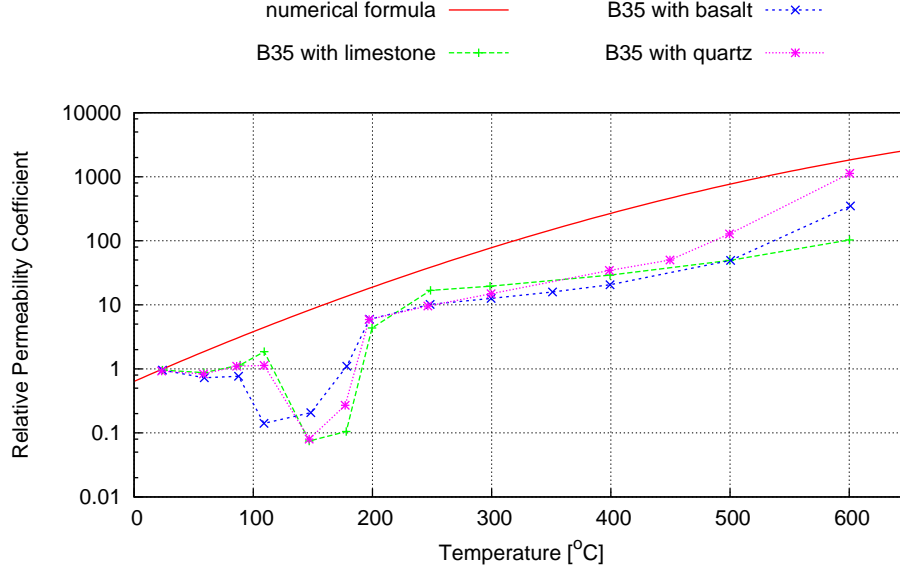
Figure 3.14.: Intrinsic permeability as a function of temperature. Assumed fit compared to experimental data [62].

Genuchten [68] and are presented in equations (3.76) and (3.77):

$$k_L = \sqrt{S}\left(1 - \left(1 - S^{\frac{1}{m}}\right)^m\right)^2 \tag{3.76}$$

$$k_G = \sqrt{1 - S}\left(1 - S^{\frac{1}{m}}\right)^{2m} \tag{3.77}$$

These relationships were established for soils and the gas relative permeability function is almost linear (see (3.15)). As soils have a different micro-structure than concrete, than these relationships may not be appropriate. Recently, the modified van Genuchten functions (3.78 and 3.79) were introduced by Monlouis-Bonnaire et al. [49], based on curve fitting of concrete experimental data (see Figure 3.16):

$$k_L = S^p\left(1 - \left(1 - S^{\frac{1}{m}}\right)^m\right)^2 \tag{3.78}$$

$$k_G = (1 - S)^p\left(1 - S^{\frac{1}{m}}\right)^{2m} \tag{3.79}$$

where $p = 5.5$ and $m = 0.56$.

The experimental data shows that relative permeability of gas is decrea-

66
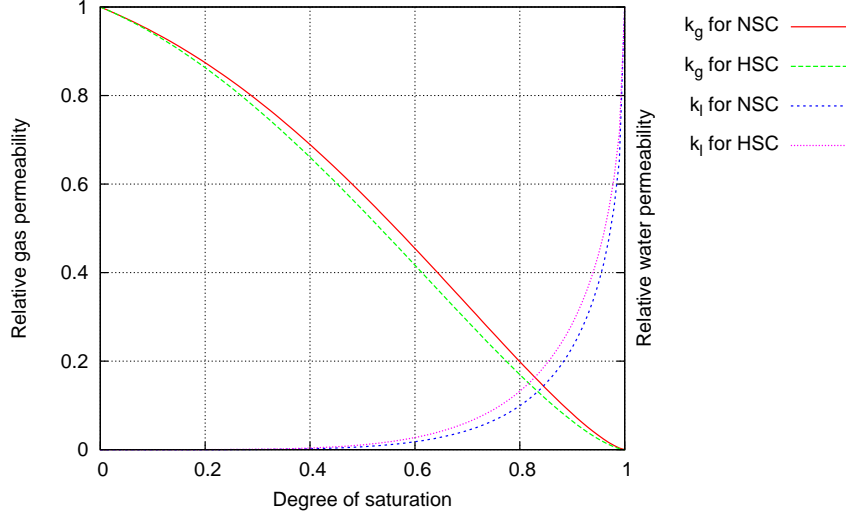
Figure 3.15.: Relative water and gas permeability for NSC and HSC based on [68]

sing in a non-linear manner with increasing saturation. This can be explained by the fact that as more fluid is available in the system, gas can be trapped or flow is inhibited. As the proposed functions are not dependent on the type of concrete, care must be taken in using this approach until such a dependency is introduced.

The relative permeability functions (3.80 and 3.81) that are porosity dependent can be found in Chung and Consolazio[12] (see Figure 3.17). They were developed for cementitious materials, based on experimental test results of Jacobs (reference 27 from Chung and Consolazio [12]). The concrete specimens at various states of partial liquid saturation were subjected to gas permeability tests and relative permeability values for gas flow were determined.

$$k_G \left(S, \phi \right) = 10^{S(0.05 - 22.5\phi)} - 10^{(0.05 - 22.5\phi)} S \qquad (3.80)$$

$$k_L \left(S, \phi \right) = k_G \left((1 - S), \phi \right) \qquad (3.81)$$

The authors in [12] stated that, as the thermally driven moisture flow through concrete is primarily influenced by gas phase flow, the gas relative permeability k_G is more influential and the liquid one can be simplified to a function symetrical with respect to saturation equal 50%. However, this

approach is not experimentally supported and so once again, care must be taken in using these functions.

One idea is to introduce a concrete mix dependency into the Monlouis-Bonnaire et al. [49] functions, based on the Baroghel-Bouny parameters. Another one is to use the relative permeabilities from Chung and Consolazio [12]. However, as Chung and Consolazio [12] used mirrored gas function for liquids, a mixed approach can be used were the relative permeability for gas is taken from [12] and the liquid relative permeability from van Genuchten [68].

All three approaches are incorporated into the Enhanced Glasgow model, as it seems more appropriate to use these new functions in computations, rather than the one established for soils [68]. When looking at the results, presented in Chapter 4, and comparing with the previously obtained when using only van Genuchten functions, there are some differences in the model response, especially in the gas pressure, which is a crucial variable when calculating the mechanical part of the analysis. All of the modified relative permeability functions give comparable results, but it seems that the porosity based functions (3.81, 3.80) are more general than the others. This will be discussed in Chapter 4.

At this particular point there is a need to discuss part of the work of Gawin et al. [22], connected with the liquid mass flux equation. The mass flux presented in their work (3.82) is decomposed into two components: the liquid water flux and the absorbed water flux:

$$\mathbf{J}_L = \left(1 - \frac{S_B}{S}\right)\varepsilon_L\rho_L\mathbf{v}_L + \left(\frac{S_B}{S}\right)\varepsilon_L\rho_L\mathbf{v}_B \qquad (3.82)$$

where S_B is a degree of saturation, $\mathbf{v}_B$ is the velocity of the adsorbed water due to diffusion.

It is assumed there that moisture entering a dry sample of concrete will initially fill the gel pores and adhere to the surface of capillary pores as adsorbed water, up to a maximum volume, before the remaining capillary pore space fills with liquid water. The degree of saturation with adsorbed water, S_B, is defined as (3.83):
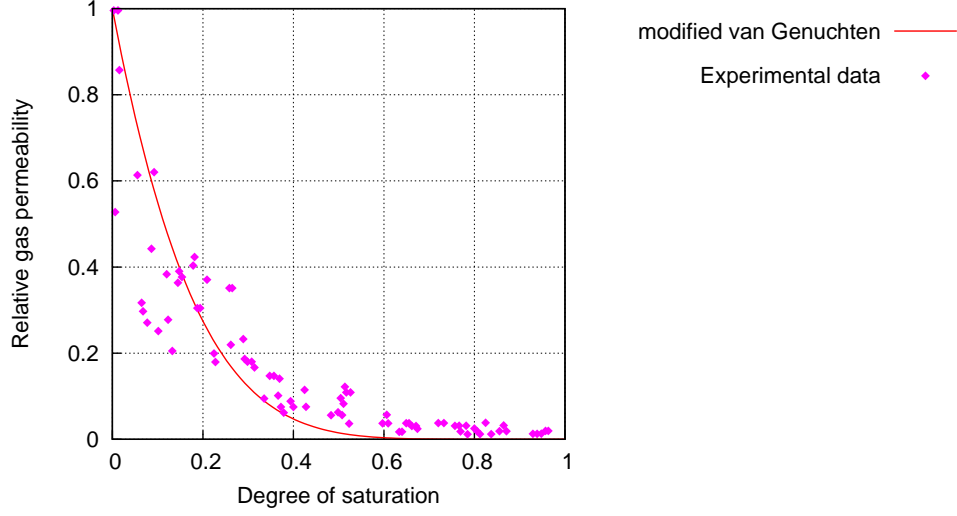
Figure 3.16.: Gas relative permeability function based on [49]

$$S_B = \begin{cases} S & \text{for } S \leq S_{SSP} \\ S_{SSP} & \text{for } S > S_{SSP} \end{cases} \tag{3.83}$$

where S_{SSP} is the solid saturation point.

The solid saturation point is the upper limit of the hygroscopic moisture range and the maximum degree of saturation with adsorbed water is achieved at this level.

In [22], the value for solid saturation point seems to be chosen arbitrarily as 0.55 without any specific explanation. Accounting for adsorbed water in this way, means that for levels of saturation below the solid saturation point ($S \leq S_{SSP}$), the liquid flow (3.82) is very small. However, it is advocated here that this effect is already accounted for in the relative permeability. This can be seen in Figures 3.15 and 3.17. Up to the saturation levels of approximately 0.5, the value for k_L is very low. After this point, k_L increases dramatically, for values $S > S_{SSP}$. Therefore, Gawin's approach [22] will not be adopted here.
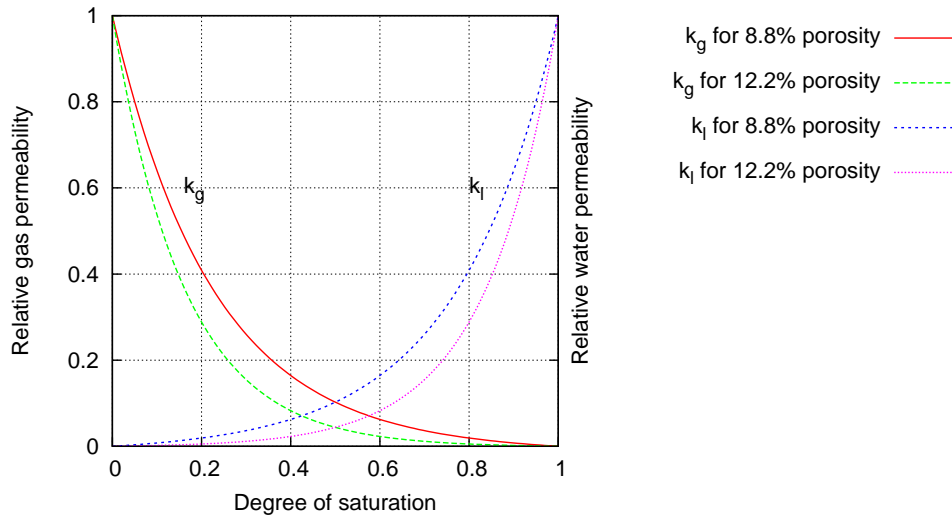
Figure 3.17.: Relative permeability functions from [12]

3.4.3. Additional physics and thermodynamic properties of fluid and heat flow in concrete at high temperatures

The general approach to the description of processes during mass and heat transfer in a porous media starts from appropriate set of differential equations, then it is supplemented with the constitutive equations and finally the thermodynamic equilibrium equations are introduced. The parametric relationships that are required for an analysis of concrete behaviour at high temperatures are presented in Appendix D. Some of the presented equilibrium equations can be regarded as the equation of state, which express the relationship between the thermodynamic variables and their spatial variations at the point of thermodynamic equilibrium. Essentially, they are allowing for the closed form solution of the system. The presented parameters are consistent for all analysis presented in this thesis.

3.5. Summary of Models

Key factors that differentiate the models to be discussed are summarised in the table below.

MODEL NAME	SORPTION ISOTHERMS	GAS SLIP EFFECT	RELATIVE PERMEABILITY	ADSORBED WATER
Tenchev [65]	Bazant's [7]	No	Eq. (3.76) and (3.77)	No
Original Glasgow [15]	Bazant's [7]	No	Eq. (3.76) and (3.77)	Yes
Enhanced Glasgow (this thesis)	Leverett based	Yes	Eq. 3.80 and 3.81 or Eq. 3.78 and 3.79	No*

Note: * Adsorbed water flow is not included explicitly, but it is taken into account in the relative permeability formulation

Table 3.4.: Summary of discussed models

4. Model validation

Model verification and validation are the main aspects of a successful development of simulation codes. Unfortunately, there are no specific algorithms, techniques or procedures that guarantee the successful determination whether the model is correct or not. The verification of the presented transport model has been done by a walk-through technique consisting of statement-by-statement analysis of the code structure, when running analyses. Next, the validation against experimental results was made, using three benchmark problems:

1. A drying problem

2. A column subjected to fire conditions

3. A simulation of the heated concrete slab

The first is a drying problem, based on Baroghel-Bouny et al. experiment [3] and the results are presented in section 4.1. This benchmark problem demonstrates the ability of the Enhanced Glasgow model to simulate the transport problem under ambient conditions. It validates the mass loss and moisture distribution during ambient conditions.

The second benchmark problem is a column subjected to fire conditions, which is presented in section 4.2. The results obtained from the fire problem are compared with the results provided by an existing model, presented by Tenchev et al. [65]. It validates the new sorption isotherms, as well as the new permeability formulations.

The third benchmark problem is the simulation of the heated concrete slab, following the experiments of Kalifa et al. [33]. The slab is subject

to heating conditions up to temperatures of 600°C. It validates the ability of the model to capture all the physical phenomena within concrete, when subjected to high temperatures, like moisture clog and pressure built-up, while maintaining the adequate mass lose.

All the presented analyses have a consistent set of variables, which are listed in Appendix D.

The presented process is believed to be sufficient to validate the Enhanced Glasgow model. The outcome of this processes is summarised in the last section of this chapter.

4.1. Benchmark problem 1 - Drying problem

All concrete structures experience a moisture transport within their life cycle. Generally, the transport processes occur when the structure is subjected to a lower environmental relative humidity than its internal state and causing the drying process to evolve. Therefore, the first validation of the model against experimental results is performed using the results presented by Baroghel-Bouny et al. [3], for the drying of different types of concrete. The authors highlight the importance and significance of the sorption isotherms and describe it as *a key parameter in the modelling of drying process.*

During the experiment, the authors measured the moisture content distribution in samples subject to drying, where normal and high strength concrete were considered. The samples of diameter 0.16 m and height of 0.1
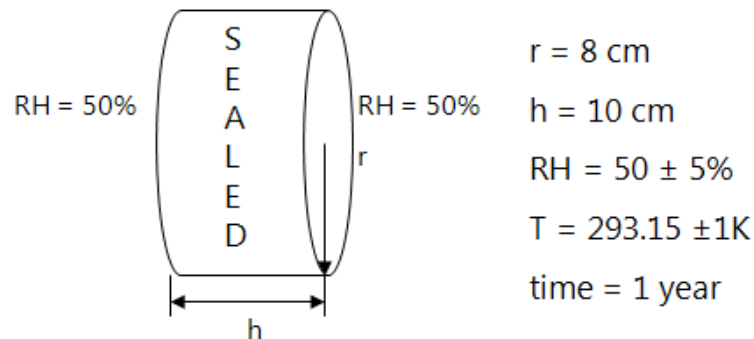
Figure 4.1.: Drying problem

m were subjected to an environmental relative humidity less than the initial internal relative humidity. In order to determine the intrinsic permeability, K, for the different concrete mixes the isothermal drying experiments were simulated numerically and the intrinsic permeability varied until a reasonable match between experimental and numerical results was obtained.

Due to the sealed boundary conditions, the problem can be treated as a one-dimensional transport problem. The experimental and numerical setup is presented in Figure 4.1. Based on the experience of this thesis author, the mesh consisted of 200 elements of 4 noded quadrilaterals.

The boundary conditions are as indicated in Figure 4.1, 50% relative humidity, temperature of of 20°C and uniform gas pressure equal to atmospheric gas pressure. During the analysis the relative permeability is calculated based on Chung and Consolazio approach (refer to section 3.4.2.2).

4.1.1. Numerical predictions

During the drying problem validation process the numerical simulations for two types of concrete are considered. The concrete specimens were dried for 1 year, corresponding to a relative humidity of 94% for normal concrete and 69% for high strength concrete. Then, the two specimens are subjected, for a one year period, to an external relative humidity of 50%. Weight loss and relative density variations were measured. The set of variables used during the analysis can be found in Appendix D.

The intrinsic permeability was varied to provide the best fit with experimental data. The comparison between the obtained numerical results for the relative weight loss over time with the experimental results of Baroghel-Bouny et al. [3] is presented in Figure 4.4. The intrinsic permeabilities determined are summarised in Table 4.2, together with the values obtained by Baroghel-Bouny et al. through simplified numerical simulation, which was based on Coussy's approach [13]. It can be seen that although the values obtained by the two numerical techniques are dissimilar, they are of similar orders of magnitude. The values for normal strength concrete are higher than for high strength concrete, as expected.

In addition to the overall relative weight loss of the specimens, the water content profiles were experimentally determined using gamma-ray attenua-

	Mix	
	NSC	HSC
$K(m^2)*$	3×10^{-21}	5×10^{-22}
$K(m^2)**$	15×10^{-21}	5×10^{-21}

Table 4.2.: Parameters for (3.54) and corresponding porosity (ϕ) for different concrete mixes following [3].
Notes:
$*$ Values obtained by Baroghel-Bouny et al. [3]
$**$ 'Best fit' parameters for the Enhanced Glasgow model

tion measurements. Figure 4.2 shows a comparison of the experimentally obtained profiles for NSC with the numerical predictions of the Enhanced Glasgow model. The results for high strength concrete are presented in Figure 4.3 for completeness, however they are less clear. The final state of relative humidity for ordinary and high strength concrete were 91% and 68%, respectively. This correlates well with the experimental results.

It is interesting to note that the presented numerical results are in very good agreement with the experimental results and are more encouraging than the numerical results reported by Baroghel-Bouny et al. [3].

4.1.2. Discussion

The Enhanced Glasgow model is able to predict the presented drying problem accurately. As mentioned by Baroghel-Bouny et al. [3], the key parameter of such drying conditions is the sorption isotherm, which quantifies the water-solid interaction. Additional parameters as the porosity and intrinsic permeability of the material are also necessary to predict the hygral state of a porous material. The calculated moisture profiles presented for both concrete types agree very well with the profiles obtained experimentally. In addition, the results show a very different behaviour between the normal and high strength concrete.
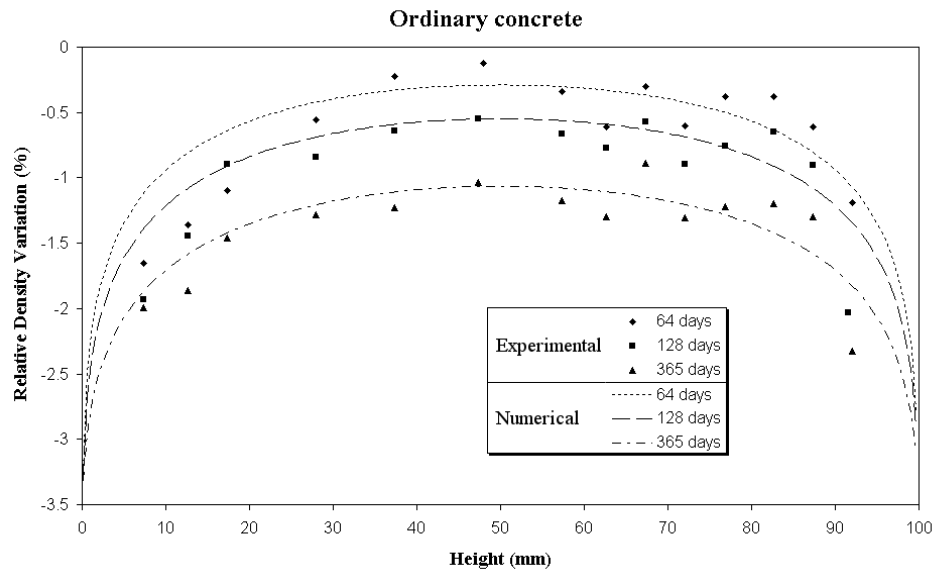
Figure 4.2.: Relative density variation as a function of height of the specimen for NSC
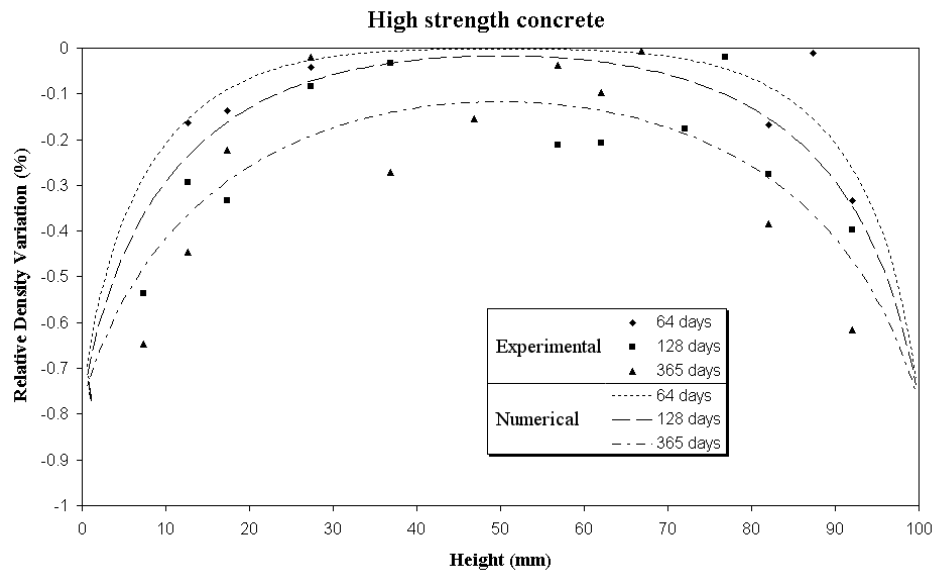
Figure 4.3.: Relative density variation as a function of height of the specimen for HSC
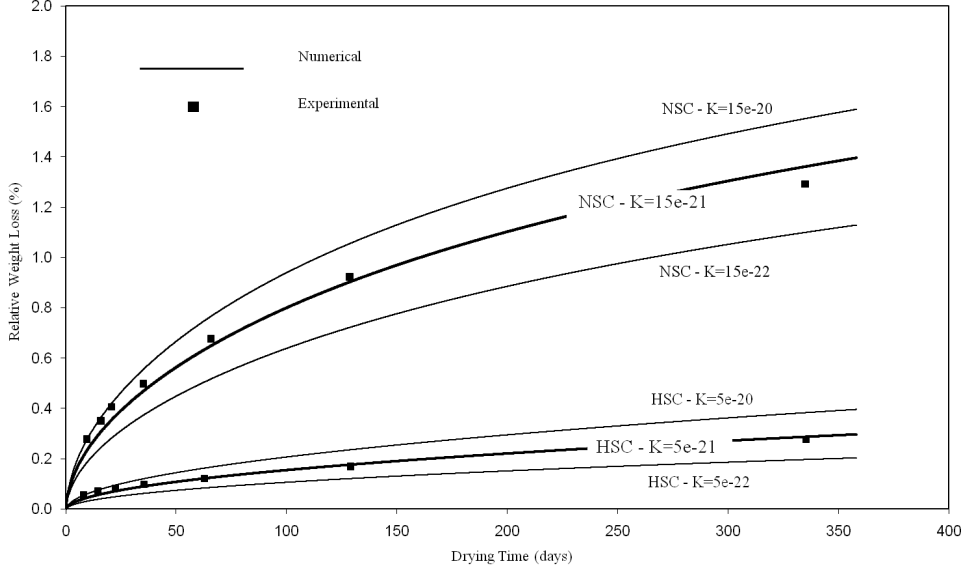
Figure 4.4.: Relative weight loss for Normal and High Strength Concrete

4.2. Benchmark problem 2 - Column subjected to fire

The next benchmark problem, which is illustrated in Figure 4.5, represents a rectangular column exposed to fire conditions. The numerical model represents a two-dimensional column section of 0.2 m in length and of arbitrary width. The problem is essentially a one-dimensional transport problem, where temperature, pore pressure and water content are being computed. On the outside surface of the column the ISO 834 standard fire curve (see Equation (4.1) and Figure 2.1 in Chapter 2), representative of an intense fire for a period of 1 hour is applied to the environmental temperature. In addition, the gas pressure is defined as 0.1 MPa and an approximate value for the environmental vapour content is set to 0.8 of the initial conditions. The environmental temperature and vapour content conditions are imposed via flux boundary conditions (see section 3.3)

The initial internal conditions for the concrete were a uniform temperature, T, of 20°C, uniform gas pressure, P_G, equal to 0.1MPa, and a uniform initial vapour content, $\tilde{\rho}_V^0$, as shown in Equation (3.49) such that, through the ideal gas law(3.48), the vapour pressure, P_V, was equal to the saturation pressure of water vapour, P_{Sat}. It may be noted that this was based on the

initial relative humidity within the concrete pores as 95%. The rest of the variables used during the analysis can be found in Appendix D.

$$T_\infty = 293.15 + 345log_{10}(8t + 1) \tag{4.1}$$

The analysis is a reproduction of the problem from Tenchev et al. [65] and Davie et al. [15]. The same solution scheme as in the latter is being used, which was an iterative, central difference time stepping algorithm with 0.5 second time step and limited to 10 iterations. The convergence criteria is set at the level of 10^{-6} for the energy norm. Based on the experience from the mentioned publications, 200 elements mesh of 8 noded quadrilaterals is chosen.

Concrete material parameters are taken to be similar to Tenchev et al. [65], to validate the model and to obtain comparable results.

4.2.1. Numerical results

The presented numerical analyses were undertaken to compare the different sorption isotherm formulations of Bazant in Tenchev's model and Leverett based used in Enhanced Glasgow model. Additionally, the different relative permeability presented in section 3.4.2.2 are tested and compared. Therefore, results from the Enhanced Glasgow model with different relative permeability relationships, is compared with the original Tenchev's model. In summary, the following four analyses were undertaken:

Analysis 1 Enhanced Glasgow model with relative permeability according
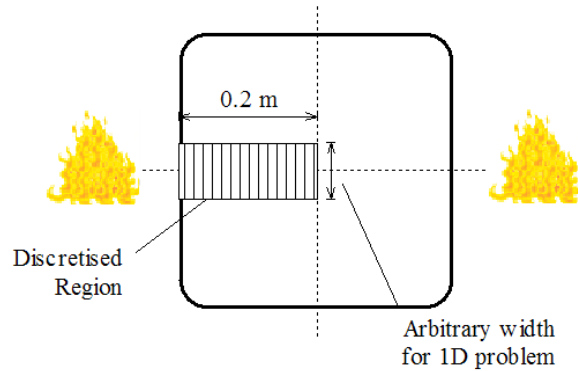
Figure 4.5.: Column subjected to fire conditions

to Manlouis-Bonnaire et al. [49] with parameters from Baroghel-Bouny et al. [3] - eq. 3.78 and 3.79

Analysis 2 Enhanced Glasgow model with relative permeability according to Chung & Consolazio [12] - eq. 3.80 and 3.81

Analysis 3 Enhanced Glasgow model augmented by relative permeability based on van Genuchten formulation, following [15] - eq. (3.76) and (3.77)

Analysis 4 Reproduction of original Tenchev's model[65, 15] - Bazant's sorption isotherms and van Genuchten relative permeabilities

The first check for all the discussed analyses is a study of the moisture mass conservation within the system. During the heating process moisture is transported through the model boundary to the environment. It is necessary that the numerical model can demonstrate a balance between the loss of the mass of moisture in the interior of the discretised zone and the total mass of the vapour passing through the boundary. For illustration, the moisture mass balance graph is presented in Figure 4.6 for the Analysis 1 where it can be seen that mass balance is achieved. All the analysis produce a similar graph, what gives an indication that the model is behaving well and the numerical implementation is correct.

All the analyses undertaken show a similar pattern of temperature, porosity and intrinsic permeability, as can be seen in Figure 4.7. This is due to the fact that except for the relative permeability formulations, all the transport properties were taken the same and it is expected they will achieve similar results.

Figure 4.7 also shows that the vapour pressure never exceeds the saturation vapour pressure, as expected. This is not the case for Analysis 4 (Tenchev's model), where relative humidity can exceed 100%. This is better illustrated in Figure 4.8, comparing relative humidity after 1 hour of fire for all analyses.

Of a particular interest is the fact that all the analyses show a steep drying front zone (Figure 4.8). On one side - the 'hot' side - of the zone there is an increased amount of the vapour content (Figure 4.9) and decreased amount of liquid content (Figure 4.12), and on the 'cold' side the reverse situation
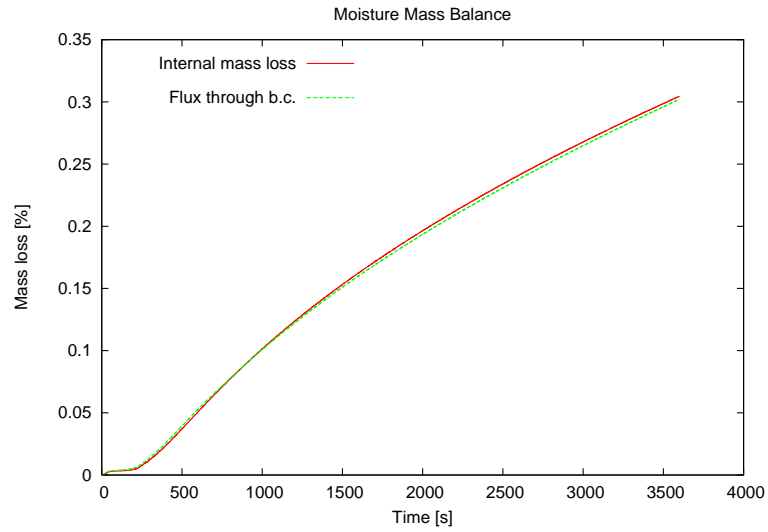
Figure 4.6.: Percentage of total mass of moisture lost from the interior of the discretised region and flux of vapour through the boundary
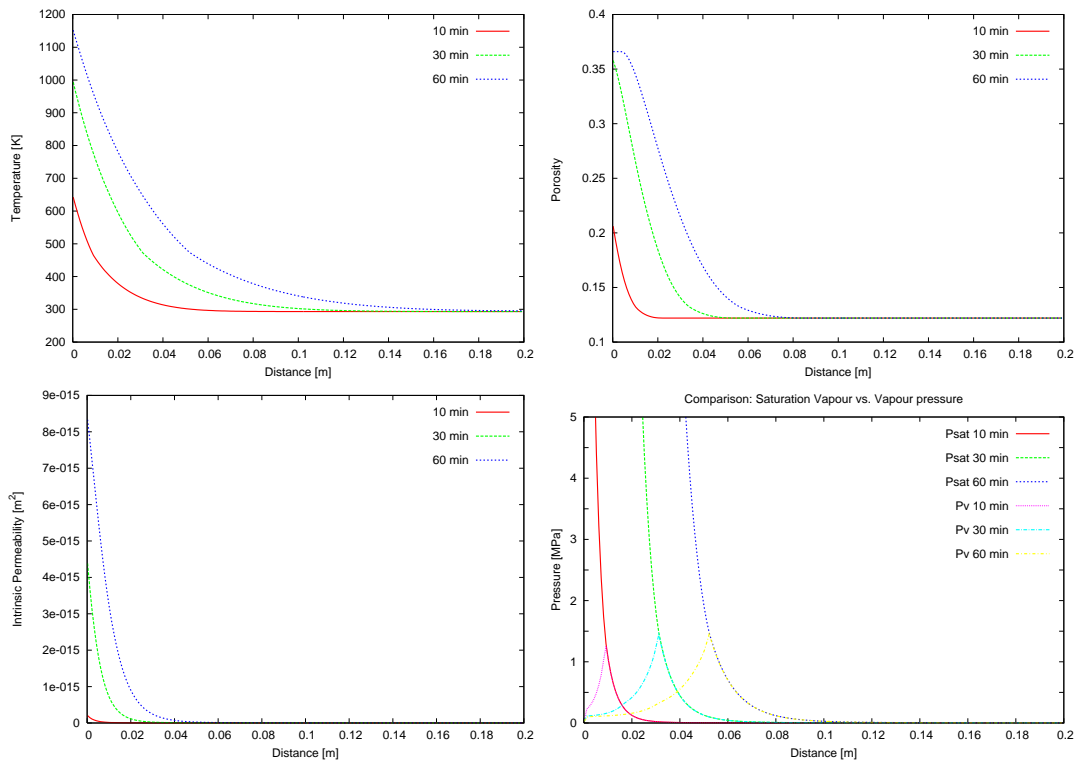
Figure 4.7.: Results from Analyses 1 showing temperature, porosity, intrinsic permeability and vapour pressure, All the results are shown against distance from the exposed surface for 10, 30 and 60 minutes fire
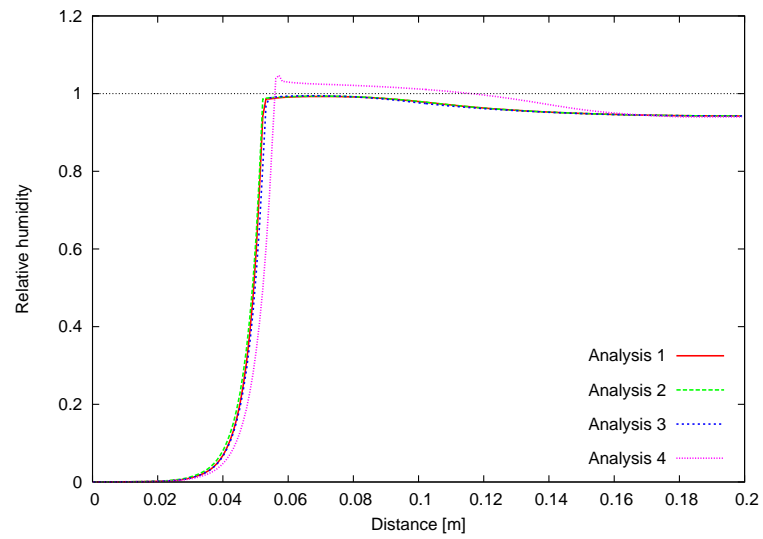
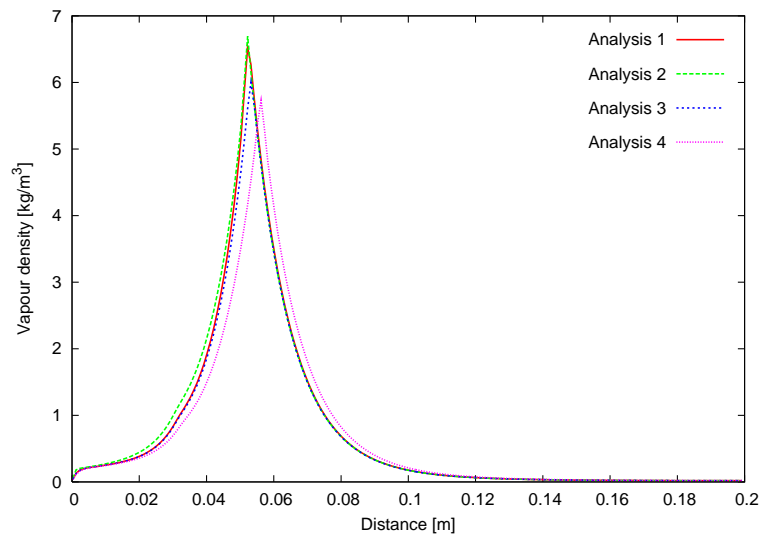Figure 4.8.: Results for relative humidity for analyses 1,2,3 and 4 against distance from the exposed surface after 1 hour of exposure to fire

Figure 4.9.: Vapour content results for analyses 1,2,3 and 4 against distance from the exposed surface after 1 hour of exposure to fire
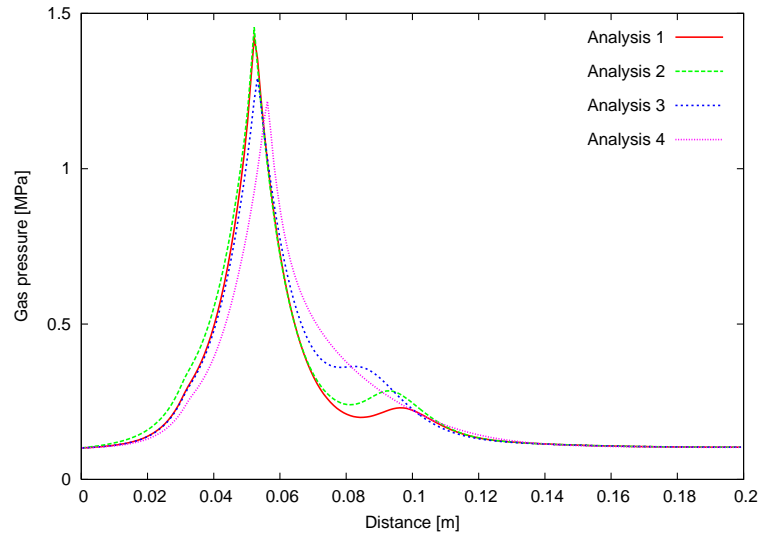
Figure 4.10.: Gas pressure results for analyses 1,2,3 and 4 against distance from the exposed surface after 1 hour of exposure to fire

is observed. Furthermore, it can be noted that there is an increase in water content ahead of the drying front, which is often referred to as the "moisture clog zone".

The increased levels of saturation - the 'moisture clog' zone have been observed by many authors ([15, 65, 22, 40]). This effect reduces the gas relative permeability, thereby inhibiting gas flow ahead of the drying front. The consequence is a dramatic increase in the gas pressure just behind the drying front (Figure 4.10). It is thought that this is a major contributor to observed spalling (see earlier section 2.1.4).

It can be seen that the peaks of the gas pressure (see Figure 4.10) and vapour content (see Figure 4.9) profiles are similar for all the cases, however the maximum values for analyses 1,2 and 3 occur at the drying fronts rather than ahead of them as for analysis 4. Corresponding pore pressures are again of equivalent manner, what can be seen in Figure 4.11.

4.2.2. Discussion

In summary, it has been shown that the presented model gives comparable results with respect to the Tenchev model. It can be argued however, that the proposed enhanced model improves the physical reasoning behind initial constitutive laws such as the sorption isotherms and avoids the spurious
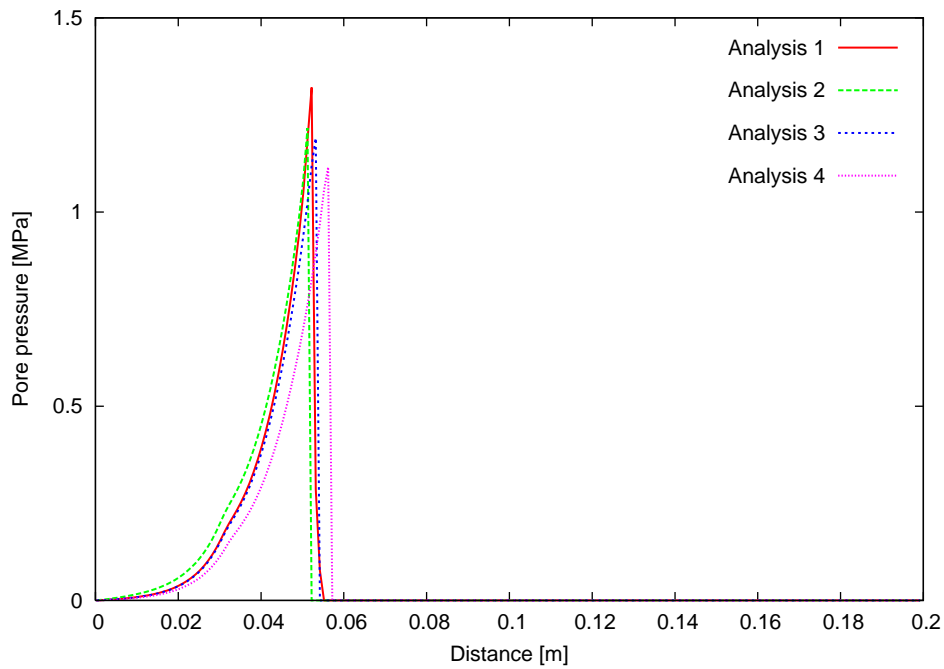
Figure 4.11.: Total pore pressure results for analyses 1,2,3 and 4 against distance from the exposed surface after 1 hour of exposure to fire
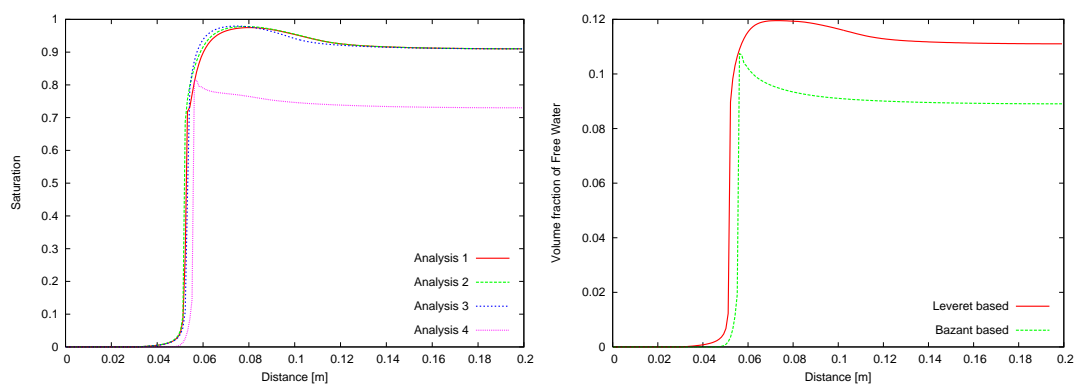
Figure 4.12.: Results for saturation (left) and volume fraction of free water (right) for analyses 1,2,3 and 4 against distance from the exposed surface after 1 hour of exposure to fire
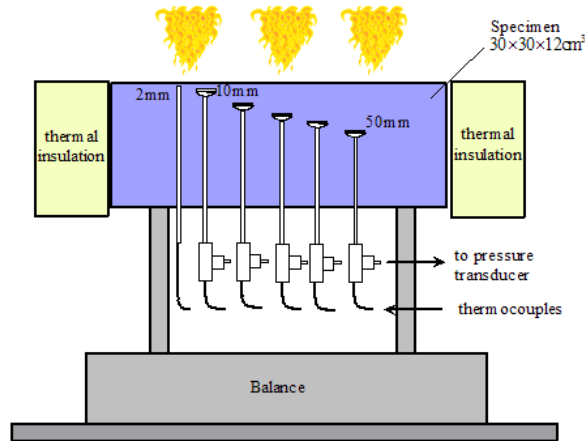
Figure 4.13.: Experimental set-up for Kalifa's problem

levels of relative humidity in excess of 100% observed in the original Tenchev model. It also includes important phenomena, like capillary pressure, or adsorbed water movement leading to better prediction of the pore pressure values.

4.3. Benchmark problem 3 - Heating problem

The additional validation of the model against experimental results is performed using data from Kalifa et al. [33]. The experimental setup is shown in Figure 4.13. Concrete samples, with a prismatic shape (0.3 x 0.3 x 0.12 m3), were subjected to thermal loading on the upper face, while the four lateral faces were thermally insulated. The imposed temperature reached 600°C (873.15K) and the heating duration was 6 hours. The validation presented in this chapter, consists of numerical simulations of the experimental tests based on the high-strength concrete (HSC) data. The problem is considered as unidirectional and consequently, the simulations are made on a slice of concrete of unit width and length of 0.12m (see Figure 4.14). The initial state of the concrete sample is characterised by a temperature of 25°C (298.15K) and a relative humidity of 69%. The rest of the variables used during the analysis can be found in Appendix D.

The validation is restricted to the comparison for the temperature, gas pressure and mass loss, as these were the measured quantities provided by the experimental report. Figure 4.15 compares the experimental results for
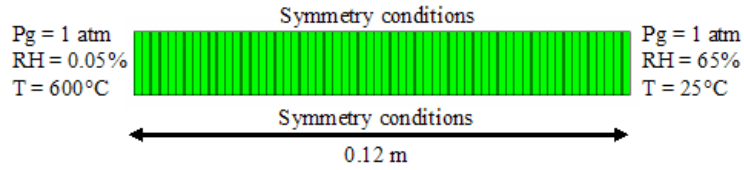
Figure 4.14.: Finite element mesh showing dimensions and boundary conditions
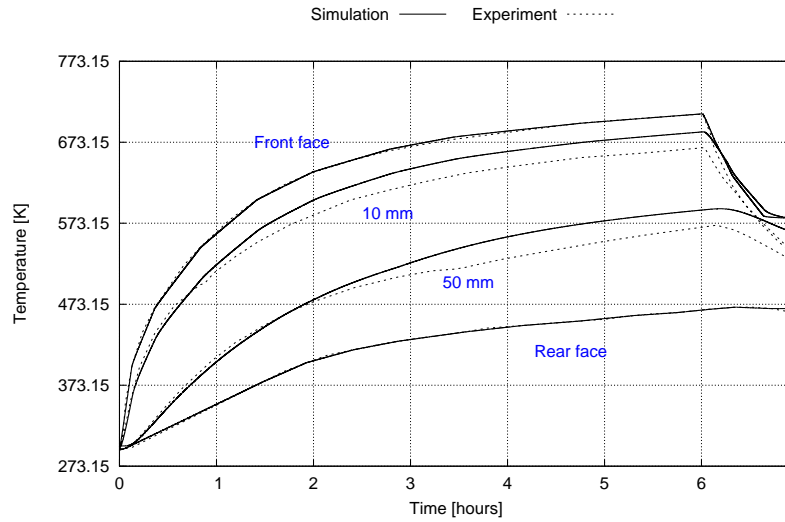

Figure 4.15.: Temperature profiles – comparison of simulation and experimental results

the temperature at different depths with those of the numerical simulations and shows a good qualitative and quantitative agreement. The gas pressure profiles at various depths for the numerical simulations are shown in Figure 4.16a and for the experiments in Figure 4.16b.

When comparing those results it can be seen that there is a reasonable qualitative and quantitative agreement. A maximum value of experimentally measured gas pressure is 3.67 MPa, where the simulated one is slightly lower at 3.51 MPa. The peak values are rising with the distance from the heat source in both the simulation and the experiment. The times at which the gas pressure peaks are recorded for both sets of results are comparable. The experimental gas pressure profiles at 30 mm depth appears out of line with the rest of the results. There might be an influence of the local damage, but it was not reported in the original paper.

Moreover, another good agreement can be seen in Figure 4.17, where
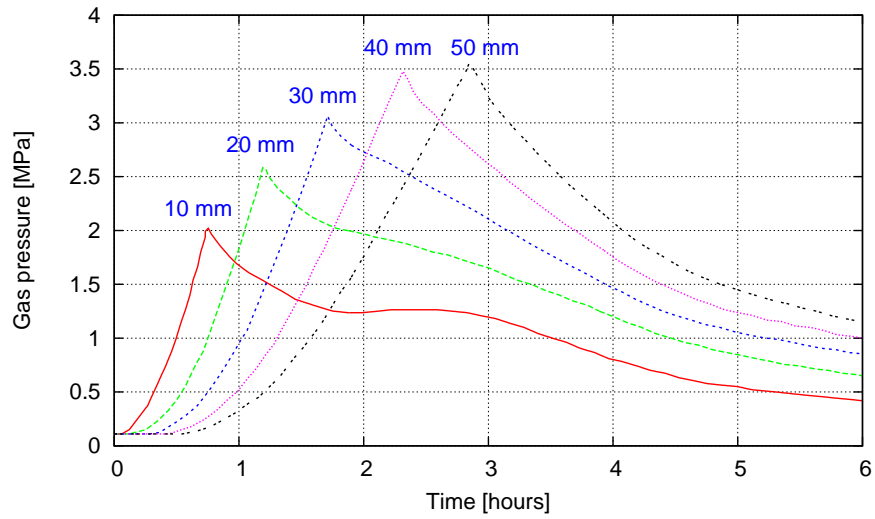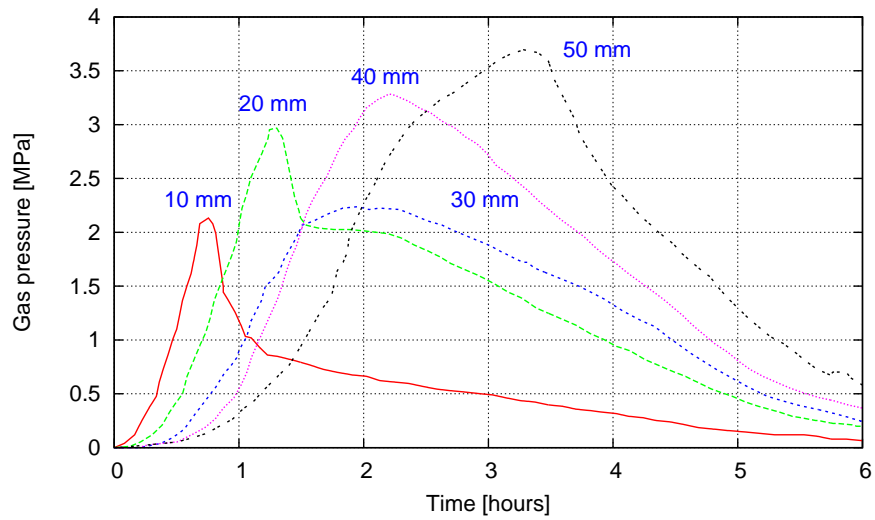
(a) simulation

(b) experiment

Figure 4.16.: Gas pressure profiles for HSC (M100) at 873K
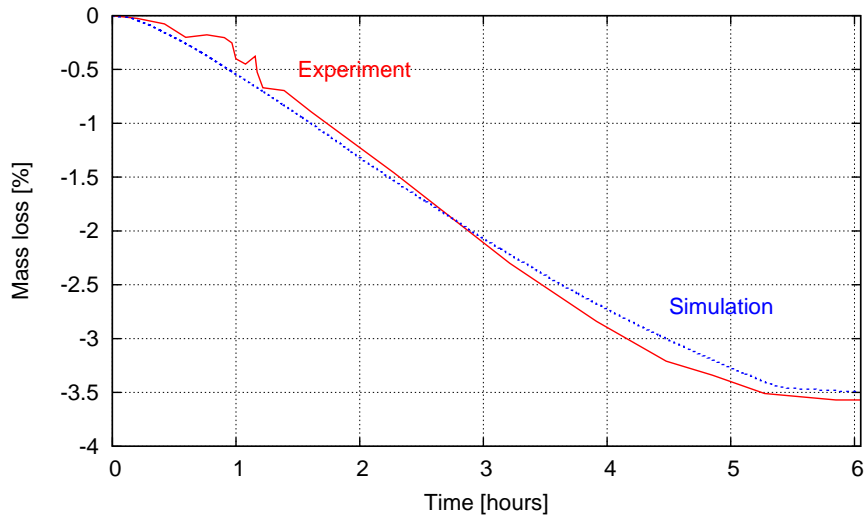
Figure 4.17.: Mass loss – comparison between experiment and numerical

the mass loss obtained from both the simulation and the experiment is presented. The mass escapes through the boundaries until a certain time and then it starts to stabilise, when a low overall level of moisture in the specimen is reached. This problem is revisited in Chapter 5, where more comprehensive results are presented for additional analyses.

4.3.1. Discussion

The presented thermo-hygral model for concrete has been qualitatively validated against Kalifa's experimental results. It has been shown that this model gives very reasonable predictions of the peak values of the gas pressure, an important component in the prediction of spalling, which will be discussed in more details in Section 7.1. The values of gas pressure are approaching the tensile strength and the possibility of spalling for this type of concrete is high.

4.4. Conclusions

In summary, it has been shown that the presented model provides the necessary mechanisms to predict the heat and moisture transport in concrete for both heating and drying problems and compare well with the existing data, experimental and numerical.

4. Model validation

The Enhanced Glasgow model is able to predict the presented drying problem accurately. The role of the state equations and material parameters are highlighted. Moreover, the calculated moisture profiles presented for both concrete types agree very well with the profiles obtained experimentally. In addition, the results are successful in interpreting a very different behaviour between normal and high strength concrete, what was expected.

Additionally, the numerical prediction of the column subjected to fire gives comparable results with respect to the Tenchev model. It was shown that the Enhanced Glasgow model improves the physical reasoning behind the proposed formulation.

Validation against Kalifa's experimental results showed that the Enhanced Glasgow model is able to reproduce the experiments at high temperature with good agreement. The pore pressure build-up and moisture concentration zone was predicted correctly.

It is argued that this validation procedure supports the conclusion that the model suits its purpose.

5. Model extension to capture effect of polypropylene fibres

One of the primary aims when constructing a model for concrete subjected to thermal loading is to be able to predict the mechanical behaviour, risks of structural damage, and especially to account for potential spalling when exposed to severe conditions. Subsequently, based on such predictions it should be possible to propose an alternative mix design and/or element design. Simultaneously, technological solutions are being developed to provide passive or active protection of the structures against spalling effects. The use of the polypropylene fibres (PPF) in the concrete mix is regarded as one of the most efficient strategies in reducing the probability of explosive spalling. Polypropylene microfibres have been employed in concrete structures during the past decade, particularly in tunnels following recent tunnel fires, which were discussed in Chapter 1. Following Khoury and Willoughby [41], it can be cited that *Polypropylene fibres are employed in concrete to combat explosive spalling in fire, but the molecular structure and the materials properties are not well understood.*

However, the recent experimental studies by Zeiml et al. [72] and the theoretical work by Khoury [36, 41] presented necessary material properties in relation to those of concrete at elevated temperatures. The work presented in this thesis is to some extent based on their conclusions.

Figure 5.1.: Types of polypropylene fibres (PPF).

5.1. Introduction

The addition of natural fibres to the concrete mix dates back to almost ancient time. It was mainly introduced to add ductility to brittle materials. Nowadays, there is an extensive use in the construction industry of small quantities of short fibres to alter the properties of the concrete, mostly to reduce cracking as it may occur. There are hundreds of different types of fibres, that can be used for concrete to solve different problems. As an example, the addition of steel fibres can be used to reduce drying shrinkage and increase tensile strength of the structural elements, on top of the regular steel reinforcement. Other type are polypropylene fibres (see Figure 5.1). With addition of this type of fibres, it seems possible to control plastic and drying shrinkage cracking. They also improve the resistance against thermal damage for both fire and freezing cases.

Polypropylene (PP) is a linear hydrocarbon polymer, expressed as $(C_3H_6)_x$. It is one of those most versatile polymers available with applications, both as a plastic and as a fibre with similar properties for both states. However, in some cases the properties of the fibre differ from those of the polymer itself. As fibres, they possess very good tensile strength in the direction of

the fibres. Polypropylene does not present stress-cracking problems and offers excellent electrical and chemical resistance at higher temperatures. The important thermal properties of the polypropylene are the melting point, which following [41] is between 150°C and 176°C, and the vaporisation point, which starts around 325°C. The recent important contribution by Khoury and Willoughby [41], gives a good insight into the property and behaviour of concrete with polypropylene fibres (PPF). Following this reference, it can be confirmed that the usual content of PPF in concrete, which can reduce the probability of explosive spalling in fire, ranges from 1 to 3 kg per m³ of concrete. Below this level, the introduction of PPF to the mix seems ineffective, whereas above it the workability of concrete begins to become a problem. Section 6.2 from Eurocode 2 [1] discusses spalling prevention, where method D presents PPF as one of the solutions. It suggests to include in the concrete mix more than 2 kg/m³ of monofilament propylene fibres.

PPF in the range of 1-3 kg/m³ of concrete, corresponds to a proportion by volume of 0.11-0.33%. Therefore, although the influence of PPF on porosity could have a local effect, it is negligible at the larger scale.

5.2. Effect of PPF on intrinsic permeability

In the context of fire damage of concrete, explosive spalling remains one of the least understood phenomena. It mainly takes place during the initial stage of the fire, and reduces the load bearing capacity of the structure. Specifically, it localises close to the heated surface and appears to peak with temperature of about 200°C to 250°C. These contribute to the considerable debate around its cause, pore pressures and thermal stresses or a combination of the two being the likely causes. This thesis has already clearly demonstrated that the excess pore pressures can be modelled accurately and are a likely candidate for the initiation of explosive spalling.

Zeiml et al. [72] observed that the spalling effects decrease with an increasing amount of PPF in the concrete mix. Extensive explanations are presented by Khoury [41, 36], suggesting that PPF play a role in reducing pore pressure via number of possible mechanisms which are summarised here.

First, one of the mechanisms that appears even before 100°C, is reported

to be the pressure-induced tangential space (*PITS*) creation. It is caused by pressure, which ruptures the weak connections between fibres and concrete, where water steam and air can migrate. This phenomenon can last till the melting temperature of the PP fibres of 150°C to 176°C. At this stage, there are already a numerous capillary ($\sim \mu m$) connections due to *PITS*, which might influence the pressure levels. Although, the melted fibres have very high viscosity, which reduces the possibility of migration, it might be assumed that previously created capillaries with existing pore spaces might build longer connections. At temperature ranging from 325°C to 475°C the melted fibres begin to vaporise into vapour that would easily travel through the concrete pores. Above 475°C all the fibres would have vaporised, leaving larger channels (according to [36] of 20-30 μm wide) for the transport of all the vapours and gases. The hydrocarbon vapour, which is produced during the vaporisation of PPF, might be combusted in the presence of oxygen at temperatures from 550°C, but this is more likely to happen outside of the concrete.

Spalling occurs at relatively low temperatures, between 150°C to 250°C, when PPF are melting. However, Khoury advocates that the creation of the new connections within the pore structure due to *PITS,* allows the initially isolated pores to interconnect and allow percolation through the concrete. As a results, there is a noticeable increase in permeability, as shown by Zeiml et al. [72], resulting in a reduction in the pore pressure [32], when compared to concrete without PPF.

Based on all of these observations, it may be concluded that permeability of concrete is one of the key controlling factors influencing spalling. Zeiml et al. [72] presented experimental evidence of the effect of PPF on the intrinsic permeability, presented in Figure 5.2.

It can be seen from Figure 5.2, that (on a logarithmic scale) the intrinsic permeability could be represented as a linear function of temperature. With the addition of the PPF there is a local increase in permeability; in the case of concrete with 1.5 kg/m^3 PPF the value of permeability, in the temperature range between 140°C to 220°C, increases almost one order of magnitude.
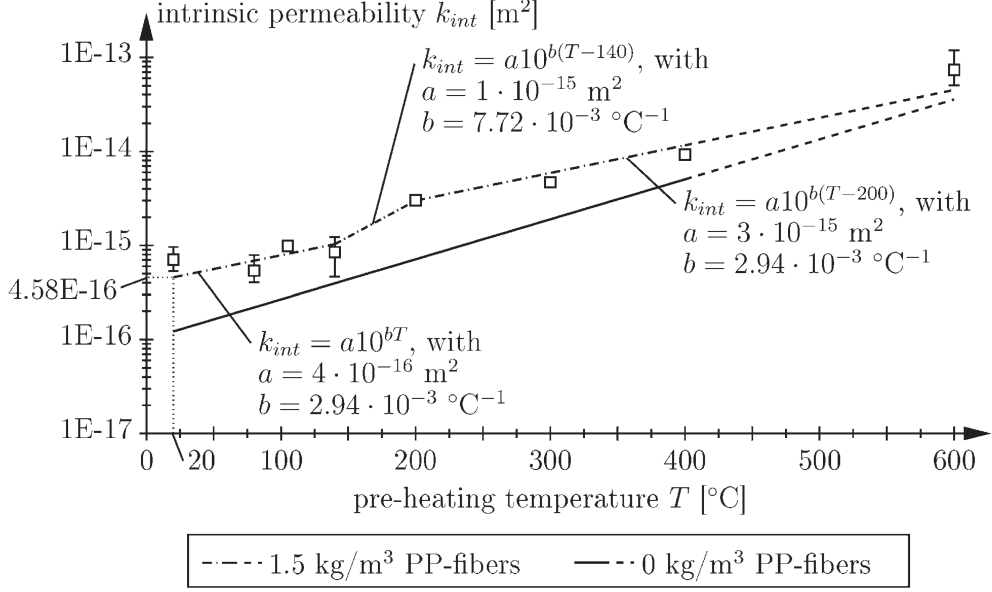
Figure 5.2.: Experimentally obtained intrinsic permeability for concrete with and without PPF from Zeiml et al. [72]

5.3. Numerical modelling

The model presented in this thesis is here extended to account for the effect of PPF on the response of moisture transport in heated concrete. The extension of the model focuses on the modification function for permeability (5.6) in the mentioned temperature region. There is a need to introduce parameters for the modified permeability function, thus

$$PPF_1 = \alpha \left(1 + 1.75 m_f\right) \tag{5.1}$$

$$PPF_2 = \alpha - m_f \tag{5.2}$$

$$\zeta_1 = \alpha + m_f \tag{5.3}$$

$$\zeta_2 = \frac{10^{PPF_1 D}}{10^{PPF_2 D}} \tag{5.4}$$

$$\zeta_3 = \frac{10^{PPF_2 D}}{10^{PPF_1 D}} \tag{5.5}$$

93
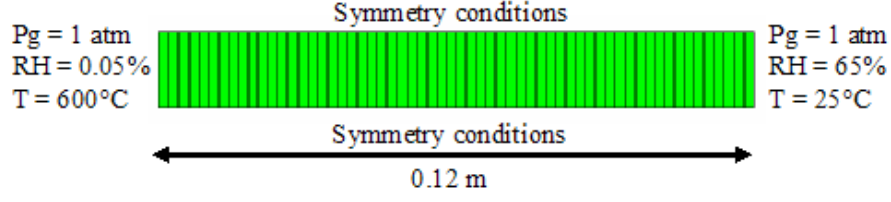
Figure 5.3.: Finite element mesh showing dimensions and boundary conditions. Reproduced after Figure 4.14.

$$K_{pp} = \begin{cases} \zeta_1 K_0 10^{PPF_2 D(T)} & T < 403K \\ \zeta_2 K_0 10^{PPF_1 D(T)} & 403K \leq T \leq 473K \\ \zeta_3 K_0 10^{PPF_2 D(T)} & T > 473K \end{cases} \qquad (5.6)$$

where K_0 - initial intrinsic permeability, ζ_i, PPF_i- coefficients taking account of PPF, m_f - mass of the fibres.

In section 4.3, the analyses of the heating problem was presented based on the experimental setup of Kalifa et al. [33]. In the next section, the continuation of Kalifa's experiments on the influence of polypropylene fibres is presented, based on [32]. Therefore, the model with the polypropylene fibres enhancement is used to simulate the experiment and the results are compared against the actual data. Finally, the presented results are concluded and possible use of the Enhanced Glasgow model towards protection of concrete structures against spalling is discussed.

5.4. Validation of influence of polypropylene fibres

The validation of the influence of polypropylene fibres is performed using data from the second Kalifa et al. [32] experiment. The experiment used the same setup as the first set of experiments [33] and the same measurements were taken. The concrete samples with the addition of PPF were subjected to thermal loading on the upper face and the four lateral faces were thermally insulated (see Figure 4.13). The maximum temperature was 600°C (873.15K) and the heating duration time was 6 hours. All properties, mesh, boundary conditions and initial conditions remain the same.
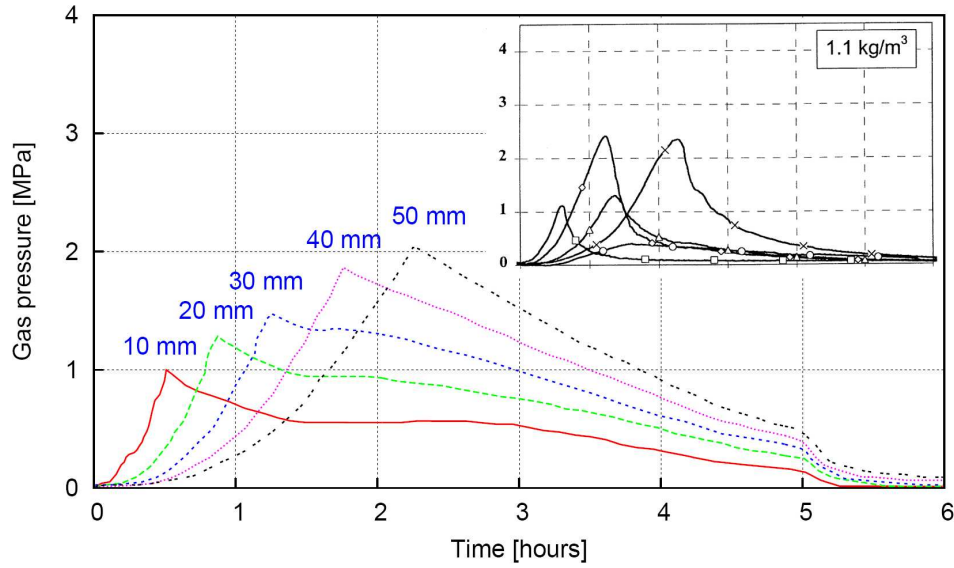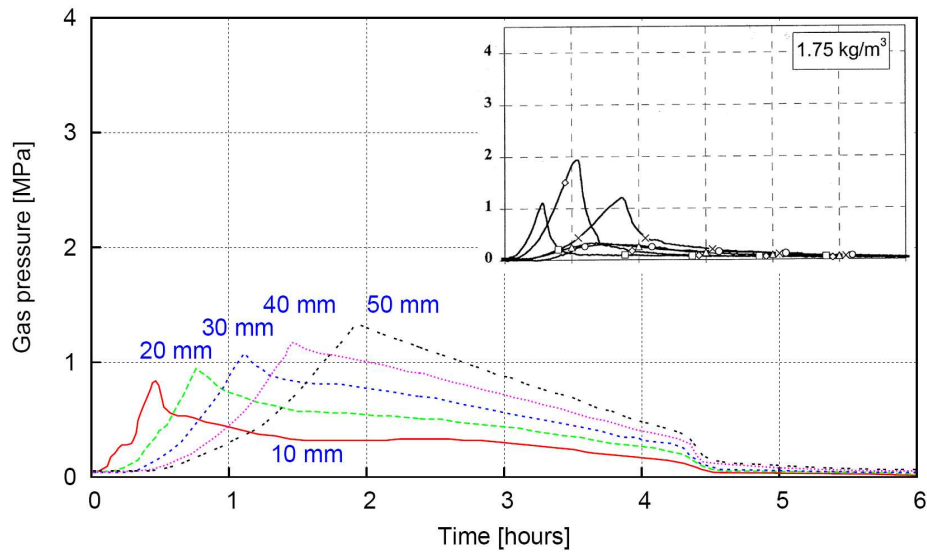
Figure 5.4.: Results for 1.1 kg/m³ of PPF in the concrete mix: simulation (main) and experiment (top right corner)

Here, comparison of the numerical results with experiments is restricted to gas pressures, since all other results are sufficiently similar to the results presented for the original study.

5.4.1. Results

Figure 5.4 and 5.5 show numerically and experimentally obtained gas pressures for 1.1 and 1.75 kg/m³. Comparison of these experimental results with the results for no PPF, shown in Figure 4.16b clearly indicate the reduction in peak gas pressures as a result of PPF. The values with 1.1 and 1.75 kg/m³ of PPF were respectively two and three times less than for concrete without PPF. The numerical results also show good qualitative and quantitative agreement with the experimental results. The experimental peak value for the concrete mix with 1.1 kg/m³ PPF was around 2.1 MPa and for the simulation it was 2 MPa. The peak pressure values for 1.75 kg/m³ mix for both simulation and experiment were about 1.4 MPa. The inconsistency in the trend of the curves for different depths have not been fully explained in the original paper [33] but this may be due to the melting process of the fibres in the region close to the pressure transducers.

Figure 5.5.: Results for 1.75 kg/m^3 of PPF in the concrete mix: simulation (main) and experiment (top right corner)

In addition, the continuous rise of the gas pressures with distance from the heated face in the numerical simulations needs further consideration. In contrast, in the experimental curves it can be seen that the gas pressures start to stabilise. These results indicate that one of the principal methods of preventing spalling is captured by the presented model.

5.5. Conclusions

To summarise, the inclusion of polypropylene fibres have been experimentally proved to be an effective means of passive fire protection by mitigating the possibility of explosive spalling and offering a positive solutions to maintaining structural integrity in fire, especially compared to alternative solutions such as the inclusion of sacrificial zones.

The Enhanced Glasgow model has been extended to include the effects of PPF in a straightforward manner that has shown to quite satisfactory extent when compared to independent experimental results. The presented extension, although simple, takes into account changes in permeability due to the addition of PPF.

Following Khoury [36], the effectiveness of the pressure release mecha-

nisms provided by PPF depends not only on the characteristics of PPF properties, but also on the dimensions, orientation and amount of the fibres itself. Future research could be directed into multi-scale modelling using, for example, semi-analytical approach, like self-consistent scheme, which will be discussed in Chapter 8.

6. Hygro-Thermo-Mechanical model of concrete

The previous chapters have described a heat and mass transport model for concrete and its validation. So far, no mechanical influence has been considered.

The ultimate aim of this thesis is to present a full thermo-hygro-mechanical model of concrete that can be used to predict its behaviour when subject to thermal and mechanical loading. Therefore, in this chapter the mechanical aspects concerning the behaviour of concrete subjected to high temperatures will be discussed. The details of the mechanical part of the model will be presented and the main focus will be put on decomposition of the total strain rate, as well as the coupling of the mechanical and transport models.

The structure of this chapter is as follows. First, the details of strain rate decomposition are shown. Second, a detailed description of each of the strain components is presented. This is followed by the thermal and mechanical damage, based on continuum damage mechanics framework. Next, a hygro-mechanical coupling is introduced, using the effective stress concept. The chapter is concluded with a summary and the final form of the mechanical part of the formulation.

6.1. Mechanical behaviour

The total strain rate can be decomposed as follows:

$$\dot{\varepsilon} = \dot{\varepsilon}^e\left(\sigma, T\right) + \dot{\varepsilon}^{pl}\left(\sigma, T\right) + \dot{\varepsilon}^{ft}\left(T\right) + \dot{\varepsilon}^c\left(\sigma, T\right) + \dot{\varepsilon}^{tm}\left(\sigma, T\right) \qquad (6.1)$$

where $\dot{\varepsilon}^e$ is the elastic strain rate, $\dot{\varepsilon}^{pl}$ is the plastic strain rate, $\dot{\varepsilon}^{ft}$ is the free thermal strain rate, $\dot{\varepsilon}^c$ is the creep strain rate and $\dot{\varepsilon}^{tm}$ is the thermo-mechanical strain rate.

The last two terms of this equation, the creep strain rate and the thermo-mechanical strain rate, can be combined to form the load induced thermal strain. The thermo-mechanical strain component is recognised to appear only during the first heating and not during subsequent cooling or heating cycles, thus it is an irrecoverable strain component and it is important factor in the behaviour of concrete structures during high temperature loading, as it may lead to severe tensile stresses during cooling process.

All the strain components will be briefly presented and discussed in the subsequent sections of this chapter. For simplicity, the presented work does not involve plasticity, but inelastic mechanical response is captured by a continuum damage mechanics.

6.2. Free thermal strains

The free thermal strain of concrete is mainly influenced by the type and amount of aggregates. Furthermore, its behaviour is non-linear and depends on the thermal stability of the aggregate itself. It is evident that $\dot{\varepsilon}^{ft}$ is a function of temperature although it is recognised to depend on the rate of heating as well. The thermal strain rate is:

$$\dot{\varepsilon}_{ij}^{ft} = \alpha_{ft}\dot{T}\delta_{ij} \qquad (6.2)$$

where α_{ft} is the coefficient of free thermal strain.

Usually the coefficient of free thermal strain for certain material is assumed a constant value within a normal temperature range between -20°C to 50°C. As suggested by Nielsen et al. [54], the temperature dependent coefficient α_{ft} for normal quartzite concrete can be expressed as:

$$\alpha_{ft} = \begin{cases} \frac{6 \times 10^{-5}}{7 - \bar{T}} & \text{for } 0 \leq \bar{T} \leq 6 \\ 0 & \text{for } \bar{T} > 6 \end{cases} \tag{6.3}$$

where $\bar{T} = \frac{(T - 293.15)}{100}$ and it is a normalised temperature.

The presented function was established to present a suitable trend rather than fitting specific experimental values. Experimental evidence indicates that thermal strains stop increasing once the temperature exceeds 600°C, which can be associated, following Bazant and Kaplan [7], with quartzite aggregate behaviour. There is a significant increase in thermal strains between 500°C and 600°C, due to the conversion of quartz crystals.

Using Voigt notations (matrix-vector), thermal strains can be expressed as:

$$\dot{\boldsymbol{\varepsilon}}^{ft} = \boldsymbol{m}\dot{T} \tag{6.4}$$

where $\boldsymbol{m} = \alpha \begin{pmatrix} 1 & 1 & 1 & 0 & 0 & 0 \end{pmatrix}^T$.

6.3. Load induced thermal strains

The load induced thermal strain (*lits*), corresponding to the last two terms of (6.1), is determined experimentally by measuring total strain during first time heating on the concrete specimen under sustained loading. The free thermal strain, measured on a unstressed specimen, and the initial elastic strain are subtracted from the total strain to give the load induced thermal strain as a function of temperature. Schneider [61] reported several test series, which were conducted through 1970's, on the load induced thermal strain of concrete tested under sustained uni-axial compressive load and constant heating rate. Another extensive experimental research took place at Imperial College London, during 1980's [38, 37], where Khoury et al. suggested that so called '*lits* master curve' exists, largely independent of aggregate type, concrete strength, age and initial moisture content.

In the rheological model proposed by Thelandersson [66] the uni-axial load induced thermal strain rate included a dashpot and thermo-mechanical element corresponding to the temperature dependent creep ($\dot{\boldsymbol{\varepsilon}}^c$) and thermo-mechanical strain ($\dot{\boldsymbol{\varepsilon}}^{tm}$) respectively. It has been recognised that these two

components cannot be separated in an experiment and thus the subdivision into two components is mainly theoretical and has little practical implications for short duration heating, as stated by Schneider [61]. However, Thelandersson [66] suggested that the creep strain is minor compared with thermo-mechanical one for practical test conditions even though steady-state creep is found to be enhanced by high temperatures. Nielsen et al.[55] illustrated, that even for a very slow heating rate of 0.05 K/min the creep strain corresponds to only up to 20 % of the thermo-mechanical strain and this value drops significantly for increased heating rates. Therefore, it seems reasonable to assume that the creep component of *lits* can be neglected.

The general formulation of the thermo-mechanical strain rate provided by Thelandersson [66] can be seen in Equation (6.5). For the uni-axial case, he assumed proportionality between $\left(\dot{\varepsilon}^{ft}\right)$ and $\left(\dot{\varepsilon}^{tm}\right)$.

$$\dot{\varepsilon}_{ij}^{tm} = \left(\gamma_1 \sigma_{kk} \delta_{ij} + \gamma_2 \sigma_{ij}\right)\dot{T} \qquad (6.5)$$

where the two coefficients γ_1 and γ_2 need to be determined experimentally. However, similarly to de Borst and Peeters [16], they can be substituted by clear physically based assumptions shown in Equation (6.6).

$$\gamma_1 = -v_c \frac{\beta}{f_c^0}, \ \gamma_2 = \left(1 + v_c\right)\frac{\beta}{f_c^0} \qquad (6.6)$$

where v_c is the transient creep Poisson's ratio, f_c^0 is the uni-axial compressive strength at room temperature and β is the coefficient of uni-axial thermo-mechanical strain.

By inserting (6.6) into (6.5) a proper thermo-mechanical strain rate formulation is obtained, which can be seen in Equation (6.7). It is noted that the formulation does not include stress variation dependency. This reflects the fact that, under a constant temperature, a variation of stress would not result in a change in the thermo-mechanical strain.

$$\dot{\varepsilon}_{ij}^{tm} = \frac{\beta}{f_c^0}\left(-v_c \sigma_{kk}\delta_{ij} + \left(1 + v_c\right)\sigma_{ij}\right)\dot{T} \qquad (6.7)$$

Subsequently, it is possible to describe the uni-axial thermo-mechanical strain with a bi-parabolic expression (6.8) presented in Nielsen et al. [55]. This bi-parabolic approach keeps the formulation simple, which is achieved
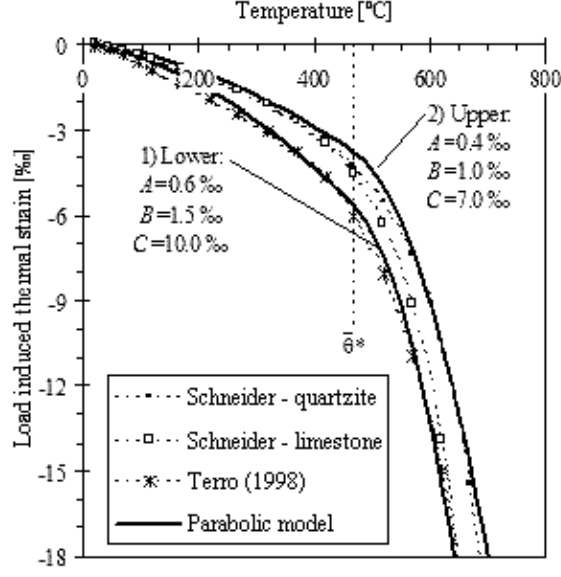
Figure 6.1.: Load induced thermal strain - comparison of experimental data with a parabolic model from [55]

by applying a direct proportionality with the stress level.

$$\varepsilon^{tm} = \frac{\sigma}{f_c^0} y \qquad (6.8)$$

where

$$y = \begin{cases} A\bar{T}^2 + B\bar{T} & for\ 0 \leq \bar{T} \leq \bar{T}^* \\ C\left(\bar{T} - \bar{T}^*\right)^2 + A\left(2\bar{T} - \bar{T}^*\right) + B\bar{T} & for\ \bar{T} > \bar{T}^* \end{cases} \qquad (6.9)$$

where $\bar{T}^*$ is a dimensionless transition temperature between the two expressions of 470°C.

When looking at figure 6.1 it can be seen that the parabolic model captures the experimental behaviour in a satisfactory manner. The two limiting parabolic curves in figure 6.1, provided by two sets of parameters (A,B,C), define a range where the thermo-mechanical strain is likely to be found for normal concretes with various aggregate types.

From the above, it is possible to determine the coefficient of uni-axial thermo-mechanical strain rate as shown in Equation (6.10).

6. Hygro-Thermo-Mechanical model of concrete

$$\dot{\varepsilon}^{tm} = \frac{\sigma}{f_c^0} \frac{dy}{d\bar{T}} \frac{d\bar{T}}{dT} \dot{T} = \frac{\sigma}{f_c^0} \beta \dot{T} \tag{6.10}$$

where the coefficient of thermal mechanical strain is

$$\beta = 0.01 \times \begin{cases} 2A\bar{T} + B & for \ 0 \le \bar{T} \le \bar{T}^* \\ 2C\left(\bar{T} - \bar{T}^*\right) + 2A\bar{T}^* + B & for \ \bar{T} > \bar{T}^* \end{cases} \tag{6.11}$$

All experimental tests for load induced thermal strains are performed on concrete specimens under sustained compressive loading and then subject to transient heating. The author is currently unaware of any similar tests performed under sustained tensile loading and therefore it is difficult to assess whether the proposed formulation for compressive stress conditions could be used for tensile stress conditions as well. Thus (6.7) is rewritten as (6.12).

$$\begin{aligned} \dot{\varepsilon}_{ij}^{tm} = \ & \frac{\beta^-}{f_c^0} \left(-v_c \sigma_{kk}^- \delta_{ij} + (1 + v_c)\, \sigma_{ij}^-\right) \dot{T} \ + \\ & \frac{\beta^+}{f_c^0} \left(-v_c \sigma_{kk}^+ \delta_{ij} + (1 + v_c)\, \sigma_{ij}^+\right) \dot{T} \quad for \ \dot{T} > 0 \end{aligned} \tag{6.12}$$

where β^- and β^+ are the coefficients of compressive and tensile uni-axial thermo-mechanical strain respectively. σ^- and σ^+ are the negative and positive projections of the stress tensor. For convenience, β^+ is set to zero until more experimental evidence on the load induced thermal strain due to tensile loading is made available. Therefore (6.12) becomes

$$\dot{\varepsilon}_{ij}^{tm} = \frac{\beta^-}{f_c^0} \left(-v_c \sigma_{kk}^- \delta_{ij} + (1 + v_c)\, \sigma_{ij}^-\right) \dot{T} \ for \ \dot{T} > 0 \tag{6.13}$$

which illustrates that v_c is analogous to Poisson's ratio. To the author's knowledge the bulk of experiments on the load induced thermal strain do not include lateral deformation measurements. However, some experiments showed that load induced thermal strains have a lateral component similar to that observed in conventional creep tests.

Using Voigt's notations, load induced thermal strain rates can be expressed as:

$$\dot{\varepsilon}^{tm} = \boldsymbol{M}^{-}\boldsymbol{\sigma}^{-}\dot{T} \qquad (6.14)$$

where $\boldsymbol{M}^{-}$ is similar to that defined by de Borst and Peeters [16], as shown in Equation (6.15).

$$\boldsymbol{M}^{-} = \frac{\beta^{-}}{f_c^0} \begin{bmatrix} 1 & -v_c & -v_c & 0 & 0 & 0 \\ -v_c & 1 & -v_c & 0 & 0 & 0 \\ -v_c & -v_c & 1 & 0 & 0 & 0 \\ 0 & 0 & 0 & 2\left(1+v_c\right) & 0 & 0 \\ 0 & 0 & 0 & 0 & 2\left(1+v_c\right) & 0 \\ 0 & 0 & 0 & 0 & 0 & 2\left(1+v_c\right) \end{bmatrix} \qquad (6.15)$$

6.4. Thermal and Mechanical damage

Degradation of the elastic stiffness can also be caused by exposure to elevated temperatures as well as by mechanical loading. Those types of failure are characterised by the non-linear behaviour of the material. The work presented in this thesis is within the continuum mechanics framework. Therefore, the continuum damage mechanics is used to model the non-linear behaviour of concrete as a quasi-brittle material.

The phenomenological damage mechanics model, presented in this thesis, is based on the fracture energy obtained from experimental observation. This theory presents damage in the smooth sense and ignores the stress localisation at the crack tip. For simplicity, only isotropic damage model is considered.

In addition to the mechanical aspects, the thermal damage is considered using similar approach. However, thermally induced damage is largely the result of the changing physical properties of the cement paste when concrete is heated.

Thus, the approach with two damage parameters is used, characterising the necessary aspects of damage, thermal and mechanical.

6.4.1. Damage mechanics

The classical elasticity-based isotropic damage model, within the continuum mechanics framework, with a single scalar damage parameter is presented in Equation (6.16). This equation describes the influence of the damage on the response of the material, which results in degradation of its elastic stiffness.

$$\boldsymbol{\sigma} = (1 - \omega)\, \boldsymbol{E}_0 : \boldsymbol{\varepsilon}^e = \boldsymbol{E}_{sec} : \boldsymbol{\varepsilon}^e \tag{6.16}$$

where E_0 is a 4th order tensor of elastic moduli of the virgin material, $\boldsymbol{\varepsilon}^e$ is the elastic tensor and ω is the damage parameter growing from 0 for the intact material to 1 for a complete material degradation and $\boldsymbol{E}_{sec}$ is a secant stiffness.

In general formulation for damage mechanics, the damage parameter can be chosen as a scalar, several scalars or different order tensors. The presented model involves only a single parameter for damage, however it is inappropriate to use it for both, thermal and mechanical damage at the same time. In order to extend this approach to capture both these effects, a multiplicative decomposition of the total damage is assumed as:

$$\boldsymbol{\sigma} = (1 - D)\, \boldsymbol{E}_0 : \boldsymbol{\varepsilon}^e = (1 - \omega)(1 - \chi)\, \boldsymbol{E}_0 : \boldsymbol{\varepsilon}^e \tag{6.17}$$

where D is the total damage parameter and χ is the thermal damage parameter, as presented in section 3.4.2.

The effective stress in the undamaged material is:

$$\hat{\boldsymbol{\sigma}} = \boldsymbol{E}_0 : \boldsymbol{\varepsilon}^e = \frac{\boldsymbol{\sigma}}{(1 - \omega)(1 - \chi)} \tag{6.18}$$

In this thesis, it is assumed that the strain associated with the damaged state, $\boldsymbol{\varepsilon}$, is the same as the strain associated with the equivalent undamaged state, $\hat{\boldsymbol{\varepsilon}}$, subjected to the effective stress as: $\boldsymbol{\varepsilon} = \hat{\boldsymbol{\varepsilon}}$.

Both damage parameters are controlled by damage loading functions. The thermal damage loading function is

$$f^{td} = T - \kappa^{td} \tag{6.19}$$

where κ^{td} is a history variable that represents the maximum temperature T, to which the material point has been subjected in its loading history.

The mechanical damage loading function with a single scalar history parameter is

$$f^{md} = \tilde{\varepsilon} - \kappa^{md} \tag{6.20}$$

where the $\tilde{\varepsilon}$ is the equivalent strain measure, which is a function of a components of the strain tensor and reflects the influence of each of these components on the micro-structural degradation of the material. This evolution law is again coupled to the loading history through a scalar parameter κ^{md}, which represents the most severe equivalent strain state to which the material point has been subjected in its loading history.

The damage loading functions depend on the form of the equivalent strain($\tilde{\varepsilon}$) or temperature (T), while the extent of the surface is set by the history parameters $\left(\kappa^{md} \text{ or } \kappa^{td}\right)$. The initial loading function follows from the initial value of the history parameters.

In either case, if $f > 0$ then the history parameter $\left(\kappa^{md} \text{ or } \kappa^{td}\right)$ will increase until $f = 0$. The evolution of the loading function is fully described by the standard Kuhn-Tucker loading-unloading conditions. Their general form is presented in Equation (6.21), whereas the specific forms for thermal and mechanical damages are presented in Equations (6.22) and (6.23), respectively.

$$f \leq 0, \ \dot{\kappa} \geq 0, \ \dot{\kappa} \cdot f = 0 \tag{6.21}$$

$$
\begin{aligned}
\dot{\chi} &= 0 \begin{cases} \text{if} & f^{td} \leq 0 \\ \text{or if} & f^{td} = 0 \ \& \dot{f}^{td} \leq 0 \end{cases} \\
\dot{\chi} &\geq 0 \text{ if } f^{td} = 0 \ \& \dot{f}^{td} = 0
\end{aligned}
\tag{6.22}
$$

$$\dot{\omega} \;=\; 0 \;\begin{cases} \text{if} & f^{md} \le 0 \\ \text{or if} & f^{md} = 0 \ \& \dot{f}^{md} \le 0 \end{cases} \tag{6.23}$$

$$\dot{\omega} \;\ge\; 0 \quad \text{if} \ \ f^{md} = 0 \ \& \dot{f}^{md} = 0$$

Given that $\varepsilon^e = \varepsilon - \varepsilon^{ft} - \varepsilon^{tm}$, the stress rate follows from (6.17) and (6.18) as

$$\begin{aligned} \dot{\boldsymbol{\sigma}} \;&=\; (1-\omega)\,(1-\chi)\,\boldsymbol{E}_0 : (\dot{\boldsymbol{\varepsilon}}^e) - \\ &-\; \dot{\chi}\,(1-\omega)\,\boldsymbol{E}_0 : \dot{\varepsilon}^e - \dot{\omega}\,(1-\chi)\,\boldsymbol{E}_0 : \dot{\varepsilon}^e = \\ &=\; \boldsymbol{E}_{sec} : \left(\dot{\boldsymbol{\varepsilon}}^e - \dot{\boldsymbol{\varepsilon}}^{ft} - \dot{\boldsymbol{\varepsilon}}^{tm}\right) - \dot{\chi}\,(1-\omega)\,\hat{\boldsymbol{\sigma}} - \dot{\omega}\,(1-\chi)\,\hat{\boldsymbol{\sigma}} \end{aligned} \tag{6.24}$$

Substitution of (6.4) and (6.14) into the above results in

$$\dot{\boldsymbol{\sigma}} = \boldsymbol{E}_{sec} : \left(\dot{\boldsymbol{\varepsilon}}^e - \boldsymbol{m}\dot{T} - \boldsymbol{M}^-\boldsymbol{\sigma}^-\dot{T}\right) - \dot{\chi}\,(1-\omega)\,\hat{\boldsymbol{\sigma}} - \dot{\omega}\,(1-\chi)\,\hat{\boldsymbol{\sigma}} \tag{6.25}$$

Alternatively, the discrete incremental form is

$$d\boldsymbol{\sigma} = \boldsymbol{E}_{sec} : \left(d\varepsilon^e - \boldsymbol{m}dT - \boldsymbol{M}^-\boldsymbol{\sigma}^-dT\right) - d\chi\,(1-\omega)\,\hat{\boldsymbol{\sigma}} - d\omega\,(1-\chi)\,\hat{\boldsymbol{\sigma}} \tag{6.26}$$

The description of the evolution of damage is completed by the proper description of the applied damage evolution law, which defines the relation between the damage parameter and the history variable.

First, the thermal part is discussed. A simple definition of the temperature dependency for elastic modulus E is expressed in Equation (6.27)[55]. Thus, as a result of increased temperature, there is an assumed degradation of the elastic modulus and the following damage function can be established:

$$\frac{E}{E_0} = \left(1 - 0.1\hat{\mathrm{T}}\right) \ \text{for } 0 \le \hat{\mathrm{T}} \le 10 \tag{6.27}$$

where $\hat{\mathrm{T}} = max\left(\bar{\mathrm{T}}\right)$ is the maximum normalised temperature reached.

6. Hygro-Thermo-Mechanical model of concrete

$$\chi\left(T\right) = 20\left(\kappa^{td} - \kappa_0^{td}\right)\left(1 - 5\left(\kappa^{td} - \kappa_0^{td}\right)\right) \tag{6.28}$$

Consequently, the incremental form of thermal damage evolution law, when $T = \kappa^{td}$, can be computed as:

$$d\chi = \frac{\partial\chi}{\partial\kappa^{td}}dT = H^{td}dT \tag{6.29}$$

Similarly, within the mechanical framework, there is a need to specify the damage loading function. There are several different definitions, which are for example listed in [28] as energy release rate or its normalised version and Mazar's equivalent strain. An alternative, which has been successfully used in the context of concrete, is the modified von Mises equivalent strain [58]:

$$\tilde{\varepsilon} = AJ_1 + \sqrt{A^2 J_1^2 + B J_2} \tag{6.30}$$

$$J_1 = tr\left(\boldsymbol{\varepsilon}\right) = \varepsilon_1 + \varepsilon_2 + \varepsilon_3 \tag{6.31}$$

$$J_2 = tr\left(\boldsymbol{\varepsilon}\cdot\boldsymbol{\varepsilon}\right) - \frac{1}{3}tr^2\left(\boldsymbol{\varepsilon}\right) = \frac{1}{3}\left(\left(\varepsilon_1 - \varepsilon_2\right)^2 + \left(\varepsilon_2 - \varepsilon_3\right)^2 + \left(\varepsilon_1 - \varepsilon_3\right)^2\right) \tag{6.32}$$

where the coefficients A and B are as follows:

$$A = \frac{\eta - 1}{2\upsilon\left(1 - 2\upsilon\right)}; B = \frac{3}{\eta\left(1 + \upsilon\right)} \tag{6.33}$$

where the parameter η is used to quantify the different sensitivity to tensile and compressive strains and υ is the Poisson's ratio. This definition has been derived from the von Mises flow rule in plasticity, where it has been formulated in terms of stresses.

This definition of the equivalent strain leads to an identical damage evolution under the compressive stress of magnitude $\eta\sigma$ as it would be under the tensile stress σ. This is the major advantage of this definition, since an experimentally determined compression/tension strength ratio η can be entered directly in the model. Figure 6.2 presents the modified von Mises definition of an equivalent strain for the two-dimensional case for the arbi-
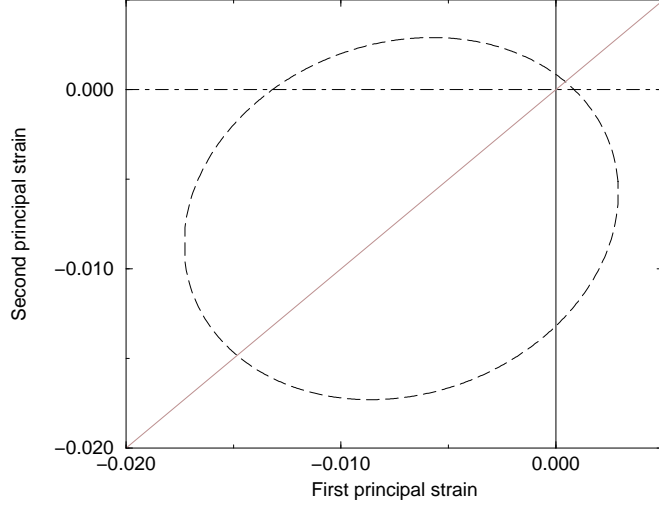
Figure 6.2.: Modified von Mises equivalent strain definition

trary value $\eta = 10$.

The mechanical damage evolution law function is defined in an integral sense following Peerlings et al. [58], as expressed in Equation (6.34). The form of this equation is based on exponential softening, which has proved to be adequate for the behaviour of a quasi-brittle materials such as concrete [44].

$$
\omega\left(\kappa^{md}\right) = 1 - \frac{\kappa_0^{md}}{\kappa^{md}}\left(1 - \alpha_\omega + \alpha_\omega e^{-\gamma\left(\kappa^{md} - \kappa_0^{md}\right)}\right) \tag{6.34}
$$

The first term $(1 - \alpha_\omega)$ represents the residual stress state as $\omega \to 1$, expressed as a proportion of the original strength. For simplicity, α is set to unity and all of the terms are set to be temperature dependent, so Equation (6.34) becomes (6.35).

$$
\omega\left(\kappa^{md}\right) = 1 - \frac{\kappa_0^{md}\left(T\right)}{\kappa^{md}}e^{-\gamma(T)\left(\kappa^{md} - \kappa_0^{md}(T)\right)} \tag{6.35}
$$

The mechanical damage threshold, $\kappa_0^{md}\left(T\right)$, is defined as a function of tensile strength $f_t\left(T\right)$ and elastic modulus $E\left(T\right)$ as follows:

$$
\kappa_0^{md}\left(T\right) = \frac{f_t\left(T\right)}{E\left(T\right)} \tag{6.36}
$$

It is assumed that the ratio between the compressive and tensile strength remains constant with changes in temperature and their temperature de-

pendency [73] can be expressed as:

$$\frac{f_t(T)}{f_t(0)} = \frac{f_c(T)}{f_c(0)} = 1 - 0.016\hat{T}^2 \text{ for } 0 \le \hat{T} \le 7.9 \qquad (6.37)$$

Therefore, $\kappa_0^{md}(T)$ can be rewritten dependent on temperature, via Equation (6.38).

$$\kappa_0^{md}(T) = \frac{f_t(0)}{E(0)} \frac{1 - 0.016\hat{T}^2}{1 - 0.1\hat{T}} \text{ for } 0 \le \hat{T} \le 7.9 \qquad (6.38)$$

The parameter in equation (6.35), $\gamma(T)$ controls the slope of the softening curve, whereby a large value corresponds to a brittle response and a small value represents a ductile one. Due to thermal effects, this term has been made temperature dependent in order to capture the change in ductility that occurs as temperature increases, according to Zhang et al. [73]. This is discussed in the next section.

6.4.2. Framework for mesh objective results

Concrete cracking is here modelled within a continuum setting, via accumulated damage. It is well known, in the context of the Finite Element Method, that the softening response adopted in Equation (6.35) results in a pathological mesh dependence (see for example [58]). The reason for this is the strain localisation into a single element, as a result of softening. If the element size changes, then so does the response. In the extreme case of the element size tending to zero, cracks can develop with no energy being dissipated. The solution to this problem is to introduce a length scale and this can be achieved in one of two ways:

1. The fracture energy approach, whereby the fracture energy G_f, is a material parameter and the softening law depends on the element size. In this way, the strains localise into the element and the softening law is modified accordingly to the size of the element.

2. A length scale parameter is introduced to define the size of the localisation zone. In this non-local approach, the strains localise into a zone that is independent of the mesh.

In the second approach, the stresses at a point must not only depend on the strains at that point but also on the strains in the vicinity of the point. Such an approach is refereed to as a non-local approach and has been successfully applied to the analysis of concrete [16, 28]. However, such an approach is outwith the scope of this work.

Instead, the fracture energy approach is adopted. The fracture energy G_f is described as the area under the stress-crack opening curve:

$$G_f = \int \sigma d\triangle u \qquad (6.39)$$

where $\triangle u$ is the crack opening.

In a continuum setting, the smeared crack approach is adopted.

Experiments carried out at Glasgow University as part of an MAECENAS EU project [73] for high strength concrete with a basalt aggregate indicate a phenomenological dependency of the fracture energy on temperature:

$$G_f(T) = G_{f0}\left(1 + 0.39\hat{T} - 0.07\hat{T}^2\right) \text{ for } 0 \leq \hat{T} \leq 4.8 \qquad (6.40)$$

where G_{f0} is the fracture energy at room temperature.

The softening parameter is expressed as

$$\gamma(T) = \frac{(1 - \chi(T))f_t(T)\lambda}{G_f(T)} \qquad (6.41)$$

where λ is the element size, taken as $\lambda = 2\sqrt{A/\pi}$ in 2D, where A is the element area.

With the definition of ω and χ at hand, $d\omega$ and $d\chi$ are expressed as:

$$d\chi = \frac{\partial \chi}{\partial \kappa^{td}}dT = H^{td}dT \qquad (6.42)$$

$$d\omega = \frac{\partial \omega}{\partial \kappa^{md}}d\tilde{\varepsilon} + \frac{\partial \omega}{\partial T}dT = H_1^{md}d\tilde{\varepsilon} + H_2^{md}dT \qquad (6.43)$$

Furthermore,

$$\begin{aligned} d\tilde{\varepsilon} &= \frac{\partial \tilde{\varepsilon}^T}{\partial \boldsymbol{\varepsilon}^e}\left(\frac{\partial \boldsymbol{\varepsilon}^e}{\partial \boldsymbol{\varepsilon}}d\boldsymbol{\varepsilon} + \frac{\partial \boldsymbol{\varepsilon}^e}{\partial T}dT\right) = \boldsymbol{s}^T\left(d\boldsymbol{\varepsilon} - \left(\frac{\partial \boldsymbol{\varepsilon}^{ft}}{\partial T} + \frac{\partial \boldsymbol{\varepsilon}^{tm}}{\partial T}\right)dT\right) \\ &= \boldsymbol{s}^T\left(d\boldsymbol{\varepsilon} - \left(\boldsymbol{m} + \boldsymbol{M}^-\boldsymbol{\sigma}^-\right)dT\right) \end{aligned} \qquad (6.44)$$

Therefore,

$$dω = H_1^{md} s^T dε - H_1^{md} s^T \left(m + M^- σ^- \right) dT + H_2^{md} dT \qquad (6.45)$$

6.5. Hygro-mechanical coupling

The influence of mechanical model on the transport model was already presented in section 3.4.2. The intrinsic permeability depends on the total damage parameter and it is repeated here for completness:

$$K = K_0 \cdot 10^{αD} \qquad (6.46)$$

To complete the full coupling between the mechanical model and the fluid transport, it is required to provide the interaction between the solid skeleton and liquid and gas phases It is introduced using the definition of Bishop's effective stress formulation [10]. The Bishop's effective stress tensor is introduced as:

$$σ' = σ + P_{Pore} I \qquad (6.47)$$

The averaged pore pressure, P_{Pore}, is determined by assuming that the adsorbed water applies no pressure but in fact behaves as a part of the solid skeleton, when considering transfer of stresses. The effects of the liquid and gas pressures are weighted on pro rata basis according to their volume fractions in the remaining pore space [15] as can be seen in Equation (6.48).

$$P_{Pore} = \begin{cases} P_G - P_{G,\infty} & \text{for } S \leq S_{SSP} \\ \bar{S} P_L + \left(1 - \bar{S} \right) P_G - P_{G,\infty} & \text{for } S > S_{SSP} \end{cases} \qquad (6.48)$$

where $P_{G,\infty}$ is the external, atmospheric pressure and $\bar{S}$ is the effective liquid saturation defined as:

$$\bar{S} = \left(\frac{S - S_{SSP}}{1 - S_{SSP}} \right) \qquad (6.49)$$

The Bishop's effective stress accounts for the mechanical deformation of the concrete. Thus, the classical isotropic damage model can be rewritten as:

$$\boldsymbol{\sigma}' = \left(1 - \omega\right)\left(1 - \chi\right)\boldsymbol{E}_0 : \boldsymbol{\varepsilon}^e = \boldsymbol{E}_{sec} : \boldsymbol{\varepsilon}^e \qquad (6.50)$$

The stresses in the undamaged material, i.e. the effective stresses, are expressed as:

$$\hat{\boldsymbol{\sigma}}' = \boldsymbol{E}_0 : \boldsymbol{\varepsilon}^e = \frac{\boldsymbol{\sigma}'}{\left(1 - \omega\right)\left(1 - \chi\right)} \qquad (6.51)$$

The total stress rate can be determined from (6.47), what results in:

$$\dot{\boldsymbol{\sigma}} = \dot{\boldsymbol{\sigma}}' + \dot{P}_{Pore}\boldsymbol{I} \qquad (6.52)$$

The Bishop's stress rate is:

$$\begin{aligned}
\dot{\boldsymbol{\sigma}}' &= \boldsymbol{E}_{sec} : \left(\dot{\boldsymbol{\varepsilon}} - \dot{\boldsymbol{\varepsilon}}^{ft} - \dot{\boldsymbol{\varepsilon}}^{tm}\right) - \dot{\chi}\left(1 - \omega\right)\hat{\boldsymbol{\sigma}}' - \dot{\omega}\left(1 - \chi\right)\hat{\boldsymbol{\sigma}}' \\
&= \boldsymbol{E}_{sec} : \dot{\boldsymbol{\varepsilon}} - \boldsymbol{E}_{sec} : \left(\dot{\boldsymbol{\varepsilon}}^{ft} + \dot{\boldsymbol{\varepsilon}}^{tm}\right) - \dot{\chi}\left(1 - \omega\right)\hat{\boldsymbol{\sigma}}' - \dot{\omega}\left(1 - \chi\right)\hat{\boldsymbol{\sigma}}' \quad (6.53)
\end{aligned}$$

Following (6.48), the rate of the average pore pressure can be expressed as:

$$\dot{P}_{Pore} = \begin{cases} \dot{P}_G & \text{for } S \leq S_{SSP} \\ \dot{P}_G - \bar{S}\frac{\partial P_C}{\partial T}\dot{T} - \bar{S}\frac{\partial P_C}{\partial \tilde{\rho}_v}\dot{\tilde{\rho}}_v & \text{for } S > S_{SSP} \end{cases} \qquad (6.54)$$

Again, in Voigt's notation, the total stress rate may be expressed as:

$$\dot{\boldsymbol{\sigma}} = \dot{\boldsymbol{\sigma}}' + \dot{\boldsymbol{p}} \qquad (6.55)$$

where $\dot{\boldsymbol{p}}$:

$$\dot{\boldsymbol{p}} = \boldsymbol{p_T}\dot{T} + \boldsymbol{p_G}\dot{P}_G + \boldsymbol{p_V}\dot{\tilde{\rho}}_v \qquad (6.56)$$

and $\boldsymbol{p_T}, \boldsymbol{p_G}, \boldsymbol{p_V}$ are expressed as

$$\left.\begin{aligned}
\boldsymbol{p_T} &= \boldsymbol{0} \\
\boldsymbol{p_G} &= \left(\begin{array}{cccccc} 1 & 1 & 1 & 0 & 0 & 0 \end{array}\right)^T \\
\boldsymbol{p_V} &= \boldsymbol{0}
\end{aligned}\right\} \quad \text{for } S \leq S_{SSP}$$

$$\left. \begin{array}{c} \boldsymbol{p_T} = -\frac{\partial P_C}{\partial T} \left(\begin{array}{cccccc} 1 & 1 & 1 & 0 & 0 & 0 \end{array} \right)^T \\ \boldsymbol{p_G} = \left(\begin{array}{cccccc} 1 & 1 & 1 & 0 & 0 & 0 \end{array} \right)^T \\ \boldsymbol{p_V} = -\frac{\partial P_C}{\partial \tilde{\rho}_v} \left(\begin{array}{cccccc} 1 & 1 & 1 & 0 & 0 & 0 \end{array} \right)^T \end{array} \right\} \text{ for } S > S_{SSP}$$

6.6. Summary

The presented coupled hygro-thermo-mechanical model can be used for the simulation of the full behaviour of concrete structures when exposed to thermo-mechanical loading. The final strain rate of the presented Glasgow model is shown in (6.57). The incremental form of the stress rate, in Voigt's notation can be seen in Equation (6.58). It can be noted that the transient creep strain term, $\boldsymbol{M}^-\boldsymbol{\sigma'}^-$, utilises the Bishop's stress rather than the total stress. Finally, using the set of primary variables $\mathbf{u} = \left(\begin{array}{cccc} \mathbf{u} & T & P_G & \tilde{\rho}_V \end{array} \right)^T$, it is possible to define the additional coupling terms of the system of differential equations (3.36), which results in Equations (6.59) to (6.65).

$$\dot{\boldsymbol{\varepsilon}} = \dot{\boldsymbol{\varepsilon}}^e \left(\sigma, T \right) + \dot{\boldsymbol{\varepsilon}}^{ft} \left(T \right) + \dot{\boldsymbol{\varepsilon}}^{tm} \left(\sigma, T \right) \tag{6.57}$$

$$
\begin{aligned}
d\boldsymbol{\sigma} \;=\; & \boldsymbol{E}_{sec} d\boldsymbol{\varepsilon} - \boldsymbol{E}_{sec} \left(\boldsymbol{m} dT + \boldsymbol{M}^- \boldsymbol{\sigma'}^- dT \right) - \\
& - \; (1 - \omega) \, \hat{\boldsymbol{\sigma}}' d\chi - (1 - \chi) \, \hat{\boldsymbol{\sigma}}' d\omega - \boldsymbol{p_T} dT - \boldsymbol{p_G} dP_G - \boldsymbol{p_V} d\tilde{\rho}_v
\end{aligned}
\tag{6.58}
$$

$$\boldsymbol{K}_{aa} = \int_V \boldsymbol{B}^T \left(\boldsymbol{E}_{sec} - H_1^{md} \left(1 - \chi \right) \hat{\boldsymbol{\sigma}}' \boldsymbol{s}^T \right) \boldsymbol{B} dV \tag{6.59}$$

$$
\begin{aligned}
\boldsymbol{K}_{aT} \;=\; & -\int_V \boldsymbol{B}^T \left[\boldsymbol{E}_{sec} \boldsymbol{m} + \boldsymbol{E}_{sec} \boldsymbol{M}^- \boldsymbol{\sigma'}^- + (1 - \omega) \, H^{td} \hat{\boldsymbol{\sigma}}' + (1 - \chi) \, H_2^{md} \hat{\boldsymbol{\sigma}}' \right. \\
& - \; \left. (1 - \chi) \, H_1^{md} \hat{\boldsymbol{\sigma}}' \boldsymbol{s}^T \left(\boldsymbol{m} + \boldsymbol{M}^- \boldsymbol{\sigma'}^- \right) + \boldsymbol{p_T} \right] \boldsymbol{h}_T^T dV
\end{aligned}
\tag{6.60}
$$

$$\boldsymbol{K}_{aP} = -\int_V \boldsymbol{B}^T \boldsymbol{p_G} \boldsymbol{h}_G^T dV \tag{6.61}$$

$$\boldsymbol{K}_{a\rho_V} = -\int_V \boldsymbol{B}^T \boldsymbol{p}_V \boldsymbol{h}_{\rho_V}^T dV \tag{6.62}$$

$$\boldsymbol{K}_{Ta} = \boldsymbol{0} \tag{6.63}$$

$$\boldsymbol{K}_{Pa} = \boldsymbol{0} \tag{6.64}$$

$$\boldsymbol{K}_{\rho_V a} = \boldsymbol{0} \tag{6.65}$$

It has to be noted that the presented formulation does not allow for full two directional coupling of all the components. The mechanical influence on the transport model is obviously taken into account through $\boldsymbol{K}_{aT}$, $\boldsymbol{K}_{aP}$ and $\boldsymbol{K}_{a\rho_V}$. However, the influence of the transport model on the mechanical properties is not fully obtained as seen through $\boldsymbol{K}_{Ta}$, $\boldsymbol{K}_{Pa}$ and $\boldsymbol{K}_{\rho_V a}$. The mechanical influence is taken into account indirectly through damage parameters, which influence porosity and permeability.

The Enhanced Glasgow Model presented in this thesis therefore represents a coupled hygro-thermo-mechanical model for concrete.

7. Hygro-Thermo-Mechanical simulations

The main objective of this chapter is to investigate the performance of the hygro-thermo-mechanical model with emphasis on the mechanical part, which was introduced in the Chapter 6. This is achieved by the analysis of two different problems:

1. A problem of concrete column exposed to fire

2. A life cycle of a nuclear prestressed concrete pressure vessel

The first example is a benchmark problem of concrete column exposed to fire loading, similar to the previously investigated within the validation process (see section 4.2). This example is presented to consider the consequences of incorporating a damage model in a transient analysis. It demonstrates the evolution of the damage zone, which is induced by the build up of the pore pressure and the thermal strains. This additional capability of the model provides the ability to predict spalling.

The final example problem considers a life cycle of a nuclear prestressed concrete pressure vessel. The concrete containment pressure vessel, within the nuclear reactor surrounding, experiences a moderate heating regime and illustrates the capability of the Enhanced Glasgow model to predict the behaviour of an existing concrete structure.

7.1. Numerical example of coupled problem

After an introduction of the important mechanical part of the hygro-thermo-mechanical formulation in Chapter 6, the capability of this part of the model is presented here. The simplest possible example is the one similar to that

Figure 7.1.: Mesh for coupled problem

presented in section 4.2, with the addition of the mechanical response, including material damage. For simplicity, no changes to the geometry are made. However, material properties are changed to accommodate the higher strength concrete, which is predicted to exhibit more serious damage scenarios due to heating. Additionally, a finer mesh is introduced, as presented in figure 7.1. There are 960 4-node quadrilateral elements and 8 linear boundary elements. The lateral boundary conditions are modified to be able to capture spalling phenomena within 1D formulation. Therefore, they are applied to avoid the built up of lateral thermal stresses across the specimen. The middle line is restrained in perpendicular direction, where the top side is clamped.

Concrete parameters in the presented example are corresponding to higher strength concrete with compressive strength of 60MPa and tensile strength at the lower bound of 2.45MPa. The parameters used during simulation are: 9.4% of porosity, 79% of relative humidity and initial intrinsic permeability at the level of 1.8e-20. A simple estimate of the initial history parameter can be reached based on Equation (6.36) and $\kappa_0^{md} = 0.0001$.

The solution scheme is an iterative, mid-point time stepping algorithm with 1 seconds time step up to the damage occurrence, and 0.01 thereafter. The maximum number of iterations is limited to 12. Checks on convergence showed that the model rarely reached this number and increasing the maximum number of iterations made negligible difference to the solution. The convergence criteria is 10^{-6} for the energy norm.

7.1.1. Results

There are four different cases under consideration. In all of them the Enhanced Glasgow Model with hygral, thermal and mechanical components is taken into account. The first case does not include the mechanical damage, thus it is similar to the example presented in section 4.2, except for the

fact that the high strength concrete properties are used instead of normal strength concrete properties. The effects of thermal damage are considered. This example will be used as a reference benchmark case and it will be compared to the next case, which considers both thermal and mechanical damage. Therefore, the second case can capture spalling initiation, if applicable. The difference in the distribution of transport variables will be compared against the reference case.

The additional cases investigate the influence of important mechanical aspects. First, the influence of free thermal expansion is considered and thus in third case the coefficient of the thermal expansion is set to 0. Next, the results are compared to the second case. This is followed by the fourth case, where the effects of load induced thermal strain (*lits*) are considered. This is achieved by setting the *lits* parameters to 0 and again comparing the results with the second case.

7.1.1.1. Case 1 - Influence of mechanical damage

As previously mentioned, the first case did not include the effects of mechanical damage and essentially it is similar to the analysis presented in section 4.2. Therefore, it is not presented here in great details. The main aspects are discussed, which are necessary for the comparison with the next case.

First, the gas pressure distributions for two different times are presented in Figure 7.2. Additionally, the evolution of tensile stress, based on equation (7.1) within the section is also presented on the same graph. It can be clearly seen that the gas pressure curve is reaching the calculated tensile strength of the specimen at time 950 seconds, thus the initiation of mechanical damage will be expected in the next case at this time step. At time equal to 1086 seconds, the tensile strength is clearly exceeded. This is not expected to be seen in the next case. For completeness, the vapour content profiles and evolution of intrinsic permeability for previously mentioned time steps are presented in Figures 7.3 and 7.4 , where it can be observed that the uniform increase is recorded.

$$f_t\left(T\right) = f_{t0}\left(1 - \left(0.2\left(\frac{T}{100}\right) - 0.1\left(\frac{T}{100}\right)^2\right)\right) \tag{7.1}$$
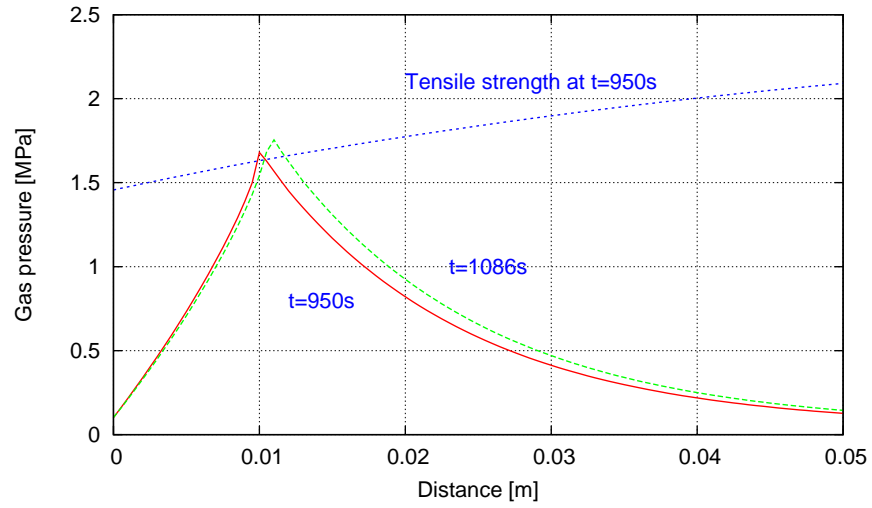
Figure 7.2.: Gas pressure profiles and estimated tensile strength based on (7.1) for case 1
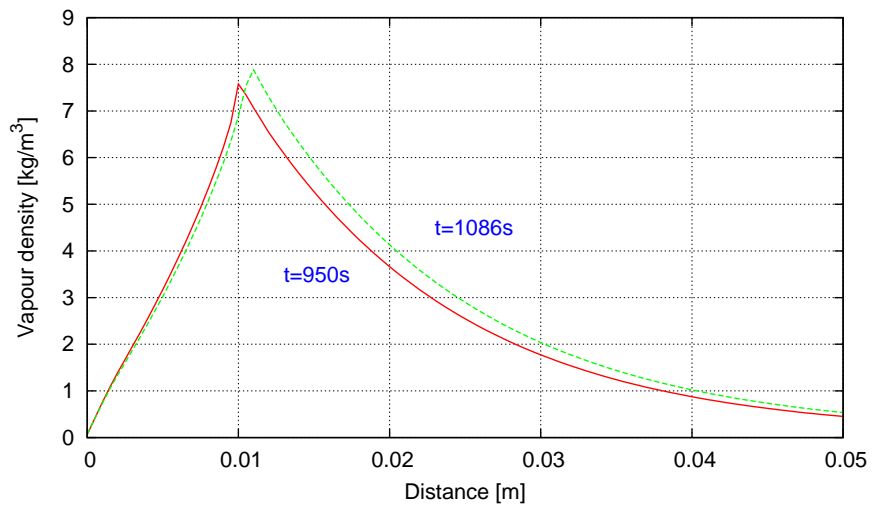
Figure 7.3.: Vapour content profiles for case 1

Figure 7.4.: Intrinsic permeability profiles for case 1

7.1.1.2. Case 2 - Full Enhanced Glasgow Model

In this analysis, both thermal and mechanical damage is considered. As discussed in previous section, the initiation of damage is expected at $t = 950$ and it is shown in Figures 7.5 a) and 7.6. This effect corresponds to the position of the maximum gas pressure, which approaches $P_G = 1.8$MPa. Figure 7.5 b) clearly shows a localised damage zone at $t = 1070$ seconds. After only another 16 seconds, damage has spread towards the heated surface, Figure 7.5 c) and 7.7. The final damage state is shown in Figure 7.5 d) at $t = 1800$ seconds.

The evolution of temperature within the specimen under the ISO fire curve is presented in Figure 7.8. It can be seen that the temperature gradient is drying the surface of the concrete column and transforming the initial liquid into vapour. This phenomenon over-saturates the nearby area and a "moisture-clog" formation starts. Part of the moisture is pushed further into the colder part of the concrete due to the pressure gradient at the back of the clog. This "moisture clog" area of localised increase in vapour content can be observed in Figure 7.9. This effect is associated with a build-up of gas pressure and is presented in Figures 7.10 and 7.11. The gas pressure peak value of 1.78MPa is localising at approximately 1 cm away from the heated surface after 950 seconds. Therefore, the coupled effect of thermal stresses and gas pressure is exceeding the reduced tensile strength
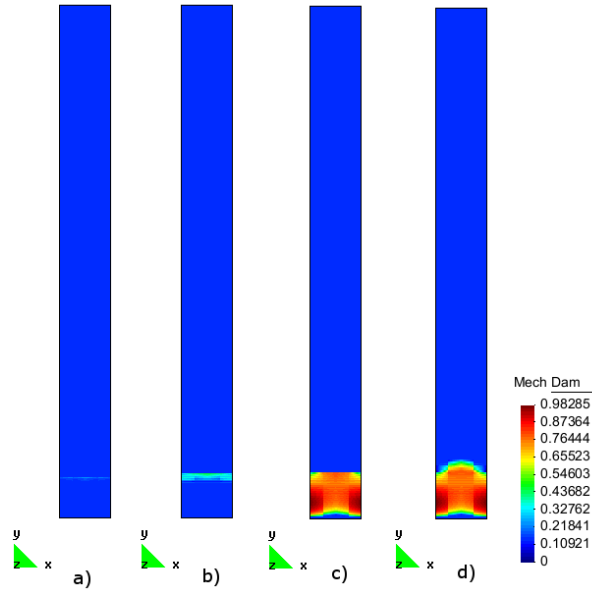
Figure 7.5.: Profiles of mechanical damage evolution for case 2 at a)$t = 950sec$, b)$t = 1070sec$, c)$t = 1086sec$ and d)$t = 1800sec$.

of the assumed concrete class, what can be clearly seen in Figure 7.11, where the calculated tensile strength is imposed on the gas pressure graph, similarly to case 1 previously discussed. Additionally, it can be observed on the stress profiles in Figure 7.16. As a result local strain concentration starts to increase and spreads in the heating direction, as indicated in Figures 7.15 b) and c). The final gas pressure distribution is presented in the Figure 7.12, where the reduced pressure, due to the local increase in intrinsic permeability (Figure 7.14), can be seen.

After the damage initiation, the model predicted further damage for an additional 120 seconds, as can be seen in Figures a) and b) of 7.5 and 7.15. The final stage of the damage at 1800 seconds slightly increased comparing to the 'post spalling' stage. However, due to the continuous heating the build-up process continues further and all the described stages were repeated till an additional damage zone has been created further into the specimen after approximately 1100 seconds.

The first damage initiation took place at approximately 200°C, due to the pressure and thermal stresses build-up. This compares well with the experimental temperature levels quoted in Chapter 5, during the discussion on the effects of the addition of the polypropylene fibres.
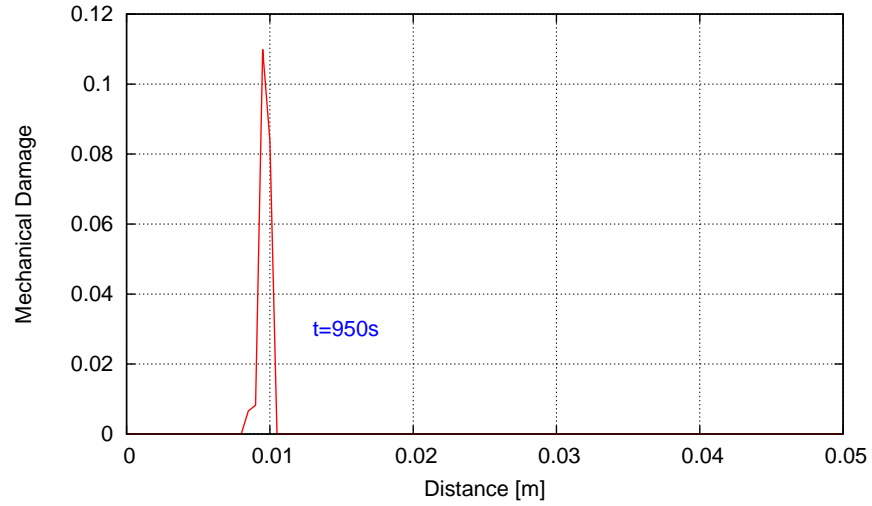
Figure 7.6.: Mechanical damage profile through the concrete section at $t = 950sec$ for case 2
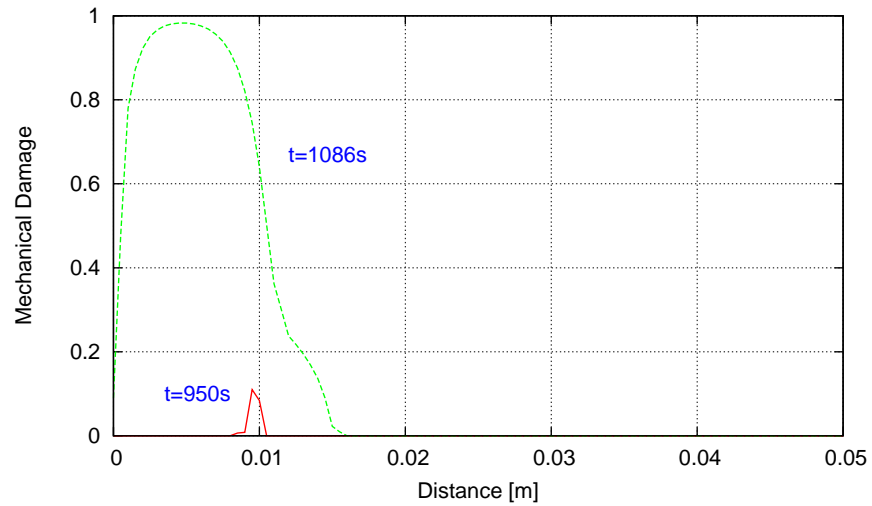
Figure 7.7.: Mechanical damage profile through the concrete section at $t = 950sec$ and $t = 1086sec$ for case 2
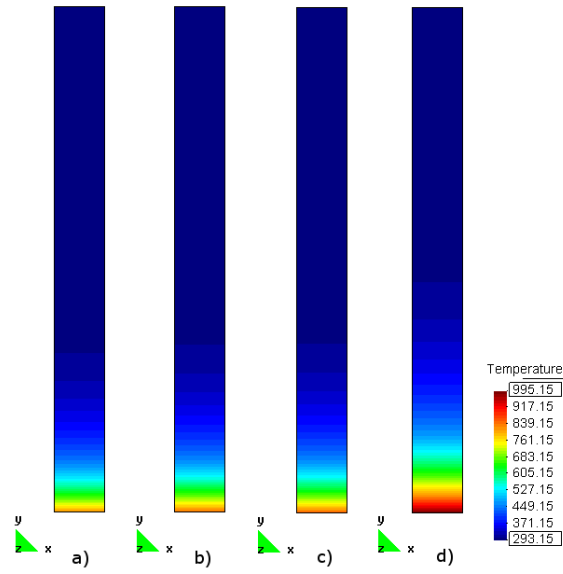
Figure 7.8.: Temperature profiles for case 2 at a)$t = 950sec$, b)$t = 1070sec$, c)$t = 1086sec$ and d)$t = 1800sec$.
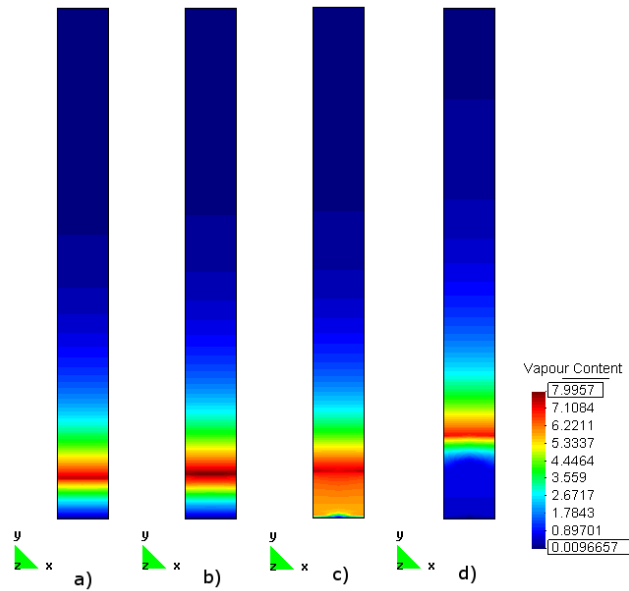
Figure 7.9.: Vapour content profiles for case 2 at a)$t = 950sec$, b)$t = 1070sec$, c)$t = 1086sec$ and d)$t = 1800sec$.
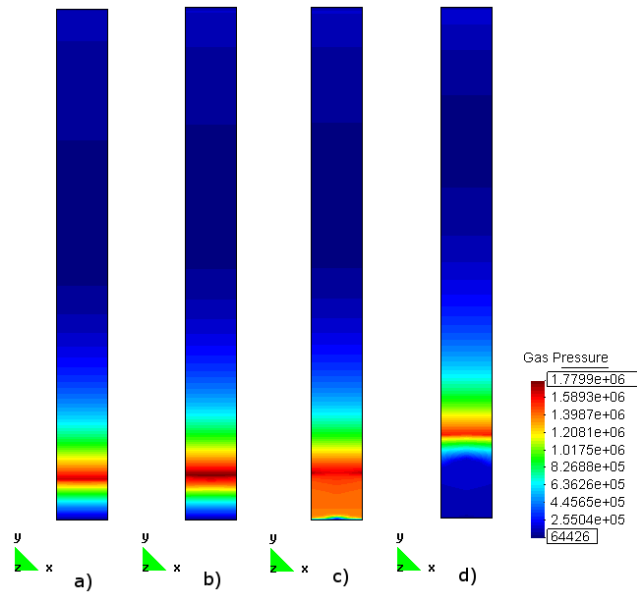
Figure 7.10.: Gas pressure profiles for case 2 at a)$t = 950sec$, b)$t = 1070sec$, c)$t = 1086sec$ and d)$t = 1800sec$.
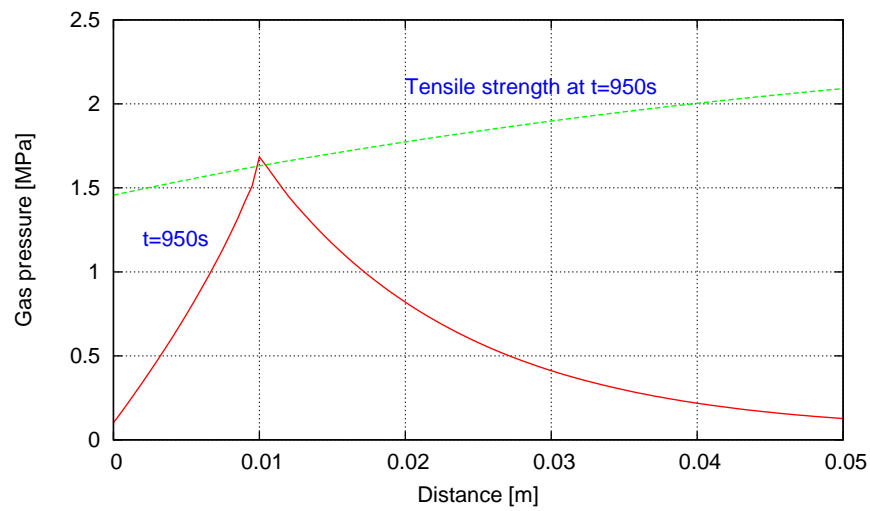
Figure 7.11.: Gas pressure profiles and estimated tensile strength based on (7.1) for case 2 at $t = 950sec$
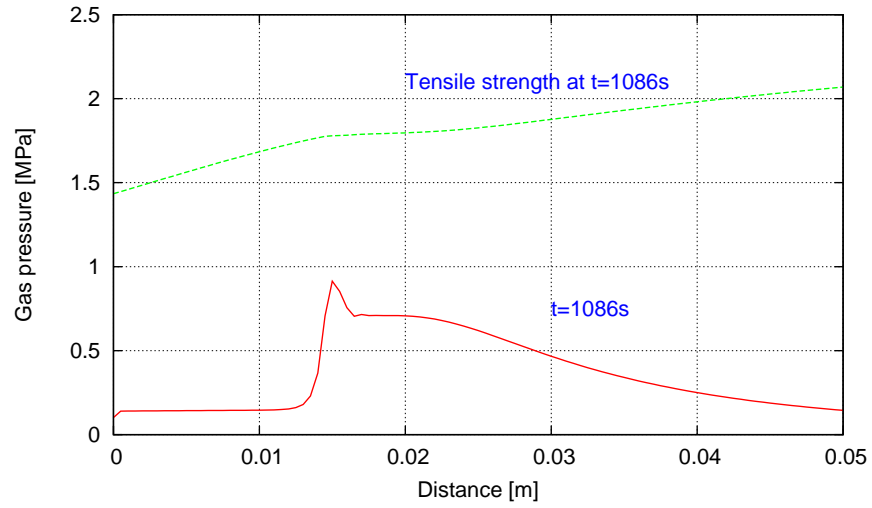
Figure 7.12.: Gas pressure profiles and estimated tensile strength based on (7.1) for case 2 at $t = 1086sec$
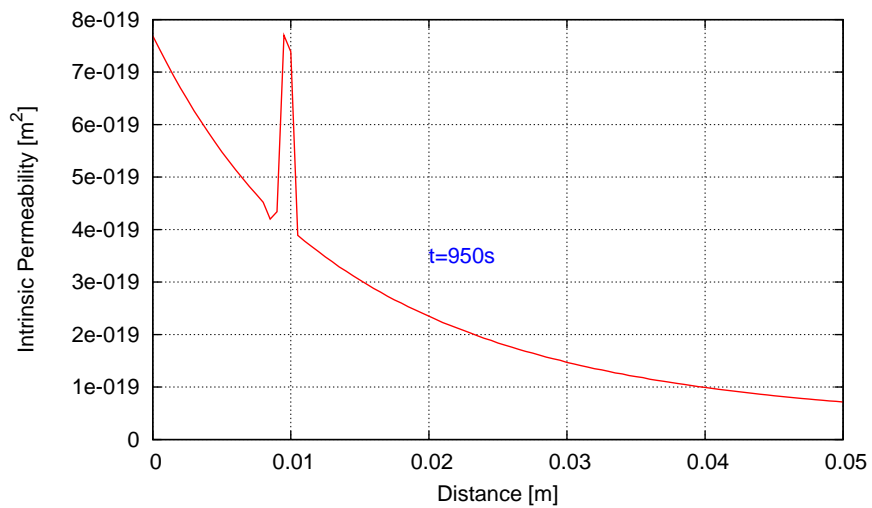
Figure 7.13.: Intrinsic permeability profiles for case 2 at $t = 950sec$
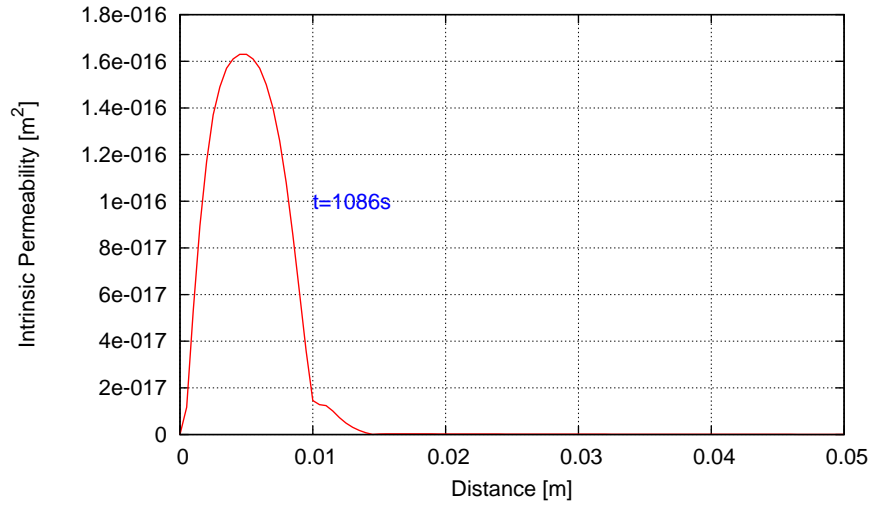
Figure 7.14.: Intrinsic permeability profiles for case 2 at $t = 1086sec$
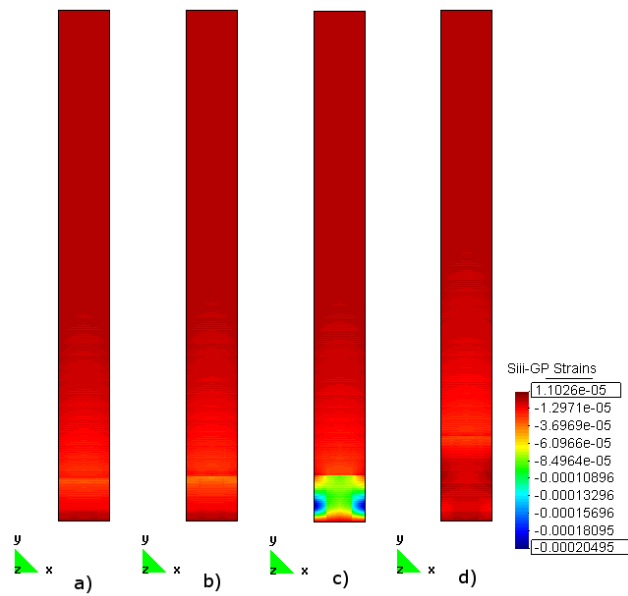
Figure 7.15.: Minimum principal strain profiles (non smoothed) for case 2 at a)$t = 950sec$, b)$t = 1070sec$, c)$t = 1086sec$ and d)$t = 1800sec$.
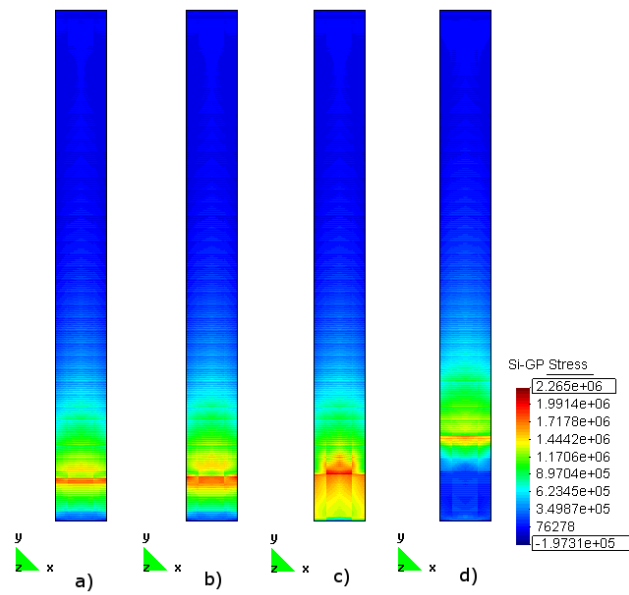
Figure 7.16.: Maximum principal stress profiles (non smoothed) for case 2 at
a)$t = 950sec$, b)$t = 1070sec$, c)$t = 1086sec$ and d)$t = 1800sec$.

7.1.1.3. Case 3 - Influence of free thermal expansion

Case 3 investigates the influence of the coefficient of free thermal expansion on the spalling prediction. The previous analysis, case 2, had taken into account this effect. Therefore, now the same analysis is undertaken with the coefficient of thermal expansion set to 0. All other parameters, including the boundary and initial conditions, are exactly the same.

In reality, additional strains due to the effect of free thermal expansion are introduced into the specimen. Therefore, it is expected that if this effect is neglected, the initiation of damage will be delayed. The results for this case are presented only for two distinct time steps. The first one is associated with time corresponding to the initiation of mechanical damage, where the second time is taken as $t = 1086sec$ to have a comparable results to case 2.

The damage initiation was recorded slightly later than for case 2, at time $t = 969sec$. Additionally, the damage profile at $t = 1086sec$ is reaching only 70% of the original profile. Both profiles are presented in Figure 7.17. When compared to previously presented damage evolutions (7.6, 7.7), it can be clearly seen that without free thermal expansion, damage is smaller at similar time steps.

This corresponds to the gas pressure evolution, which can be seen in Figure 7.18, where again the calculated tensile strength is imposed on the graph to present that with the addition of mechanical damage it cannot be exceeded by the gas pressure. The final gas pressure at $t = 1086sec$ is greater than the gas pressure presented in Figure 7.12 for case 2, due to the less damage in the specimen. Similar situation can be seen in Figure 7.19, which presents the vapour content. The vapour did not escape yet as the built up of intrinsic permeability, which is presented in Figure 7.20, is not as extensive as it was in the comparable case 2 (Figure 7.14).

Therefore, the influence of free thermal expansion is not critical, but has an influence on the model behaviour, especially on the time, instant of the initial damage occurrence. It needs to be highlighted that the presented problem is formulated in a way to reduce the possibility of built-up of thermal stresses, due to the application of boundary conditions.
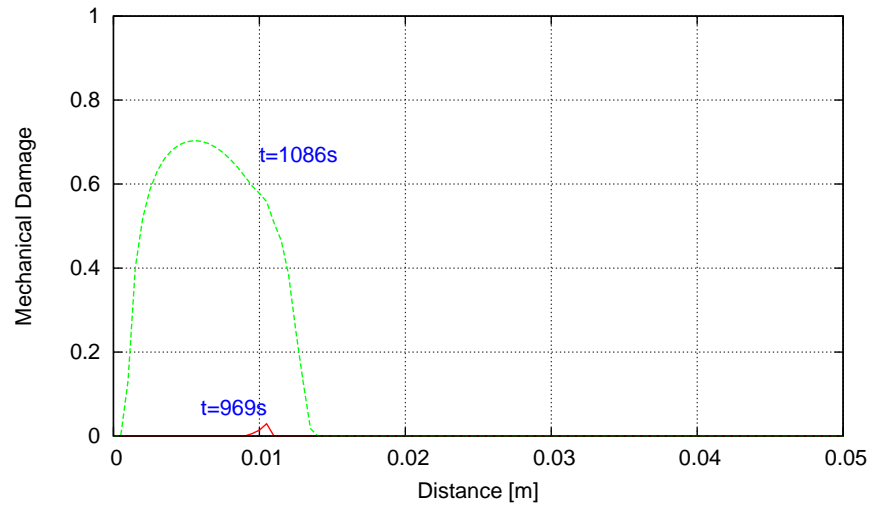
Figure 7.17.: Mechanical damage evolution throughout the section for case 3
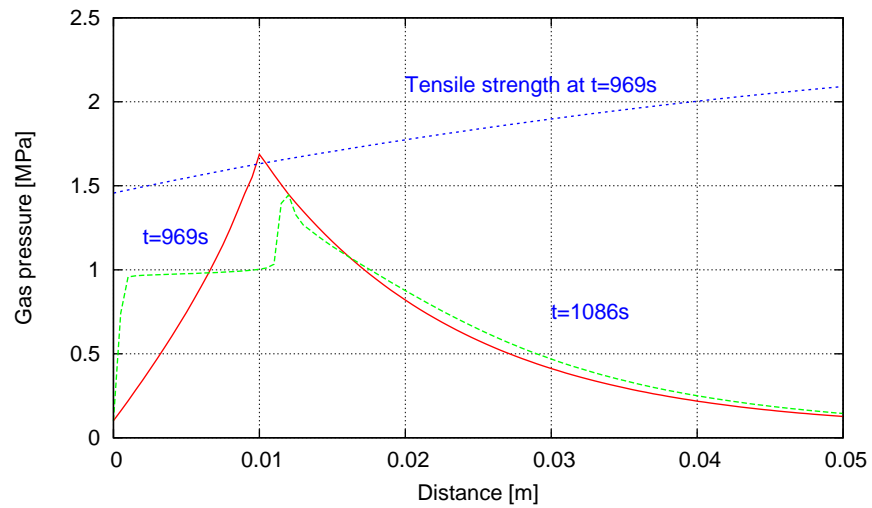
Figure 7.18.: Gas pressure profiles and estimated tensile strength based on (7.1) for case 3
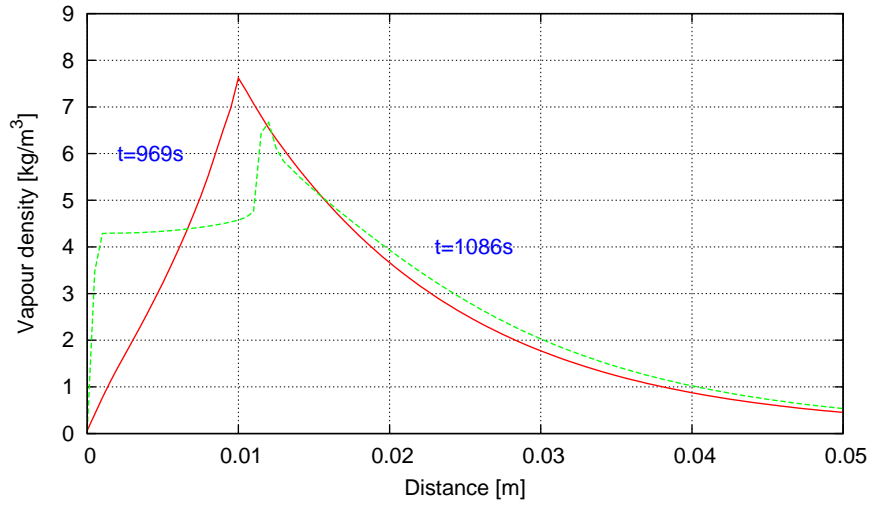
Figure 7.19.: Vapour content profiles for case 3
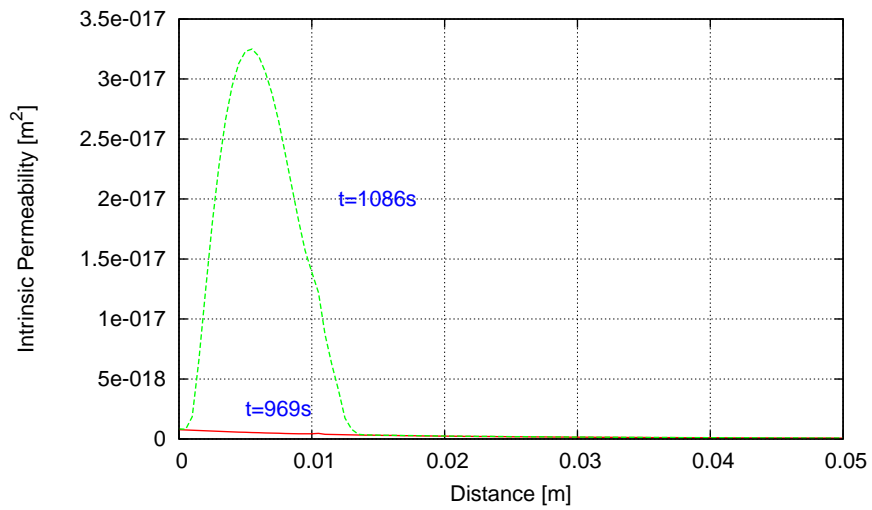
Figure 7.20.: Intrinsic permeability profiles for case 3

7.1.1.4. Case 4 - Influence of load induced thermal strain (*lits*)

The next case considers the effects of the load induced thermal strain (*lits*) and specifically the transient thermal creep. These effects are considered to be very important in concrete at elevated temperatures, as discussed in Chapter 6.

The investigation is undertaken by the deactivation of these effects and a comparison with the results of second case. In this case, similar to case 3, less severe situation than in case 2 is recorded. Again, the results for this case are presented only for two distinct time steps, where $t_1 = 950sec$ and $t_2 = 1086sec$.

The damage initiation was recorded at similar time as for case 2, at time $t = 950sec$. Additionally, the damage profile at $t = 1086sec$ is reaching around 86% of the original profile for comparable case 2. The comparison of these profiles is presented in Figure 7.22. These profiles can be compared to the case 2 results (7.6, 7.7) and it can be clearly seen that damage is smaller at similar time steps, when the transient thermal strains are not considered.

Consequently, less damage results in less severe increase in intrinsic permeability as can be seen in Figure 7.24. Therefore, the transport of vapour (Figure 7.23) and gas pressure relieve (Figure 7.21) is less pronounced than in case 2 (7.12).

Therefore, the influence of load induced thermal strain is again not critical, but has influence on the behaviour of the model, when severe heating conditions are considered.
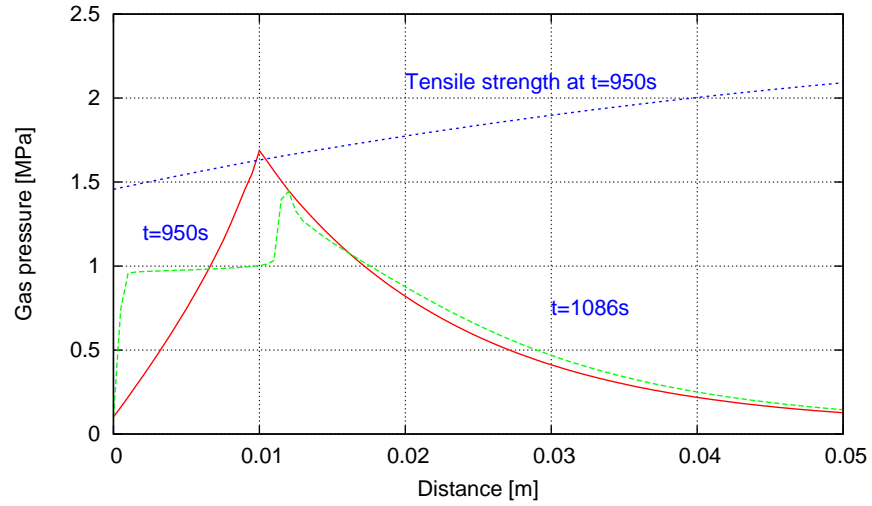
Figure 7.21.: Gas pressure profiles and estimated tensile strength based on (7.1) for case 4
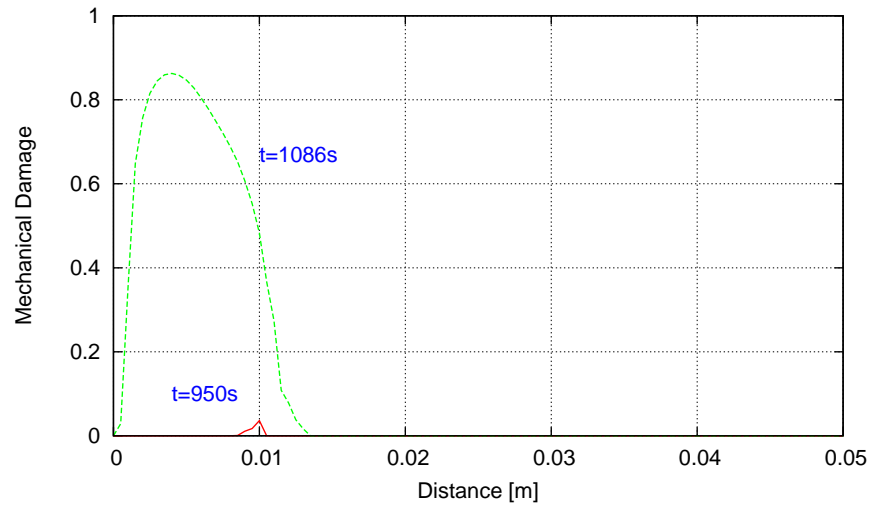
Figure 7.22.: Mechanical damage evolution throughout the section for case 4
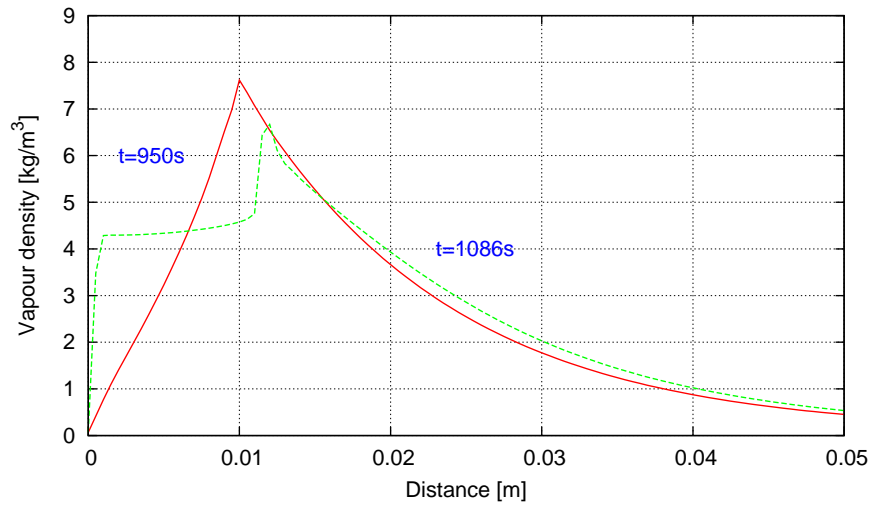
Figure 7.23.: Vapour content profiles for case 4
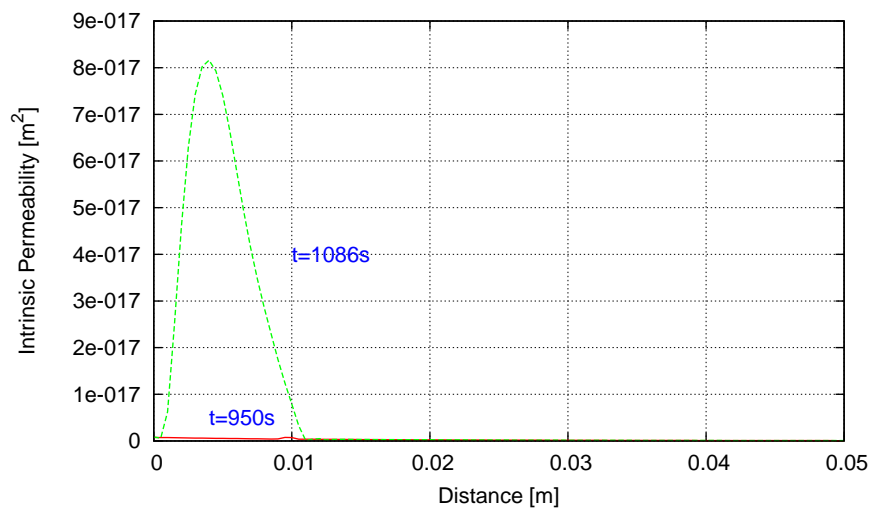
Figure 7.24.: Intrinsic permeability profiles for case 4

7.1.2. Summary

The results of the presented numerical simulation show that both pore pressure and thermally induced stresses can be identified as responsible for the spalling occurrence, and that their role depends on the particular conditions. The maximum recorded gas pressure for the presented example is 1.78MPa, where the maximum recorded principal stress is 2.26MPa. Therefore there is a difference of 0.48MPa, which can be associated with the stress induced by thermal strains. Experimental data to compare the simulated results are not available, which would provide an invaluable validation of the presented analysis. However, the presented simulation results agree with the descriptions available in the literature such as [7, 26, 39, 71]. Additionally, it was identified that the pressure build-up played a major role in the discussed case. Therefore, it agrees well with the author's statement on the importance of the pressure build-up during the fire situation.

All the additional investigations presented the importance of different aspects of this modelling approach, where all hygral, thermal and mechanical aspects are important. The short summary of comparison of the results for cases 2,3 and 4 is presented in the table below. It can be clearly seen that the spalling initiation and its effects can be captured, when all the mechanical aspects are considered.

	time	Case 2	Case 3	Case 4
Mechanical damage	t_1	0.11	0.03	0.04
[-]	t_2	0.98	0.7	0.86
Permeability	t_1	$7.7 \cdot 10^{-19}$	$4.7 \cdot 10^{-19}$	$5 \cdot 10^{-19}$
$[m^2]$	t_2	$16.3 \cdot 10^{-18}$	$3.2 \cdot 10^{-18}$	$8.1 \cdot 10^{-18}$
Gas Pressure	t_1	1.78	1.78	1.78
[MPa]	t_2	0.91	1.44	1.24
Vapour content	t_1	7.6	7.6	7.6
$[kg/m^3]$	t_2	4.4	6.6	5.7

Table 7.1.: Comparison of important variables for cases 2,3 and 4 at $t_1 = 950sec$ and $t_2 = 1086sec$, except for case 3, where $t_1 = 969sec$.

7.2. Nuclear concrete reactor vessel during real life conditions

The previously presented example was a generic benchmark coupled problem, which highlighted the possibilities of thermal and mechanical damage prediction. This section presents a more realistic case study of a life cycle of concrete reactor pressure vessel.

One of the main parts of the reactor in the nuclear power plant is the pressure vessel. It is a large scale structure with thick walls and it often weighs more than 300 tons. The pressure vessel surrounds and protects the reactor core. It provides a safety barrier and holds the fuel assemblies, the control rods, and the coolant/moderator. There are steel and concrete pressure vessels. In this dissertation only the concrete ones are considered.

The pressure vessel is located inside the containment building, which is made of thick concrete that is reinforced with adequate steel reinforcement bars. An example of the prestressed concrete containment vessel(PCCV) can be seen in Figure 7.25. This is a 1/4-scale model, which was tested by Sandia National Laboratories in September 2000. This test was undertaken to establish how much pressure full-scale PCCVs could tolerate in severe nuclear power plant accidents. During the test, engineers were gradually increasing the internal gas pressure. When the internal pressure inside the model was approaching 2.5 times the model's design pressure, test engineers detected and verified a leak in the vessel. The maximum internal pressure during the test was about 3.1 times the design pressure.

Such tests, as well as ageing nuclear power plants across Europe, inspired research communities to investigate ageing of PCCVs and Prestressed Concrete Reactor Vessels (PCRV). Under the EU MAECENAS project [14], the University of Glasgow computational mechanics group was involved in the research program that was looking into the behaviour of PCRVs during 33 years of service loads.

With reference to this project, the model presented in this thesis is used to predict the state of the PCRV during its service. The actual service loadings for temperature, internal pressure, as well as prestressed state for 33 years are presented in Figure 7.26. It can be seen that initially the pressure vessel is prestressed to the level of 1.2 MPa. After that level is

Figure 7.25.: Sandia National Laboratories test of a 1/4-scale model of a prestressed concrete containment vessel (PCCV) at an operating nuclear power plant in Japan.

(a) Temperature
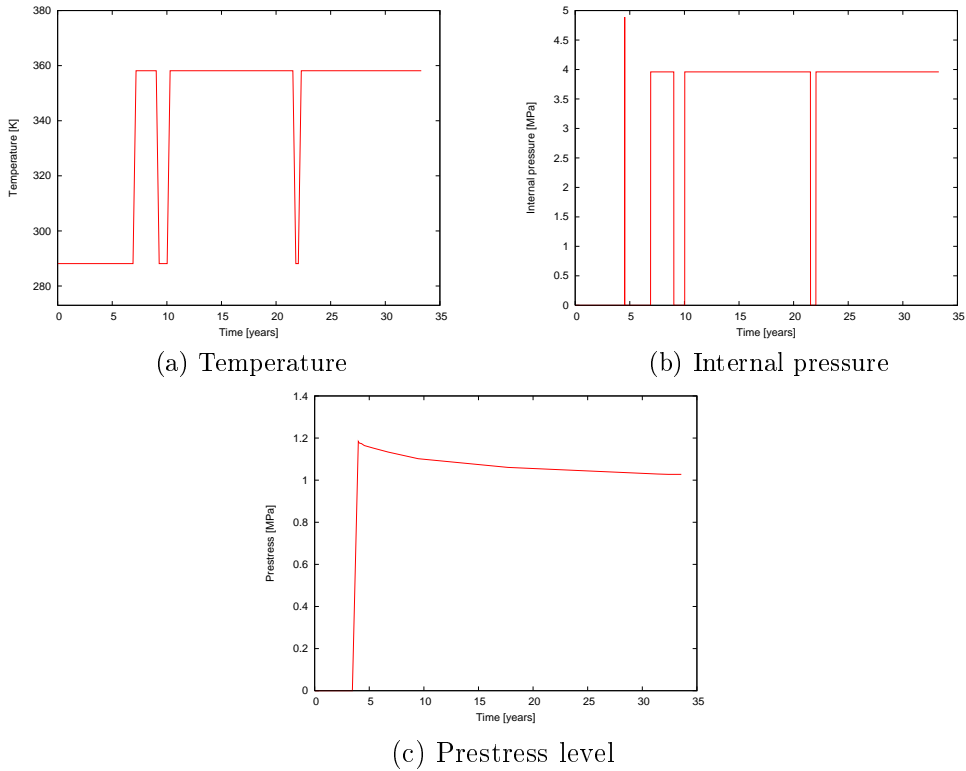

(b) Internal pressure

(c) Prestress level

Figure 7.26.: Temperature, internal pressure and prestress profiles for PCCV

reached a test pressurisation of up to 5 MPa of the vessel is undertaken to observe, whether it is free of any defects and leaks. Subsequently, when the test is satisfied, it can start normal service, during which the maximum service temperature reaches 85°C at the top part of the internal face and the internal pressure is close to 4 MPa.

7.2.1. Problem definition

The reactor vessel has an outer radius of 15.164 meters and an inner radius of 9.95 meters. The reactor vessel is 35.622 meters high. It is sealed on the internal face and open to the environment on the outer face. An axisymmetric finite element model consists of 5526 8-noded quadrilateral elements and 272 second order linear boundary elements, which results in 17021 nodes. Model is supported by series of spring elements at the bottom. The radial prestressing force is applied as an equivalent radial pressure on

the right side of the model. Additionally, a vertical prestress pressure is applied at the top of the PCRV. The internal pressure is applied on the inside of the chamber, what is indicated with the red colour in the Figure 7.27. The rest of the common variables used during the analysis can be found in Appendix D.

The solution scheme is an iterative, mid-point time stepping algorithm with 24 hours time steps and limited to 10 iterations. Checks on convergence showed that the model did not reached this number. The convergence criteria is at level of 10^{-6} for the energy norm.

Concrete parameters are taken for high strength concrete with compressive strength at 60MPa and tensile strength of 4MPa. Based on the information from the previously mentioned MAECENAS project, corresponding values of the important parameters are: 9% of porosity, 85% of relative humidity and initial intrinsic permeability at the level of 2.0e-18.

The analysis was undertaken for temperature history of 30 years of the PCRV, corresponding to a typical life span of such structure, and the results are presented in the following section.

7.2.2. Results

The presented results consider all important intervals within the life cycle of the structure. The evolution of the primary variables (temperature, gas pressure and vapour content) are presented in Figures 7.29, 7.28 and 7.30 at three points, A, B and C, which are indicated in figure 7.27.

The graphs indicate the coupling of the various transport processes, with rapid changes in gas pressure and vapour content corresponding to changes in the temperature profile.

Figure 7.31 shows the temperature distribution after 22 and 30 years. The hottest part of the structure is the "top part" corresponding to the area with least cooling on the inner face. Again the gas pressure and vapour content (shown in Figures 7.32 and 7.30) mirror the distribution of temperature.

The maximum recorded gas pressure is slightly above 1.5MPa and is localised to the area of the reactor cap. Therefore, under the normal working conditions the gas pressure is far from the tensile strength of the pressure vessel of 4MPa. Thus no mechanical damage is expected from this action.
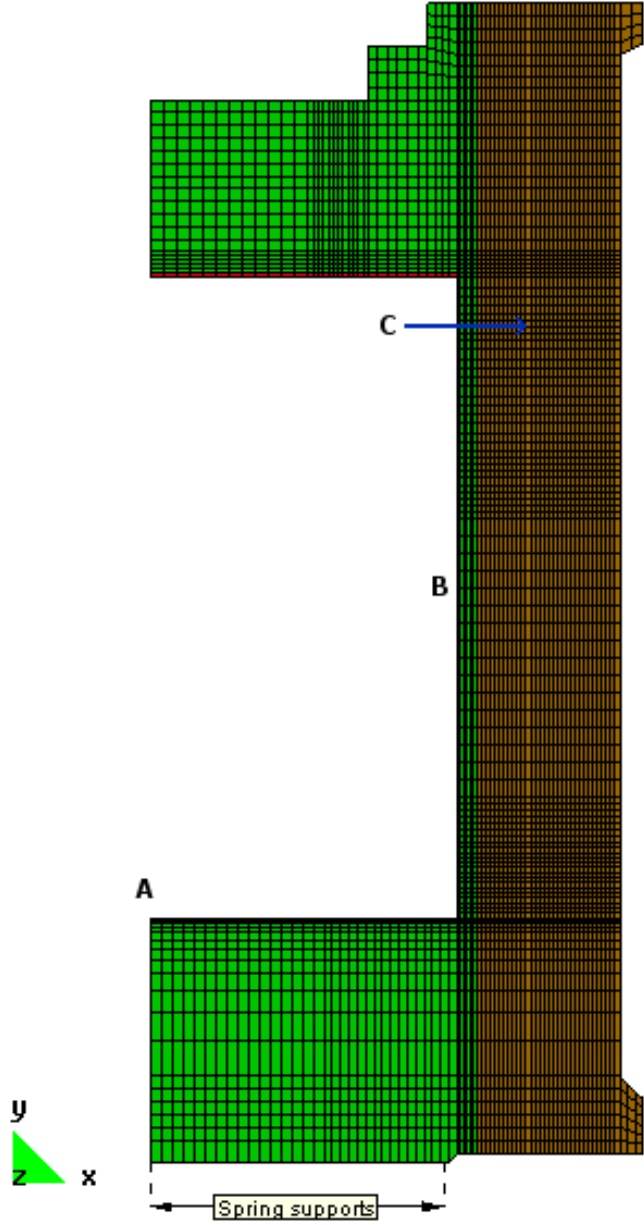
Figure 7.27.: Concrete pressure vessel - discretised model with boundary conditions.
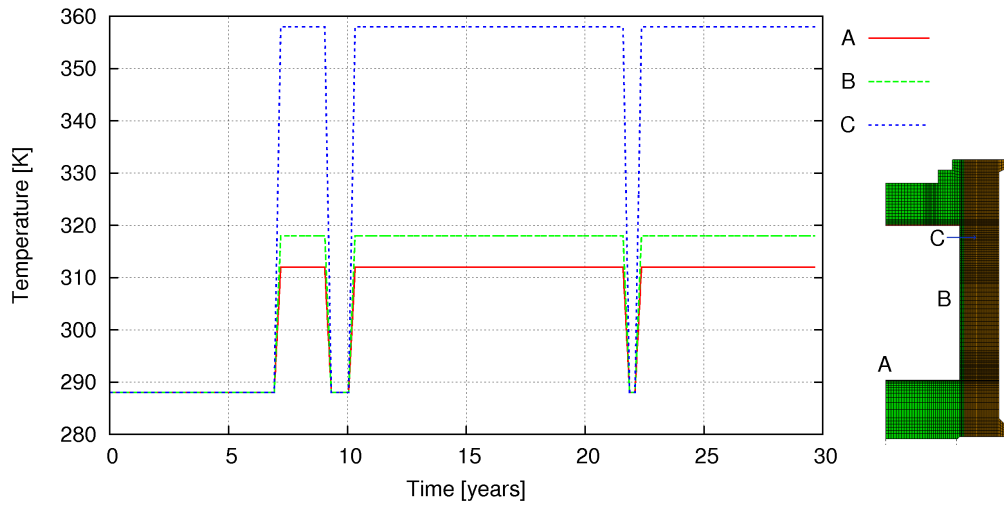
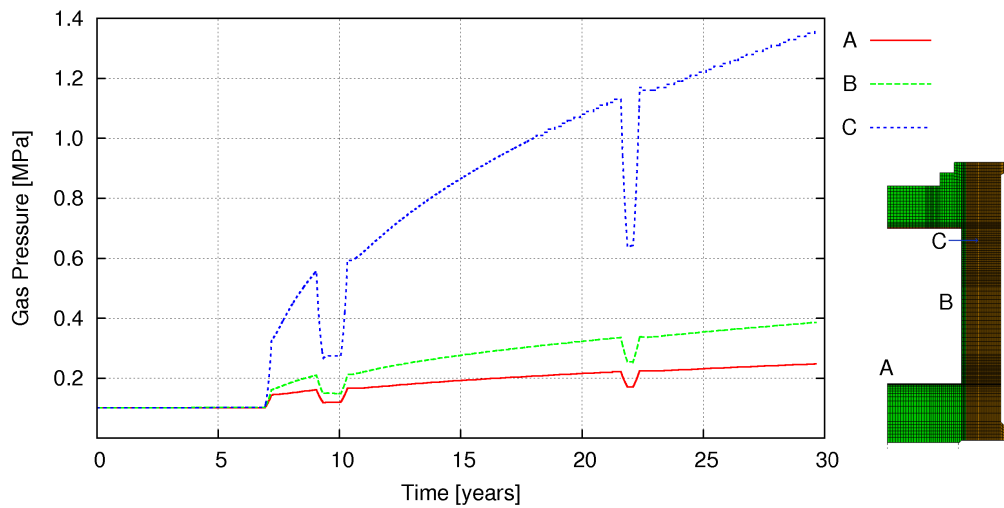Figure 7.28.: Evolution of temperature profiles for nodes A, B and C as indicated in figure 7.27

Figure 7.29.: Gas pressure evolutions for nodes A, B and C as indicated in figure 7.27
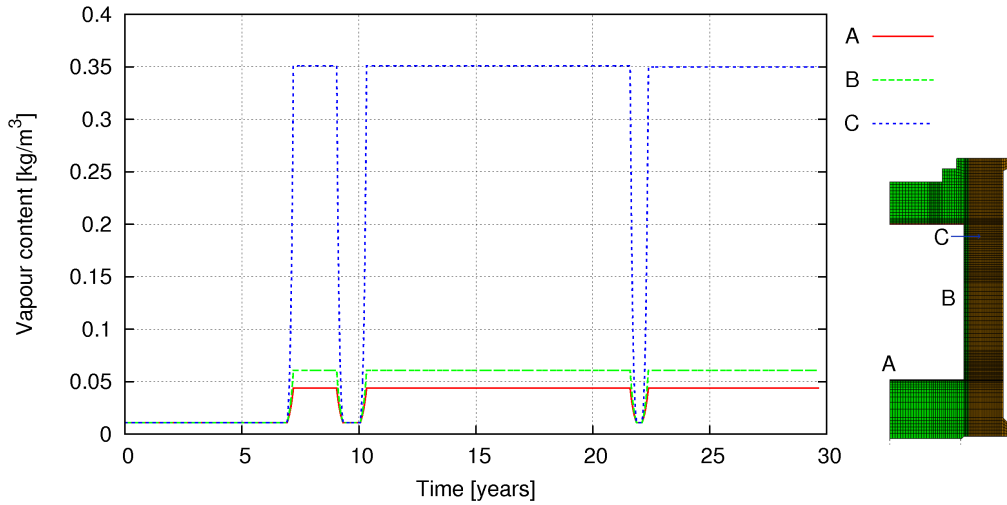
Figure 7.30.: Vapour content evolutions for nodes A, B and C as indicated in figure 7.27

The only damage that was experienced by the structure during the simulated 30 years is due to the thermal action. The profile of the thermal damage, which is essentially equal to total damage in this case, is presented in Figure 7.34. Due to the thermal damage there is an increase in the intrinsic permeability in the damaged zone of more than 3 times. The values of the mechanical damage that were registered in close proximity to the chamber corners, are negligible.

Additionally, a deflected shape of the structure is presented in figure 7.35. All the figures are magnified by a factor of 500 to visualise the behaviour of the pressure vessel. The initial self weight settles on the spring base. Afterwards, a gradual increase in prestress compresses the structure and allows future pressurisation. The final state of the structure, which is presented at the bottom of Figure 7.35, indicate full pressurisation of the inside chamber to the working conditions.

7.2.3. Summary

The presented simulation of pressurised concrete containment vessel during life cycle of 30 years provides an indication of the capabilities of the presented model. The concrete pressure vessel under normal working conditions experiences a moderate heating regime, which corresponds more with
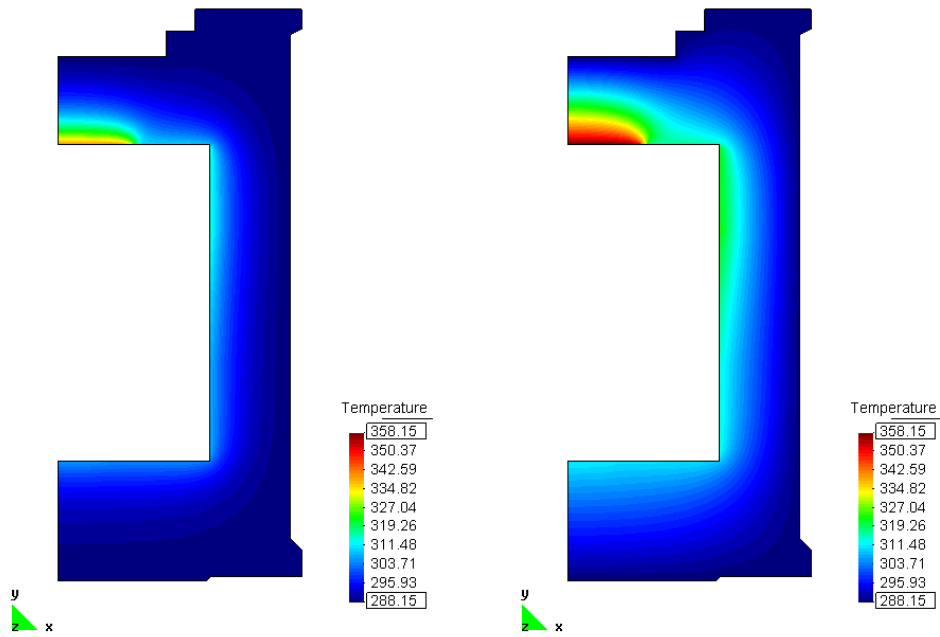
Figure 7.31.: Temperature profiles after 22 and 30 years
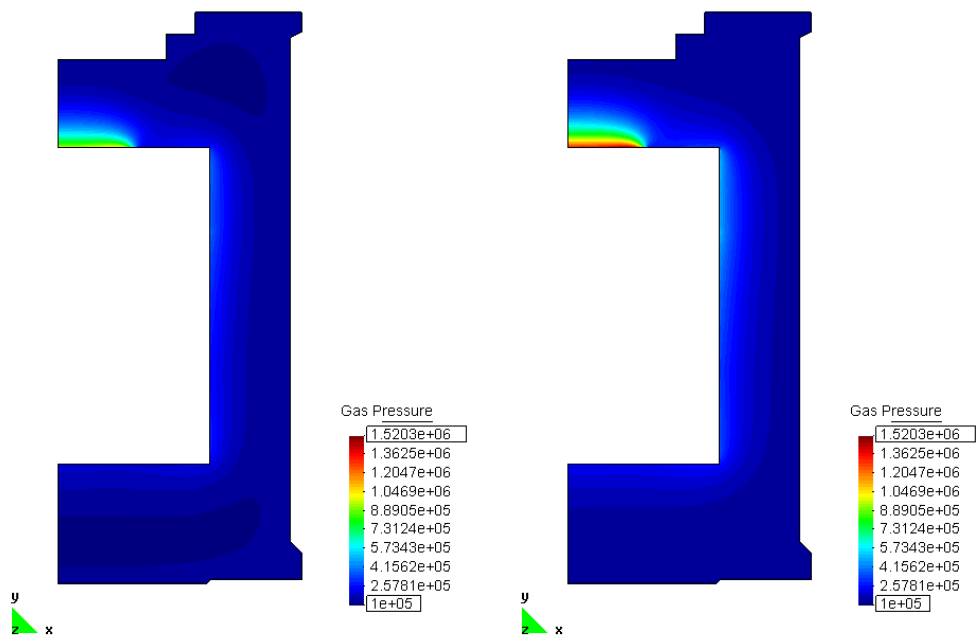
Figure 7.32.: Gas pressure profiles after 22 and 30 years
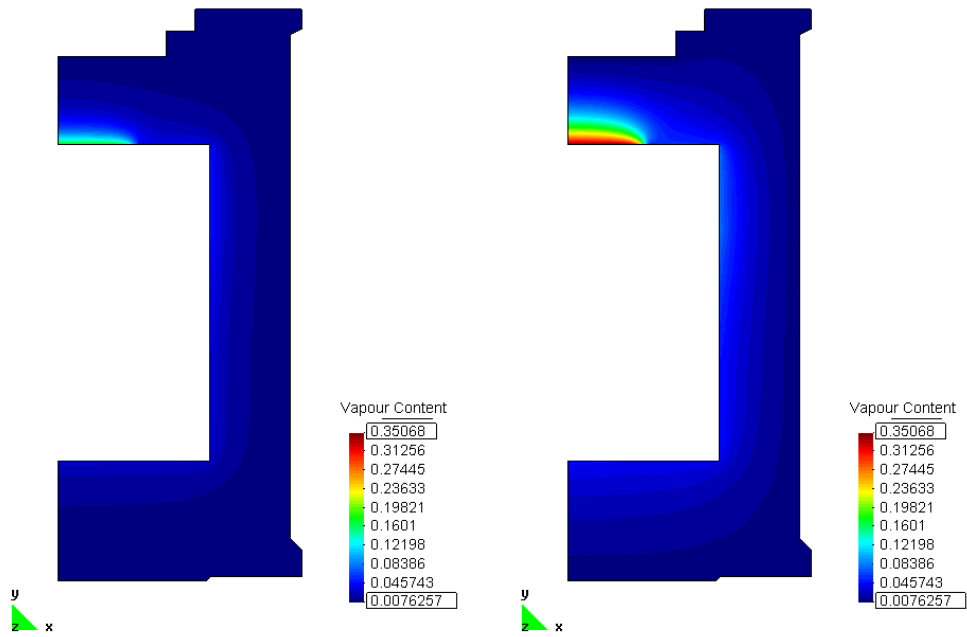
Figure 7.33.: Vapour content profiles after 22 and 30 years
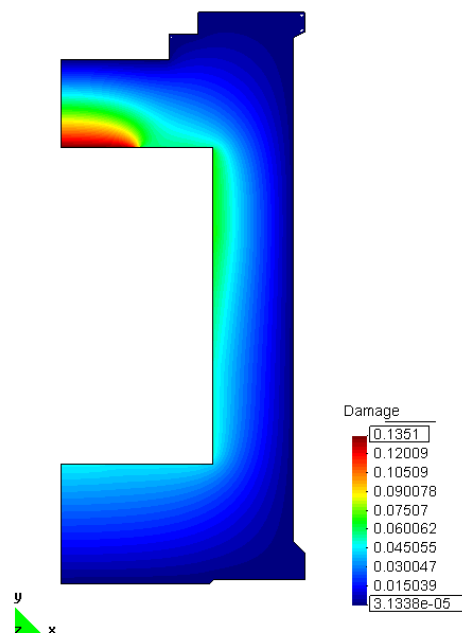
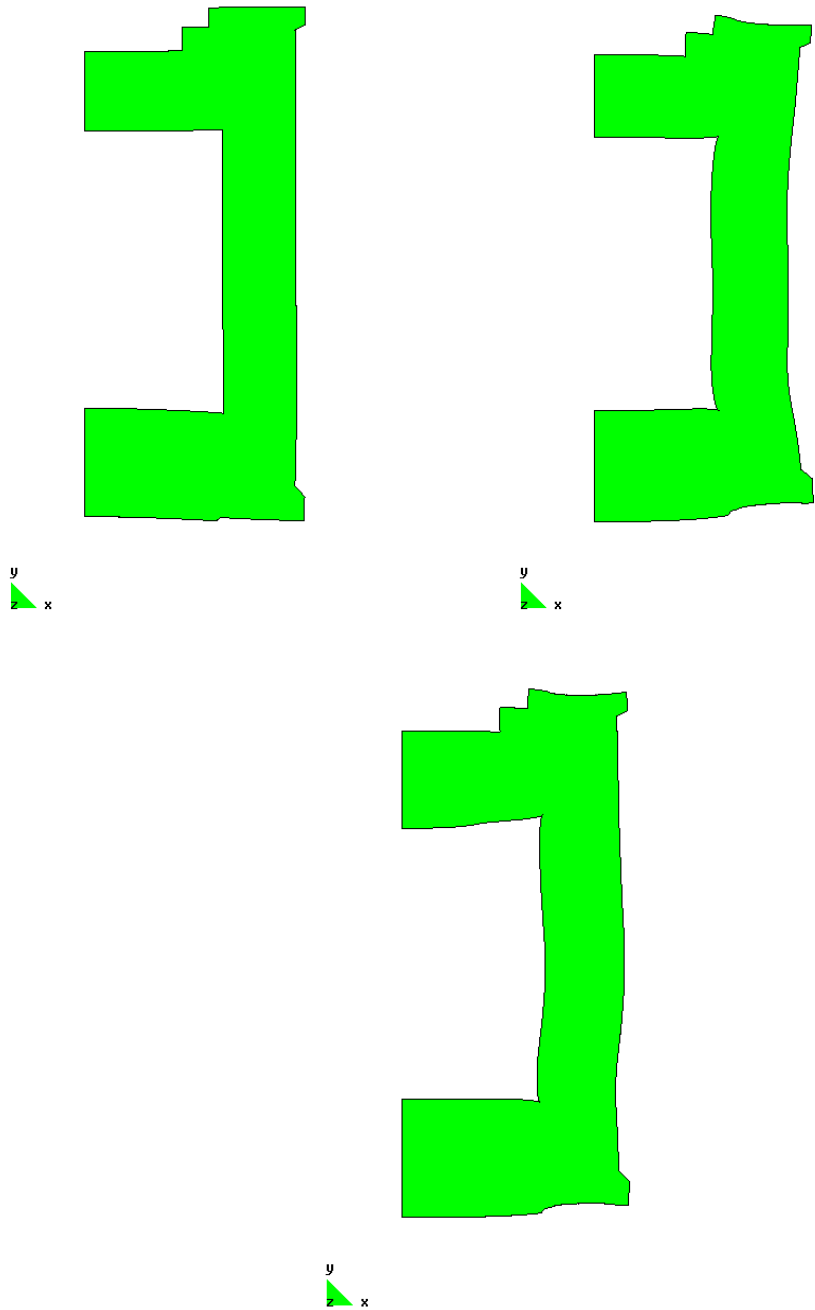Figure 7.34.: Final damage evolution after 30 years

Figure 7.35.: Deflected shape (factored by 500) after self weight (top right), prestress (top left) and pressurisation (bottom)

a drying problem than a fire conditions. All the model variables are not approaching their extreme values, therefore only a low degree of thermal damage is experienced. The full potential of the model could be used if an extreme event was introduced.

7.3. Conclusions

The up-to-date research, as already presented in literature overview in Chapter 1, explains the main reasons of the thermal spalling. As a result of high temperature gradients, the stored energy resulting from high values of restrained strains is released. Additionally, the temperature gradient increases the rate of moisture evaporation, which in turn causes the build-up of high pore pressure localised in the area close to the heated concrete surface. However, the relative importance of the two mechanisms is not yet determined and further studies seems essential.

The extension of the thermo-hygro model for concrete to include the mechanical damage, which was presented in Chapter 6, is concise and straightforward. It includes all the necessary phenomenas like free thermal expansion, creep and thermo-mechanical effects. All these effects, coupled with the heat and mass transport model enables the simulation of hygral, thermal and mechanical processes in concrete structures when exposed to ambient or elevated temperature conditions, especially spalling mechanisms that occur during rapid fire conditions. It has been shown that the numerical solution of these coupled multi-physics problems is successful and full of potential for further studies.

8. Conclusions and future

8.1. Summary of the undertaken work

The main aim of the presented work was the development of a reliable and coherent mathematical and computational formulation for the modelling of concrete behaviour, especially under severe heating conditions. As a result, a detailed and robust, finite element-based hygro-thermo-mechanical model for the predictive modelling of concrete has been presented, that has been verified and validated.

The thesis focuses initially on developing an improved heat and moisture transport model through the development and extension of the existing analytical, numerical and constitutive 'Glasgow Model' from Davie et al. [15]. Subsequently, the transport model is extended to incorporate coupled mechanical behaviour as well.

The sorption isotherms and permeability functions are identified as the most critical aspects of the transport model and this is reflected in the significant attention given to them in this thesis. The thesis introduces a new formulation for sorption isotherms that is based on the works of Leverett [45] and Baroghel-Bouny et al. [3]. The sorption curves capture different concrete types (normal and high strength) across a full range of temperatures within a single unified formulation, using a minimum of experimentally obtainable parameters. Differences between gas and liquid intrinsic permeability are accounted for by the introduction of the slip flow effect. Furthermore, the expression for relative permeability as a function of saturation is updated to make it more appropriate to concrete microstructures.

The predictions of moisture state for the drying problem are in line with

the experimental results, as are the mass loss predictions for the Kalifa heating problem presented in Section 4.3. Classical behaviour associated with heated concrete, such as moisture clog, gas pressure build-up, etc. are all captured by the presented model. The model also accommodates the influence of polypropylene fibres on the fluid transport in heated concrete in a phenomenological manner, based on experimental evidence. This enhances the applicability of the model and enables it to be used to investigate the inclusion of polypropylene fibres as a passive protection measure against thermal spalling.

Additionally, the thesis has introduced several new state equations, including saturation vapour pressure based on Hyland and Wexler [30], additional conductivity formulations based on concrete types and an alternative relationship for porosity as a function of temperature, based on experimental data.

This thesis has also explored the coupling of the transport formulation with a damage-based mechanical model to complete the full hygro-thermo-mechanical model that has been used to explore the complex behaviour of concrete at elevated temperatures. The Enhanced Glasgow Model has been validated against published experimental results and used for the analysis of larger scale problems.

The spalling phenomenon has also been investigated, although it is clear that more experimental data is required. The build-up of gas pressures, thought to be a major contributing factor in spalling, are predicted very well (Section 4.3 and 5.4) given the limited data available. However, simulations indicated that 20% of the final maximum stress that would cause spalling was not associated with the build-up of gas pressures and it is believed that thermal stresses are also important (Section 7.1).

Finally, the author has derived full set of constitutive equations, which are presented in Appendix B.

8.2. Model limitations and possible improvements

The presented model is a comprehensive tool, which can be used in predicting the transport processes, mechanical behaviour and coupled response of concrete elements under severe heating regime as well as for normal operating temperatures.

However, there are a number of limitations that could be addressed in the future. First, although the heat and moisture transport is influenced by mechanical and thermal damage, the influence of discrete cracks, for example, are not accounted for. Additionally, a coupling between continous and discontinous approach might be used.

Second, the damage model presented in Chapter 6 is a simple local model based on the fracture energy approach. A more extensive non-local model could be considered in the future, but this would increase the level of complexity. The fully coupled analyses presented in this thesis are computationally expensive and currently limited to single processor computers. Therefore, optimising the computer code for high performance parallel computer architectures would be extremely worthwhile, especially when considering 3D problems.

Next, the extension of the model to cooling regime, where the reversibility of the processess or its lack would be considered.

The presented formulation presents a mix of theoretical and empirical formulations. The next step could be a reduction of reliance on empiricism and introduction of theoretical formulations instead.

Other possible extensions include the application of homogenisation techniques. Based on the RVE concept, it is possible to calculate appropriate effective material properties based on knowledge of the microstructure (e.g. S. Nemat-Nasser and M. Hori [51]). Computational homogenisation represents an area of recent development (e.g. F. Feyel [20]) that utilises a nested finite element analysis procedure. Such approaches would permit some of the phenomenological relationships used in this thesis to be replaced by micro-mechanically inspired relationships. However, such homogenisation techniques have not yet, to the author's knowledge, been applied to the kind of complex coupled problems described in this thesis and represent

further computational complexity.

The suggested extensions seem worthwhile, however not essential. As mentioned before, parallel implementation of the code is thought to be the most necessary improvement of them all to render the simulation of more realistic problems.

8.3. Possible applications

One of the already mentioned applications is the design or assessment of new cement-based materials. The Enhanced Glasgow Model can be used in the initial testing process of the new material micro structure. This would lower the cost of the design process and eliminate possible flaws in the design. An example of such a procedure is the assessment of the addition of polypropylene fibres into the concrete mix, presented in Chapter 5.

Another possible application is a forensic investigation of fire damage of existing structural components, like beams, columns and slabs. An example of such an application is presented in Chapter 7. The same approach could also be used for entire structures, providing the simulation time could be speed-up, through parallel implementation of the code. Furthermore, the presented model proved to be able to estimate the moisture state of the specimens in both drying problem from Chapter 4 and in the concrete pressure vessel simulation from Chapter 7. Therefore, it is possible to investigate the moisture state in established structures.

Further application of the work presented in this thesis is the estimation of the transport processes at the location and close proximity of the deep geological high level waste (HLW) repositories. Deep geological disposal of high level waste would involve the excavation of tunnels or vaults at depths typically between 250 and 1,000 meters below ground in a suitable "host" rock (see e.g. Figure 8.1). In most concepts for deep geological disposal, the engineered waste package is surrounded at an appropriate time by a back-fill (which can be a cement-based grout or, in the case of disposal in salt, crushed salt) or a "buffer" material (is robust and a predicted state of concrete for all the presented typically a clay which swells on contact with water). The choice of the design and materials of the waste container and of the back-fill or buffer material is dependent upon the type of waste to
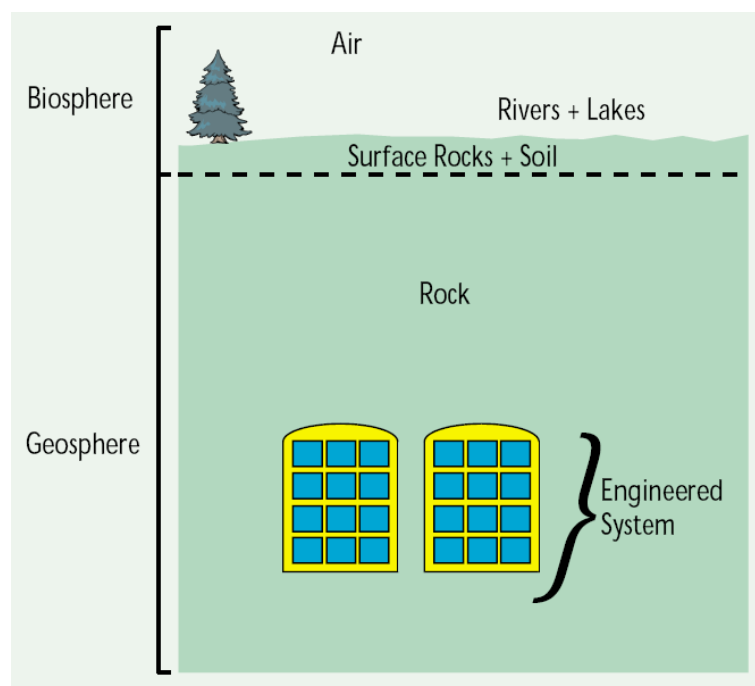
Figure 8.1.: Sketch of deep geological repository from [56]

be disposed of and, in some instances, the choice of host rock. Generally, it would be possible to investigate the behaviour of the heat, gas and moisture transport to provide the necessary information for design of proper HLW containers and establish the appropriate properties of back-fill. The adequate modifications to include soil constitutive models and adequate damage mechanisms would be vital. However, all the transport parts of the presented model are within the porous media mechanics, what provides all the necessary tools for such cases. Ultimately, the main aim would be to provide a good redistribution of heat away from HLW containers, without the transit of the polluting gases and radionuclide.

In summary, the presented Enhanced Glasgow Model is expected to be applicable in a wide variety of important applications, from the design of new fire resistant materials, the assessment of the fire damaged structural components, through to forensic investigation of entire structures.

A. Enhanced Glasgow Model formulation

Full set of equations for the Enhanced Glasgow model:

$$\mathbf{C}\dot{\mathbf{u}} - \bigtriangledown \cdot (\mathbf{K} \bigtriangledown \mathbf{u}) = 0$$

where the matrices $\mathbf{C}$ and $\mathbf{K}$ are presented in eq (**??**).

$$\mathbf{C} = \begin{pmatrix} 0 & 0 & 0 & 0 \\ 0 & C_{TT} & C_{TP} & C_{TV} \\ 0 & C_{AT} & C_{AP} & C_{AV} \\ 0 & C_{MT} & C_{MP} & C_{MV} \end{pmatrix}, \ \mathbf{K} = \begin{pmatrix} K_{aa} & K_{aT} & K_{aP} & K_{aV} \\ K_{Ta} & K_{TT} & K_{TP} & K_{TV} \\ K_{Pa} & K_{AT} & K_{AP} & K_{AV} \\ K_{Va} & K_{MT} & K_{MP} & K_{MV} \end{pmatrix}$$

$$K_{aa} = \int_V \boldsymbol{B}^T \left(\boldsymbol{E}_{sec} - H_1^{md} \left(1 - \chi \right) \hat{\boldsymbol{\sigma}}' \boldsymbol{s}^T \right) \boldsymbol{B} dV \qquad (\text{A.1})$$

$$\begin{aligned} K_{aT} &= -\int_V \boldsymbol{B}^T \left[\boldsymbol{E}_{sec}\boldsymbol{m} + \boldsymbol{E}_{sec}\boldsymbol{M}^- \boldsymbol{\sigma}'^- + (1 - \omega) H^{td}\hat{\boldsymbol{\sigma}}' + (1 - \chi) H_2^{md}\hat{\boldsymbol{\sigma}}' \right. \\ &- \left. (1 - \chi) H_1^{md}\hat{\boldsymbol{\sigma}}' \boldsymbol{s}^T \left(\boldsymbol{m} + \boldsymbol{M}^- \boldsymbol{\sigma}'^- \right) + \boldsymbol{p_T} \right] \boldsymbol{h}_T^T dV \qquad (\text{A.2}) \end{aligned}$$

$$K_{aP} = -\int_V \boldsymbol{B}^T \boldsymbol{p}_G \boldsymbol{h}_G^T dV \qquad (\text{A.3})$$

$$K_{aV} = -\int_V \boldsymbol{B}^T \boldsymbol{p}_V \boldsymbol{h}_{\rho_V}^T dV \qquad (\text{A.4})$$

$$K_{Ta} = \mathbf{0} \qquad (\text{A.5})$$

A. Enhanced Glasgow Model formulation

$$K_{Pa} = \mathbf{0} \tag{A.6}$$

$$K_{Va} = \mathbf{0} \tag{A.7}$$

$$
\begin{aligned}
K_{TT} = k - \lambda_E \varepsilon_L \rho_L \ & \left(\frac{S_B D_B}{S\phi} \left(\frac{\partial \varepsilon_L}{\partial T} - \frac{\varepsilon_L}{\phi} \frac{\partial \phi}{\partial T} \right) - \right. \\
& \left(1 - \frac{S_B}{S} \right) \frac{KK_L R_V \rho_L}{\mu_L} \left(\frac{T}{P_{Sat}} \frac{\partial P_{Sat}}{\partial T} - \right. \\
& \left. \left. \left(1 + \frac{T}{\rho_L} \frac{\partial \rho_L}{\partial T} \right) ln \left(\frac{\tilde{\rho}_V R_V T}{P_{Sat}} \right) - 1 \right) \right)
\end{aligned}
\tag{A.8}
$$

$$K_{TP} = -\lambda_E \left(1 - \frac{S_B}{S} \right) \varepsilon_L \rho_L \frac{KK_L}{\mu_L} \tag{A.9}$$

$$K_{TV} = -\lambda_E \varepsilon_L \rho_L \left(\frac{S_B D_B}{S\phi} \frac{\partial \varepsilon_L}{\partial \tilde{\rho}_V} + \left(1 - \frac{S_B}{S} \right) \frac{KK_L}{\mu_L} \frac{\rho_L R_V T}{\tilde{\rho}_V} \right) \tag{A.10}$$

$$K_{AT} = -\frac{\varepsilon_G D_{AV} \tilde{\rho}_V P_G}{\tilde{\rho}_G R_A T^2} \tag{A.11}$$

$$K_{AP} = \varepsilon_G \tilde{\rho}_A \frac{KK_G}{\mu_G} + \frac{\varepsilon_G D_{AV} \tilde{\rho}_V}{\tilde{\rho}_G R_V T} \tag{A.12}$$

$$K_{AV} = -\frac{\varepsilon_G D_{AV}}{\tilde{\rho}_G} \left(\tilde{\rho}_A + \tilde{\rho}_V \frac{R_V}{R_A} \right) \tag{A.13}$$

$$
\begin{aligned}
K_{MT} = \ & \frac{\varepsilon_G D_{AV} \tilde{\rho}_V P_G}{\tilde{\rho}_G R_A T^2} + \varepsilon_L \rho_L \left(\frac{S_B D_B}{S\phi} \left(\frac{\partial \varepsilon_L}{\partial T} - \frac{\varepsilon_L}{\phi} \frac{\partial \phi}{\partial T} \right) - \right. \\
& \left(1 - \frac{S_B}{S} \right) \frac{KK_L R_V \rho_L}{\mu_L} \left(\frac{T}{P_{Sat}} \frac{\partial P_{Sat}}{\partial T} - \right. \\
& \left. \left. \left(1 + \frac{T}{\rho_L} \frac{\partial \rho_L}{\partial T} \right) ln \left(\frac{\tilde{\rho}_V R_V T}{P_{Sat}} \right) - 1 \right) \right)
\end{aligned}
\tag{A.14}
$$

A. Enhanced Glasgow Model formulation

$$K_{MP} = \left(1 - \frac{S_B}{S}\right)\varepsilon_L \rho_L \frac{KK_L}{\mu_L} + \varepsilon_G \tilde{\rho}_V \frac{KK_G}{\mu_G} - \frac{\varepsilon_G D_{AV} \tilde{\rho}_V}{\tilde{\rho}_G R_A T^2} \qquad (A.15)$$

$$\begin{aligned} K_{MV} &= \frac{\varepsilon_G D_{AV}}{\tilde{\rho}_G}\left(\tilde{\rho}_A + \tilde{\rho}_V \frac{R_V}{R_A}\right) + \\ &+ \varepsilon_L \rho_L \left(\frac{S_B D_B}{S\phi}\frac{\partial \varepsilon_L}{\partial \tilde{\rho}_V} + \left(1 - \frac{S_B}{S}\right)\frac{KK_L}{\mu_L}\frac{\rho_L R_V T}{\tilde{\rho}_V}\right) \quad (A.16) \end{aligned}$$

$$C_{TT} = \rho C - \lambda_E \left(\frac{\partial \bar{\rho}_L}{\partial T}\right) + (\lambda_D + \lambda_E)\frac{\partial \bar{\rho}_D}{\partial T} \qquad (A.17)$$

$$C_{TP} = 0 \qquad (A.18)$$

$$C_{TV} = -\lambda_E \left(\frac{\partial \bar{\rho}_L}{\partial \tilde{\rho}_V}\right) \qquad (A.19)$$

$$C_{AT} = \tilde{\rho}_A \left(\frac{\partial \phi}{\partial T} - \frac{\partial \varepsilon_L}{\partial T}\right) - \left(\frac{\varepsilon_G P_G}{R_A T^2}\right) \qquad (A.20)$$

$$C_{AP} = \frac{\varepsilon_G}{R_A T^2} \qquad (A.21)$$

$$C_{AV} = \tilde{\rho}_A \frac{\partial \varepsilon_L}{\partial \tilde{\rho}_V} - \frac{\varepsilon_G R_V}{R_A} \qquad (A.22)$$

$$C_{MT} = \tilde{\rho}_V \left(\frac{\partial \phi}{\partial T} - \frac{\partial \varepsilon_L}{\partial T}\right) + \rho_L \left(\frac{\partial \varepsilon_D}{\partial T} - \frac{\partial \varepsilon_L}{\partial T}\right) + (\varepsilon_L - \varepsilon_D)\frac{\partial \rho_L}{\partial T} \quad (A.23)$$

$$C_{MP} = 0 \qquad (A.24)$$

$$C_{MV} = \varepsilon_G + (\rho_L - \tilde{\rho}_V)\frac{\partial \varepsilon_L}{\partial \tilde{\rho}_V} \qquad (A.25)$$

B. Full derivations for transport model

System of governing equations of transport part of the Enhanced Glasgow Model:

$$\frac{\partial \left(\varepsilon_G \widetilde{\rho}_A\right)}{\partial t} = -\nabla \cdot \mathbf{J}_A \tag{B.1}$$

$$\frac{\partial \left(\varepsilon_G \widetilde{\rho}_V\right)}{\partial t} + \frac{\partial \left(\varepsilon_L \rho_L\right)}{\partial t} - \frac{\partial \left(\varepsilon_D \rho_L\right)}{\partial t} = -\nabla \cdot \left(\mathbf{J}_{FW} + \mathbf{J}_V\right) \tag{B.2}$$

$$\begin{aligned}\left(\underline{\rho C}\right) \frac{\partial T}{\partial t} - \lambda_E \frac{\partial (\varepsilon_L \rho_L)}{\partial t} + \left(\lambda_D + \lambda_E\right) \frac{\partial (\varepsilon_D \rho_L)}{\partial t} &= \\ \nabla \cdot \left(k \nabla T\right) + \lambda_E \nabla \cdot \mathbf{J}_{FW} - \left(\underline{\rho C}\mathbf{v}\right) \cdot \nabla T& \end{aligned} \tag{B.3}$$

Finite element formulation - simplest notation:

$$\mathbf{C}\dot{\mathbf{u}} - \bigtriangledown \cdot \left(\mathbf{K} \bigtriangledown \mathbf{u}\right) = 0 \tag{B.4}$$

where

$$\mathbf{u}^T = (T, P_G, \tilde{\rho}_V) \tag{B.5}$$

There are six components which need to be simplified with respect to time and spatial derivatives for all three equations, to obtain $\mathbf{C}$ and $\mathbf{K}$. First, all the components connected with the gradients are calculated.

Water vapour flux :

B. Full derivations for transport model

$$-\mathbf{J}_V = \frac{KK_G}{\mu_G}\varepsilon_G\tilde{\rho}_V\partial P_G + \varepsilon_G\tilde{\rho}_G D_{VA}\frac{d}{d\mathbf{u}}\left(\frac{\tilde{\rho}_V}{\tilde{\rho}_G}\right) \tag{B.6}$$

$$\frac{d}{d\mathbf{u}}\left(\frac{\tilde{\rho}_V}{\tilde{\rho}_G}\right) = \frac{\frac{d\tilde{\rho}_V}{d\mathbf{u}}\tilde{\rho}_A - \tilde{\rho}_V\frac{d\tilde{\rho}_A}{d\mathbf{u}}}{(\tilde{\rho}_G)^2} \tag{B.7}$$

$$\begin{aligned}
\frac{d\tilde{\rho}_A}{d\mathbf{u}} &= \frac{d}{d\mathbf{u}}\frac{P_A}{R_A T} = \frac{d}{d\mathbf{u}}\frac{P_G - P_V}{R_A T} = \frac{d}{d\mathbf{u}}\left(\frac{P_G}{R_A T} - \frac{R_V}{R_A}\tilde{\rho}_V\right) = \\
&= \frac{T\partial P_G - P_G\partial T}{R_A T^2} - \frac{R_V}{R_A}\partial\tilde{\rho}_V
\end{aligned} \tag{B.8}$$

$$\begin{aligned}
\tilde{\rho}_G\frac{d}{d\mathbf{u}}\left(\frac{\tilde{\rho}_V}{\tilde{\rho}_G}\right) &= \tilde{\rho}_G\left(\frac{\frac{d\tilde{\rho}_V}{d\mathbf{u}}\tilde{\rho}_A - \tilde{\rho}_V\frac{d\tilde{\rho}_A}{d\mathbf{u}}}{(\tilde{\rho}_G)^2}\right) = \\
&= \frac{\tilde{\rho}_V P_G}{R_A T^2\tilde{\rho}_G}\partial T + \frac{\tilde{\rho}_V}{R_A T\tilde{\rho}_G}\partial P_G + \\
&+ \frac{\tilde{\rho}_A R_A + \tilde{\rho}_V R_V}{R_A\tilde{\rho}_G}\partial\tilde{\rho}_V
\end{aligned} \tag{B.9}$$

$$\begin{aligned}
-\mathbf{J}_V &= \frac{\varepsilon_G D_{VA}\tilde{\rho}_V P_G}{R_A T^2\tilde{\rho}_G}\partial T + \varepsilon_G\tilde{\rho}_V\left(\frac{KK_G}{\mu_G} - \frac{D_{VA}}{R_A T\tilde{\rho}_G}\right)\partial P_G + \\
&+ \frac{\varepsilon_G D_{VA}}{\tilde{\rho}_G}\left(\tilde{\rho}_A + \frac{\tilde{\rho}_V R_V}{R_A}\right)\partial\tilde{\rho}_V
\end{aligned} \tag{B.10}$$

$$-\mathbf{J}_V = K_{VT}\partial T + K_{VP}\partial P_G + K_{VV}\partial\tilde{\rho}_V \tag{B.11}$$

Air flux :

$$-\mathbf{J}_A = \frac{KK_G}{\mu_G}\varepsilon_G\tilde{\rho}_A dP_G + \varepsilon_G\tilde{\rho}_G D_{AV} d\left(\frac{\tilde{\rho}_A}{\tilde{\rho}_G}\right) \tag{B.12}$$

$$\frac{d}{d\mathbf{u}}\left(\frac{\tilde{\rho}_A}{\tilde{\rho}_G}\right) = \frac{\frac{d\tilde{\rho}_A}{d\mathbf{u}}\tilde{\rho}_G - \tilde{\rho}_A\frac{d\tilde{\rho}_G}{d\mathbf{u}}}{(\tilde{\rho}_G)^2} \tag{B.13}$$

$$\tilde{\rho}_A = \tilde{\rho}_G - \tilde{\rho}_V \tag{B.14}$$

155

$$\frac{d}{d\mathbf{u}}\left(\frac{\tilde{\rho}_A}{\tilde{\rho}_G}\right) = \frac{d}{d\mathbf{u}}\left(\frac{\tilde{\rho}_G - \tilde{\rho}_V}{\tilde{\rho}_G}\right) = \frac{\left(\frac{d\tilde{\rho}_V}{d\mathbf{u}}\tilde{\rho}_G + \tilde{\rho}_V\frac{d\tilde{\rho}_G}{d\mathbf{u}}\right)}{(\tilde{\rho}_G)^2} \qquad (B.15)$$

$$= \frac{\left(\frac{d\tilde{\rho}_V}{d\mathbf{u}}\tilde{\rho}_A - \tilde{\rho}_V\frac{d\tilde{\rho}_A}{d\mathbf{u}}\right)}{(\tilde{\rho}_G)^2}$$

$$= \frac{d}{d\mathbf{u}}\left(\frac{\tilde{\rho}_V}{\tilde{\rho}_G}\right)$$

$$\tilde{\rho}_G\frac{d}{d\mathbf{u}}\left(\frac{\tilde{\rho}_A}{\tilde{\rho}_G}\right) = \tilde{\rho}_G\frac{d}{d\mathbf{u}}\left(\frac{\tilde{\rho}_V}{\tilde{\rho}_G}\right) = -\left[\frac{\tilde{\rho}_V P_G}{R_A T^2 \tilde{\rho}_G}\partial T + \right. \qquad (B.16)$$

$$\left. -\frac{\tilde{\rho}_V T}{R_A T^2 \tilde{\rho}_G}\partial P_G + \frac{\tilde{\rho}_A R_A + \tilde{\rho}_V R_V}{R_A \tilde{\rho}_G}\partial\tilde{\rho}_V\right]$$

$$-\mathbf{J}_A = -\left(\frac{\varepsilon_G \tilde{\rho}_G D_{AV} P_G}{R_A T^2 \tilde{\rho}_G}\right)\partial T +$$

$$+\left(\frac{KK_G}{\mu_G}\varepsilon_G\tilde{\rho}_A + \frac{\varepsilon_G\tilde{\rho}_G D_{AV}}{R_A T\tilde{\rho}_G}\right)\partial P_G + \qquad (B.17)$$

$$-\frac{\varepsilon_G D_{AV}}{\tilde{\rho}_G}\left(\tilde{\rho}_A + \frac{\tilde{\rho}_V R_V}{R_A}\right)\partial\tilde{\rho}_V$$

$$-\mathbf{J}_A = K_{AT}\partial T + K_{AP}\partial P_G + K_{AV}\partial\tilde{\rho}_V \qquad (B.18)$$

Liquid water flux :

$$-\mathbf{J}_L = \left(1 - \frac{S_B}{S}\right)\frac{KK_L}{\mu_L}\varepsilon_L\rho_L\frac{dP_L}{d\mathbf{u}} + \left(\frac{S_B}{S}\right)\varepsilon_L\rho_L D_B\frac{dS_B}{d\mathbf{u}} \qquad (B.19)$$

$$P_L = P_G - P_C \qquad (B.20)$$

$$\frac{dP_L}{d\mathbf{u}} = \partial P_G + \frac{dP_C}{d\mathbf{u}} \qquad (B.21)$$

$$P_C = -R_V T\rho_L ln\left(\frac{P_V}{P_{Sat}}\right) \qquad (B.22)$$

B. Full derivations for transport model

$$P_V = R_V \tilde{\rho}_V T \tag{B.23}$$

$$P_C = -R_V T \rho_L ln \left(\frac{R_V \tilde{\rho}_V T}{P_{Sat}} \right) \tag{B.24}$$

$$\frac{\partial P_C}{\partial T} = R_V \rho_L \left[-\left(1 + \frac{T}{\rho_L} \frac{\partial \rho_L}{\partial T} \right) ln \left(\frac{R_V \tilde{\rho}_V T}{P_{Sat}} \right) - 1 + \frac{T}{P_{Sat}} \frac{\partial P_{Sat}}{\partial T} \right] \tag{B.25}$$

$$\frac{\partial P_C}{\partial \tilde{\rho}_V} = -R_V T \left(\frac{\rho_L}{\tilde{\rho}_V} \right) \tag{B.26}$$

$$S_B = \frac{\varepsilon_L}{\phi} \tag{B.27}$$

$$\frac{dS_B}{d\mathbf{u}} = \frac{\frac{d\varepsilon_L}{d\mathbf{u}} \phi - \varepsilon_L \frac{d\phi}{d\mathbf{u}}}{\phi^2} \tag{B.28}$$

$$\frac{d\varepsilon_L}{d\mathbf{u}} = \frac{\partial \varepsilon_L}{\partial \tilde{\rho}_V} \partial \tilde{\rho}_V + \frac{\partial \varepsilon_L}{\partial T} \partial T \tag{B.29}$$

$$\frac{d\phi}{d\mathbf{u}} = \frac{\partial \phi}{\partial T} \partial T \tag{B.30}$$

$$-\mathbf{J}_L = \left(1 - \frac{S_B}{S} \right) \frac{K K_L}{\mu_L} \varepsilon_L \rho_L \frac{d \left(P_G - P_C \right)}{d\mathbf{u}} + \left(\frac{S_B}{S} \right) \varepsilon_L \rho_L D_B \frac{dS_B}{d\mathbf{u}} \tag{B.31}$$

$$-\mathbf{J}_L = \varepsilon_L\rho_L\left(\frac{S_B D_B}{S\phi}\left(\frac{\partial\varepsilon_L}{\partial T} - \frac{\varepsilon_L}{\phi}\frac{\partial\phi}{\partial T}\right) + \right. \tag{B.32}$$

$$- \left(1 - \frac{S_B}{S}\right)\frac{KK_L R_V\rho_L}{\mu_L}\left(\frac{T}{P_{Sat}}\frac{\partial P_{Sat}}{\partial T} + \right.$$

$$- \left.\left(1 + \frac{T}{\rho_L}\frac{\partial\rho_L}{\partial T}\right)ln\left(\frac{\tilde{\rho}_V R_V T}{P_{Sat}}\right) - 1\right)\right)\partial T +$$

$$+ \left(1 - \frac{S_B}{S}\right)\varepsilon_L\rho_L\frac{KK_L}{\mu_L}\partial P_G +$$

$$+ \left.\varepsilon_L\rho_L\left(\frac{S_B D_B}{S\phi}\frac{\partial\varepsilon_L}{\partial\tilde{\rho}_V} + \left(1 - \frac{S_B}{S}\right)\frac{KK_L}{\mu_L}\frac{\rho_L R_V T}{\tilde{\rho}_V}\right)\partial\tilde{\rho}_V\right.$$

$$-\mathbf{J}_L = K_{LT}\partial T + K_{LP}\partial P_G + K_{LV}\partial\tilde{\rho}_V \tag{B.33}$$

Moisture flux - free water and water vapour combined :

$$-\left(\mathbf{J}_V + \mathbf{J}_L\right) = \left(K_{VT} + K_{LT}\right)\partial T + \left(K_{VP} + K_{LP}\right)\partial P_G + \left(K_{VV} + K_{LV}\right)\partial\tilde{\rho}_V$$
$$\tag{B.34}$$

$$-\left(\mathbf{J}_V + \mathbf{J}_L\right) = K_{MT}\partial T + K_{MP}\partial P_G + K_{MV}\partial\tilde{\rho}_V \tag{B.35}$$

Time derivatives :

1st equation

$$\frac{\partial\left(\varepsilon_G\tilde{\rho}_A\right)}{\partial t} \Rightarrow \tag{B.36}$$

$$\frac{\partial\left(\varepsilon_G\tilde{\rho}_A\right)}{\partial t} = \frac{\partial\left(\varepsilon_G\right)}{\partial t}\tilde{\rho}_A + \varepsilon_G\frac{\partial\left(\tilde{\rho}_A\right)}{\partial t} \tag{B.37}$$

$$\tilde{\rho}_A = \frac{P_G}{R_A T} + \frac{R_V}{R_A}\tilde{\rho}_V \tag{B.38}$$

$$\frac{\partial\left(\tilde{\rho}_A\right)}{\partial t} = \frac{-P_G}{R_A T^2}\frac{\partial T}{\partial t} + \frac{1}{R_A T}\frac{\partial P_G}{\partial t} - \frac{R_V}{R_A}\frac{\partial\tilde{\rho}_V}{\partial t} \tag{B.39}$$

$$\varepsilon_G = \phi - \varepsilon_L \tag{B.40}$$

$$\frac{\partial \left(\varepsilon_G\right)}{\partial t} = \frac{\partial T}{\partial t}\left(\frac{\partial \varepsilon_G}{\partial T}\right) + \frac{\partial \widetilde{\rho}_V}{\partial t}\left(\frac{\partial \varepsilon_G}{\partial \widetilde{\rho}_V}\right) \tag{B.41}$$

$$\frac{\partial \varepsilon_G}{\partial T} = \frac{\partial \phi}{\partial T} + \frac{\partial \varepsilon_L}{\partial T} \tag{B.42}$$

$$\frac{\partial \varepsilon_G}{\partial \widetilde{\rho}_V} = \frac{\partial \varepsilon_L}{\partial \widetilde{\rho}_V} \tag{B.43}$$

$$\frac{\partial \left(\varepsilon_G\widetilde{\rho}_A\right)}{\partial t} = \left(\tilde{\rho}_A\left(\frac{\partial \phi}{\partial T} - \frac{\partial \varepsilon_L}{\partial T}\right) - \left(\frac{\varepsilon_G P_G}{R_A T^2}\right)\right)\frac{\partial T}{\partial t} + \tag{B.44}$$
$$+ \left(\frac{\varepsilon_G}{R_A T^2}\right)\frac{\partial P_G}{\partial t} + \left(\tilde{\rho}_A\frac{\partial \varepsilon_L}{\partial \tilde{\rho}_V} - \frac{\varepsilon_G R_V}{R_A}\right)\frac{\partial \widetilde{\rho}_V}{\partial t}$$

$$\frac{\partial \left(\varepsilon_G\widetilde{\rho}_A\right)}{\partial t} = C_{AT}\frac{\partial T}{\partial t} + C_{AP}\frac{\partial P_G}{\partial t} + C_{AV}\frac{\partial \widetilde{\rho}_V}{\partial t} \tag{B.45}$$

2nd equation

$$\frac{\partial \left(\varepsilon_G\widetilde{\rho}_V\right)}{\partial t} + \frac{\partial \left(\varepsilon_L\rho_L\right)}{\partial t} - \frac{\partial \left(\varepsilon_D\rho_L\right)}{\partial t} \Rightarrow \tag{B.46}$$

$$\frac{\partial \left(\varepsilon_G\widetilde{\rho}_V\right)}{\partial t} = \frac{\partial \varepsilon_G}{\partial t}\widetilde{\rho}_V + \varepsilon_G\frac{\partial \widetilde{\rho}_V}{\partial t} \tag{B.47}$$

$$\frac{\partial \left(\varepsilon_L\rho_L\right)}{\partial t} = \left(\frac{\partial \left(\varepsilon_L\right)}{\partial T}\rho_L + \varepsilon_L\frac{\partial \left(\rho_L\right)}{\partial T}\right)\frac{\partial T}{\partial t} + \rho_L\frac{\partial \left(\varepsilon_L\right)}{\partial \widetilde{\rho}_V}\frac{\partial \widetilde{\rho}_V}{\partial t} \tag{B.48}$$

$$\frac{\partial \left(\varepsilon_D\rho_L\right)}{\partial t} = \frac{\partial \left(\varepsilon_D\rho_L\right)}{\partial T}\frac{\partial T}{\partial t} \tag{B.49}$$

$$\frac{\partial\left(\varepsilon_G\widetilde{\rho}_V\right)}{\partial t} + \frac{\partial\left(\varepsilon_L\rho_L\right)}{\partial t} \quad + \tag{B.50}$$

$$-\frac{\partial\left(\varepsilon_D\rho_L\right)}{\partial t} \;=\; \left(\widetilde{\rho}_V\left(\frac{\partial\phi}{\partial T} - \frac{\partial\varepsilon_L}{\partial T}\right) +\right.$$

$$+\;\; \rho_L\left(\frac{\partial\varepsilon_D}{\partial T} - \frac{\partial\varepsilon_L}{\partial T}\right) + \left(\varepsilon_L - \varepsilon_D\right)\frac{\partial\rho_L}{\partial T}\right)\frac{\partial T}{\partial t}$$

$$+\;\; (0)\frac{\partial P_G}{\partial t} + \left(\varepsilon_G + \left(\rho_L - \widetilde{\rho}_V\right)\frac{\partial\varepsilon_L}{\partial\widetilde{\rho}_V}\right)\frac{\partial\widetilde{\rho}_V}{\partial t}$$

$$\frac{\partial\left(\varepsilon_G\widetilde{\rho}_A\right)}{\partial t} + \frac{\partial\left(\varepsilon_L\rho_L\right)}{\partial t} - \frac{\partial\left(\varepsilon_D\rho_L\right)}{\partial t} = C_{MT}\frac{\partial T}{\partial t} + C_{MP}\frac{\partial P_G}{\partial t} + C_{MV}\frac{\partial\widetilde{\rho}_V}{\partial t} \tag{B.51}$$

3rd equation

$$\left(\underline{\rho C}\right)\frac{\partial T}{\partial t} - \lambda_E\frac{\partial\left(\varepsilon_L\rho_L\right)}{\partial t} + \left(\lambda_D + \lambda_E\right)\frac{\partial\left(\varepsilon_D\rho_L\right)}{\partial t} \Rightarrow \tag{B.52}$$

$$\left(\underline{\rho C}\right)\frac{\partial T}{\partial t} - \lambda_E\frac{\partial\left(\varepsilon_L\rho_L\right)}{\partial t} \quad + \tag{B.53}$$

$$+\left(\lambda_D + \lambda_E\right)\frac{\partial\left(\varepsilon_D\rho_L\right)}{\partial t} \;=\; \left(\rho C - \lambda_E\left(\frac{\partial\bar{\rho}_L}{\partial T}\right) + \left(\lambda_D + \lambda_E\right)\frac{\partial\bar{\rho}_D}{\partial T}\right)\frac{\partial T}{\partial t} +$$

$$+\;\; (0)\frac{\partial P_G}{\partial t} + \left(-\lambda_E\left(\frac{\partial\bar{\rho}_L}{\partial\widetilde{\rho}_V}\right)\right)\frac{\partial\widetilde{\rho}_V}{\partial t}$$

$$\left(\underline{\rho C}\right)\frac{\partial T}{\partial t} - \lambda_E\frac{\partial\left(\varepsilon_L\rho_L\right)}{\partial t} + \left(\lambda_D + \lambda_E\right)\frac{\partial\left(\varepsilon_D\rho_L\right)}{\partial t} = C_{TT}\frac{\partial T}{\partial t} + C_{TP}\frac{\partial P_G}{\partial t} + C_{TV}\frac{\partial\widetilde{\rho}_V}{\partial t}$$
$$\tag{B.54}$$

Final form

$$\mathbf{C\dot{u}} - \bigtriangledown\left(\mathbf{K}\bigtriangledown\mathbf{u}\right) = 0 \tag{B.55}$$

where the matrices $\mathbf{C}$ and $\mathbf{K}$ are presented in Appendix A.

C. Numerical formulation

$$\bar{\mathbf{K}} \triangle \mathbf{u} = \mathbf{R} \tag{C.1}$$

$$\bar{\mathbf{K}}_{i-1} \triangle \mathbf{a} = \mathbf{f}_{ext} - \mathbf{f}_{int,i-1} \tag{C.2}$$

$$
\begin{aligned}
\bar{\mathbf{K}} &= \begin{pmatrix} \mathbf{K_{TT}} & \mathbf{K_{TP}} & \mathbf{K_{TV}} \\ \mathbf{K_{AT}} & \mathbf{K_{AP}} & \mathbf{K_{AV}} \\ \mathbf{K_{MT}} & \mathbf{K_{MP}} & \mathbf{K_{MV}} \end{pmatrix} = \\
&= \int_U \left(\frac{1}{\triangle t} \mathbf{N}^T \mathbf{C} \mathbf{N} + \alpha\left(t\right) \cdot \bigtriangledown^T \mathbf{N} \left(\mathbf{K} \bigtriangledown \left(\mathbf{N} \right) \right) \right) dV
\end{aligned} \tag{C.3}
$$

where sub-matrices are defined as:

$$\mathbf{K}_{TT} = \int_U \left(\frac{1}{\triangle t} h_T C_{TT} h_T + \alpha\left(t\right) \bigtriangledown^T h_T \left(\boldsymbol{K_{TT}} \bigtriangledown \left(h_T \right) \right) \right) dV \tag{C.4}$$

$$\mathbf{K}_{TP} = \int_U \left(\frac{1}{\triangle t} h_T C_{TP} h_T + \alpha\left(t\right) \bigtriangledown^T h_T \left(\boldsymbol{K_{TP}} \bigtriangledown \left(h_T \right) \right) \right) dV \tag{C.5}$$

$$\mathbf{K}_{TV} = \int_U \left(\frac{1}{\triangle t} h_T C_{TV} h_T + \alpha\left(t\right) \bigtriangledown^T h_T \left(\boldsymbol{K_{TV}} \bigtriangledown \left(h_T \right) \right) \right) dV \tag{C.6}$$

$$\mathbf{K}_{AT} = \int_U \left(\frac{1}{\triangle t} h_P C_{AT} h_P + \alpha\left(t\right) \bigtriangledown^T h_P \left(\boldsymbol{K_{AT}} \bigtriangledown \left(h_P \right) \right) \right) dV \tag{C.7}$$

$$\mathbf{K}_{AP} = \int_U \left(\frac{1}{\triangle t} h_P C_{AP} h_P + \alpha\left(t\right) \bigtriangledown^T h_P \left(\boldsymbol{K_{AP}} \bigtriangledown \left(h_P\right)\right) \right) dV \qquad \text{(C.8)}$$

$$\mathbf{K}_{AV} = \int_U \left(\frac{1}{\triangle t} h_P C_{AV} h_P + \alpha\left(t\right) \bigtriangledown^T h_P \left(\boldsymbol{K_{AV}} \bigtriangledown \left(h_P\right)\right) \right) dV \qquad \text{(C.9)}$$

$$\mathbf{K}_{MT} = \int_U \left(\frac{1}{\triangle t} h_{\rho_V} C_{MT} h_{\rho_V} + \alpha\left(t\right) \bigtriangledown^T h_{\rho_V} \left(\boldsymbol{K_{MT}} \bigtriangledown \left(h_{\rho_V}\right)\right) \right) dV \quad \text{(C.10)}$$

$$\mathbf{K}_{MP} = \int_U \left(\frac{1}{\triangle t} h_{\rho_V} C_{MP} h_{\rho_V} + \alpha\left(t\right) \bigtriangledown^T h_{\rho_V} \left(\boldsymbol{K_{MP}} \bigtriangledown \left(h_{\rho_V}\right)\right) \right) dV \quad \text{(C.11)}$$

$$\mathbf{K}_{MV} = \int_U \left(\frac{1}{\triangle t} h_{\rho_V} C_{MV} h_{\rho_V} + \alpha\left(t\right) \bigtriangledown^T h_{\rho_V} \left(\boldsymbol{K_{MV}} \bigtriangledown \left(h_{\rho_V}\right)\right) \right) dV \quad \text{(C.12)}$$

$$\mathbf{R} = \begin{pmatrix} f_{Text} - f_{Tint} \\ f_{Aext} - f_{Aint} \\ f_{Mext} - f_{Mint} \end{pmatrix} \qquad \text{(C.13)}$$

where the force vectors are defined as:

$$
\begin{aligned}
f_{Text} \;=\;& \int_{\partial U} h_T K_{TT} \left(\frac{d}{dn} T \right) dS + \int_{\partial U} h_T K_{TP} \left(\frac{d}{dn} P_G \right) dS + \\
& \int_{\partial U} h_T K_{TV} \left(\frac{d}{dn} \tilde{\rho}_V \right) dS
\end{aligned} \qquad \text{(C.14)}
$$

$$
\begin{aligned}
f_{Aext} \;=\;& \int_{\partial U} h_P K_{AT} \left(\frac{d}{dn} T \right) dS + \int_{\partial U} h_P K_{AP} \left(\frac{d}{dn} P_G \right) dS + \\
& \int_{\partial U} h_P K_{AV} \left(\frac{d}{dn} \tilde{\rho}_V \right) dS
\end{aligned} \qquad \text{(C.15)}
$$

$$
\begin{aligned}
f_{Mext} \;=\; & \int_{\partial U} h_{\rho_V} K_{MT} \left(\frac{d}{dn} T \right) dS + \int_{\partial U} h_{\rho_V} K_{MP} \left(\frac{d}{dn} P_G \right) dS + \\
& \int_{\partial U} h_{\rho_V} K_{MV} \left(\frac{d}{dn} \tilde{\rho}_V \right) dS
\end{aligned}
\tag{C.16}
$$

$$
f_{Tint} = \int_U h_T C_{TT} \frac{d}{dt} \mathbf{u}_i^{k-1} dV + \int_U \triangledown h_T \left(K_{TT} \triangledown \left(\mathbf{u}\left(\mathbf{t}\right)_{k-1} \right) \right) dV
\tag{C.17}
$$

$$
f_{Aint} = \int_U h_P C_{AP} \frac{d}{dt} \mathbf{u}_i^{k-1} dV + \int_U \triangledown h_P \left(K_{AP} \triangledown \left(\mathbf{u}\left(\mathbf{t}\right)_{k-1} \right) \right) dV
\tag{C.18}
$$

$$
f_{Mint} = \int_U h_{\rho_V} C_{MV} \frac{d}{dt} \mathbf{u}_i^{k-1} dV + \int_U \triangledown h_{\rho_V} \left(K_{MV} \triangledown \left(\mathbf{u}\left(\mathbf{t}\right)_{k-1} \right) \right) dV
\tag{C.19}
$$

D. Additional physics and thermodynamic properties

State equation of liquid water. A relationship that is used for a state equation of water in the model is a nonlinear empirically based expression, which was introduced by Furbish [21]. This relationship is presented in equation (D.1) and in figure D.1. It can be easily see that water density decreases with the rise in temperature and that a thermal expansion happens around the critical point of water.

$$
\begin{aligned}
\rho_w &= (p_{wl} - p_{wr}) \left(a_0 + a_1 T_C + a_2 T_C^2 + a_3 T_C^3 + a_4 T_C^4 + a_5 T_C^5 \right) \\
&+ \left(b_0 + b_1 T_C + b_2 T_C^2 + b_3 T_C^3 + b_4 T_C^4 + b_5 T_C^5 \right) \left[\frac{\text{kg}}{\text{m}^3} \right] \qquad \text{(D.1)}
\end{aligned}
$$

where $p_{wl} = 1e + 7$ Pa and $p_{wr} = 2e + 7$ Pa are the characteristic liquid pressures and the coefficients a_i and b_i are shown in table D.1.

Saturation Vapour Pressure. The water vapour in moist air is assumed to have the same composition as naturally occurring liquid water. The saturation pressure of vapour over liquid water used in the model is based on the work of Hyland and Wexler [30]. It was obtained by the integration of the Clausius-Clapeyron equation (D.2) and data fitting to yield an equation

a_0	a_1	a_2	a_3	a_4	a_5
4.8863e-7	-1.6528e-9	1.8621e-12	2.4266e-13	-1.5996e-15	3.3703e-18

b_0	b_1	b_2	b_3	b_4	b_5
1.0213e+3	-7.7377e-1	8.7696e-3	-9.2118e-5	3.3534e-7	-4.4034e-10

Table D.1.: Furbish coefficients a_i and b_i.
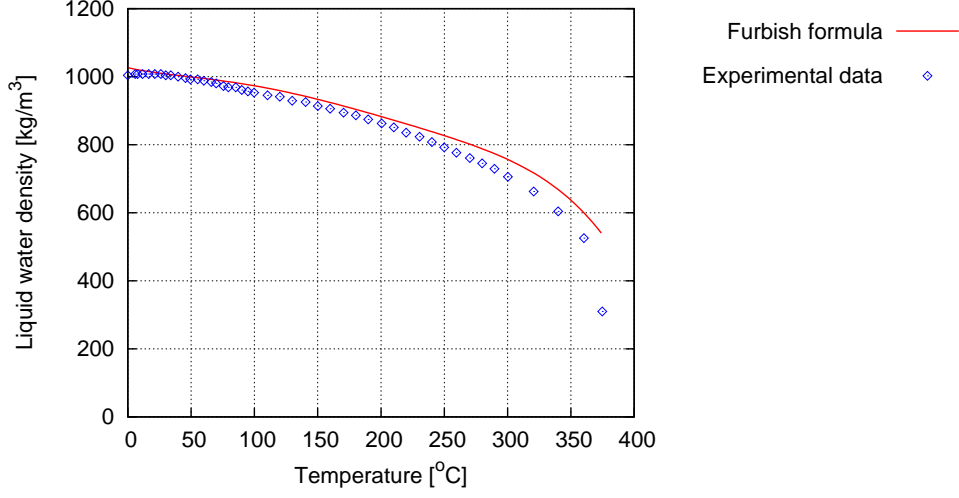
Figure D.1.: Water density by Furbish [21], comparison between experimental results and the formulation.

c_0	c_1	c_2	c_3
-0.56745359e+3	0.63925247e+1	-0.96778430e-2	0.62215701e-6

c_4	c_5	c_6
0.20747825e-8	-0.94840240e-12	0.41635019e+1

Table D.2.: Hyland-Wexler coefficients

implicit on P_{Sat}. A formulation for the saturation vapour pressure over liquid water is given by (D.3).

$$\frac{dp}{dT} = \frac{\Delta h}{T \Delta v} \qquad (D.2)$$

$$P_{Sat} = \frac{c_0}{T} + c_1 + c_2 T + c_3 T^2 + c_4 T^3 + c_5 T^4 + c_6 log\,(T)\ [\text{MPa}] \qquad (D.3)$$

where the coefficients c_i are shown in equation Table D.2 on page 165.

Porosity. The changes of porosity with increase of the temperature can be represented as a simple function presented in equation D.5 following [65]. This simplified approach allows porosity to increase 3 times its initial value.

a	b	c	d
-0.11661807e-8	0.15743440e-1	-0.27988338e-2	1.13411079
e	f	g	h
-0.23234008e-3	0.23345607e-5	-0.16798756e-8	1.00156306

Table D.3.: Porosity coefficients

$$\phi = \phi_0 \begin{cases} 1 & \text{for } T_C \leq 100^oC \\ aT_C^3 + bT_C^2 + cT_C + d & \text{for } 100^oC < T_C \leq 800^oC \\ 3 & \text{for } T_C > 800^oC \end{cases} \qquad \text{(D.4)}$$

where ϕ_0 is an initial porosity and a, b, c and d are coefficients of a cubic functions such that $\phi(T)$ and its derivative are continuous (presented in table D.3).

Alternatively, a function of porosity has been derived by the author based on experimental results presented by Bazant [7]. In this approach, a presented porosity function ((D.5)) is allowing porosity to increase only by 50%. However, when the temperature is reaching its high levels of above 1000°C, the porosity is being reduced almost to the initial level by 1250°C.

$$\phi = \phi_0 \begin{cases} 1 & \text{for } T_C \leq 100^oC \\ eT_C^3 + fT_C^2 + gT_C + h & \text{for } 100^oC < T_C \leq 1250^oC \\ eT_{C\infty}^3 + fT_{C\infty}^2 + gT_{C\infty} + h & \text{for } T_C > 1250^oC \end{cases} \qquad \text{(D.5)}$$

where e, f, g and h are coefficients of a cubic functions (presented in table D.3) and $T_{C\infty}$ is a temperature of 1250°C.

D. Additional physics and thermodynamic properties

Mass of dehydrated water [65].

$$\varepsilon_D \rho_L = \begin{cases} 0 & \text{for } T_C \leq 200^o C \\ 7e-4 \, (T_C - 200) & \text{for } 200^o C < T_C \leq 300^o C \\ 4e-5 \, (T_C - 200) + 0.07 & \text{for } 300^o C < T_C \leq 800^o C \\ 0.09 & \text{for } T_C > 800^o C \end{cases} \quad \left[\frac{\text{kg}}{\text{m}^3}\right]$$

$$(D.6)$$

Diffusivity of Gas [11]. The effective diffusion coefficient (D.7) of water vapour in air, or air in water vapour varies with temperature and gas pressure. The proper diffusion for concrete can be achieved through reduction in the rate of it caused by the complex pore structure, what can be seen in equation (D.8).

$$D = 1.87e - 5 \left(\frac{T^{2.072}}{P_G}\right) \; \left[\frac{\text{m}^2}{\text{s}}\right] \tag{D.7}$$

$$D_{AV} = D_{VA} = D\frac{\delta}{\tau^2} \; \left[\frac{\text{m}^2}{\text{s}}\right] \tag{D.8}$$

where $\delta = 0.5$ is a constrictivity and $\tau = 3$ is a tortuosity.

Dynamic Viscosity is a measure of the resistance of a fluid to deform under shear stress or more simple to flow. All the equations provided in this subsection were reported by [22] and fit well with the tabulated data refereed by [11]. All the temperatures in this equations are in degrees Kelvin.

- Dynamic Viscosity of Liquid Water

$$\mu_L = 0.6612 \, (T - 229)^{-1.562} \; \left[\frac{Ns}{m^2}\right] \text{ for } T \leq T_{Crit} \tag{D.9}$$

where $T_{Crit} = 647.3$ K is the critical point of water.

- Dynamic Viscosity of Water Vapour

$$\mu_V = \mu_V^0 + \alpha_V \, (T - T_0) \; \left[\frac{Ns}{m^2}\right] \tag{D.10}$$

D. Additional physics and thermodynamic properties

where $\mu_V^0 = 8.85e-6$ Pa s, $\alpha_V = 3.53e-8$ Pa s K^{-1} and $T_0 = 273.15$ K.

- Dynamic Viscosity of Dry Air

$$\mu_A = \mu_A^0 + \alpha_V\,(T-T_0) - \beta_V\,(T-T_0)^2 \quad \left[\frac{Ns}{m^2}\right] \tag{D.11}$$

where $\mu_A^0 = 17.17e-6$ Pa s, $\alpha_A = 4.73e-8$ Pa s K^{-1} and $\beta_A = 2.22e-11$ Pa s K^{-2}.

- Dynamic Viscosity of mixture of Gases

$$\mu_G = \begin{cases} \frac{\tilde{\rho}_A\mu_A+\tilde{\rho}_V\mu_V}{\tilde{\rho}_A+\tilde{\rho}_V} & \text{for } (\tilde{\rho}_A+\tilde{\rho}_V) > 0 \\ 0 & \text{for } (\tilde{\rho}_A+\tilde{\rho}_V) = 0 \end{cases} \quad \left[\frac{Ns}{m^2}\right] \tag{D.12}$$

Effective Heat Capacity of partially saturated concrete can be expressed as a combination of the thermal capacities of its constituents, it is presented in equation (D.13). Heat capacity is mathematically defined as the ratio of a small increment of energy ∂Q, to the corresponding small increase in its temperature dT.

$$\underline{\rho C} = \varepsilon_S\rho_S C_S + \varepsilon_L\rho_L C_L + \varepsilon_G\tilde{\rho}_V C_V + \varepsilon_G\tilde{\rho}_A C_A \quad \left[\frac{\text{J}}{\text{m}^3\text{K}}\right] \tag{D.13}$$

where $\varepsilon_S\rho_S$ is the solid skeleton content per unit volume of concrete and C_i is the specific heat of the phase i.

Specific Heat is the amount of heat per unit mass required to raise the temperature by one degree Celsius.

- Specific Heat of Liquid Water

$$C_L = \begin{cases} (2.4768T + 3368.2) + \left(\frac{aT}{513.15}\right)^b & \text{for } T \leq T_{Crit} \\ 24515.0 & \text{for } T > T_{Crit} \end{cases} \quad \left[\frac{\text{J}}{\text{kgK}}\right] \tag{D.14}$$

where $a = 1.08542631988638$ and $b = 31.4447657616636$.

D. Additional physics and thermodynamic properties

- Specific Heat of Water Vapour

$$C_V = \begin{cases} (7.1399T + 443) + \left(\frac{aT}{513.15}\right)^b & \text{for } T \leq T_{Crit} \\ 45821.04 & \text{for } T > T_{Crit} \end{cases} \left[\frac{\text{J}}{\text{kgK}}\right] \quad \text{(D.15)}$$

where $a = 1.13771502228162$ and $b = 29.4435287521143$.

- Specific Heat of Dry Air

$$C_A = aT^3 + bT^2 + cT + d \ \left[\frac{\text{J}}{\text{kgK}}\right] \quad \text{(D.16)}$$

where $a = -9.84936701814735e - 8$, $b = 3.56436257769861e - 4$, $c = -1.21617923987757e - 1$ and $d = 1.01250255216324e + 3$.

- Latent Heat of Solid Skeleton

$$C_S = 811 + 80 \left(\frac{T_C}{120}\right) - 4 \left(\frac{T_C}{120}\right)^2 \left[\frac{\text{J}}{\text{kgK}}\right] \quad \text{(D.17)}$$

Specific enthalpies

- Evaporation and desorption

$$\lambda_E = 2.672e + 5 \left(T_{Crit} - T\right)^{0.38} \left[\frac{J}{kg}\right] \quad \text{(D.18)}$$

- Dehydration of chemically bound water, kept at constant value

$$\lambda_D = 2400e + 3 \left[\frac{J}{kg}\right] \quad \text{(D.19)}$$

Transfer Coefficient

- Radiative Heat Transfer Coefficient

$$h_r = e\sigma \left(T^2 + T_\infty^2\right)\left(T + T_\infty\right) \left[\frac{\text{W}}{\text{m}^2\text{K}}\right] \quad \text{(D.20)}$$

where e is the emissivity of the concrete surface and $\sigma = 5.67e - 8 \left[\text{W/m}^2\text{K}^4\right]$ is a Stefan-Boltzmann constant.

D. Additional physics and thermodynamic properties

- Convective Heat Transfer Coefficient, h_q, is kept as a constant value and it depends on the problem.

- Combined Heat Transfer Coefficient

$$h_{qr} = h_r + h_q \quad \left[\frac{\text{W}}{\text{m}^2\text{K}} \right] \tag{D.21}$$

Thermal Conductivity   as a function of temperature is difficult to measure experimentally. There is almost no or limited testing standards and on top of that very often the moisture conditions are neglected during such tests and afterwards, information on type and amount of aggregate are not fully provided. Furthermore the apparatus used and the methods themselves are considered to be not enough accurate.

There are some well known and established functions, like Anderberg (1978)(D.22). It was published in CIB bulletins and used in Swedish codes for fire engineering design. The function provided (D.22) is for normal strength concrete with siliceous aggregate.

$$k_{eff} = 1.68 - 0.19055 \left(\frac{T}{100} \right) + 0.0082 \left(\frac{T}{100} \right)^2 \left[\frac{\text{W}}{\text{Km}} \right] \tag{D.22}$$

For engineering practise, in Eurocode 2 [1] and 4 a thermal conductivity limits has been proposed and an adequate function can be chosen within lower(D.23) and upper band(D.24). The recommendations for the UK are introduced in the National Annex, where thermal conductivity for normal strength concrete should coincide with lower limit defined by (D.23) and for high strength concrete by upper limit defined by (D.24).

$$k_{eff} = 1.36 - 0.136 \left(\frac{T}{100} \right) + 0.0057 \left(\frac{T}{100} \right)^2 \left[\frac{\text{W}}{\text{Km}} \right] \tag{D.23}$$

$$k_{eff} = 2 - 0.2451 \left(\frac{T}{100} \right) + 0.0107 \left(\frac{T}{100} \right)^2 \left[\frac{\text{W}}{\text{Km}} \right] \tag{D.24}$$

Both of the above approaches are within the temperature range of (20 - $1200^o C$).

Recently, a studies on thermal parameters of high strength concrete had been conducted by Kodur and Sultan [43]. They presented a thermal
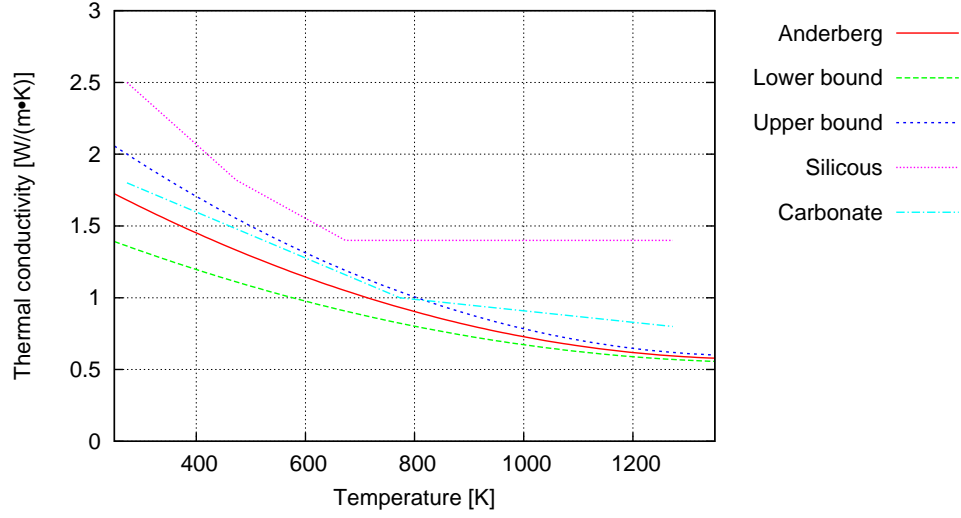
Figure D.2.: Comparison of thermal conductivity functions.

conductivity functions for this type of concrete with two different types of aggregates, siliceous one(D.25) and carbonate one(D.26).

$$
k_{eff} =
$$

$$
\begin{aligned}
2.5 - 0.0034T & \quad \text{for } 0 < T \leq 200^oC \\
2.24 - 0.0021T & \quad \text{for } 200 < T \leq 400^oC \\
1.4 & \quad \text{for } 400 < T \leq 1000^oC
\end{aligned}
\qquad (D.25)
$$

$$
k_{eff} =
$$

$$
\begin{aligned}
1.8 - 0.0016T & \quad \text{for } 0 < T \leq 500^oC \\
1.2 - 0.0004T & \quad \text{for } 500 < T \leq 1000^oC
\end{aligned}
\qquad (D.26)
$$

The comparison of the functions is presented in Figure D.2, where it can be easily seen that Anderberg function coincide with a lower limit provided by Euro-code. The function for high strength concrete with siliceous aggregate seems to be overestimating the values. The function for carbonate aggregate is coinciding with upper limit up to 600 degrees, from then it starts to be the lower function from the presented.

Bibliography

[1] Bs en 1992-1-2:2004 eurocode 2: Design of concrete structures - part 1-2: General rules - structural fire design.

[2] P. B. Bamforth. Relationship between permeability coefficients for concrete obtained using liquid and gas. *Magazine of Concrete Research*, 39(138):3–11, 1987.

[3] V. Baroghel-Bouny, M. Mainguy, T. Lassabatere, and O. Coussy. Characterization and identification of equilibrium and transfer moisture properties for ordinary and high-performance cementitious materials. *Cement and Concrete Research*, 29(8):1225–1238, 1999.

[4] B. Bary. Etude de couplage hydraulique - mechanique dans le beton endomage. *Laboratoire de Mecanique et Technologie, Cachan*, 11, 1996.

[5] Z. P. Bazant. Analysis of pore pressure, thermal stress and fracture in rapidly heated concrete. In *Proc. of Int. Workshop on Fire Performance of High-Strength Concrete*, Gaitherburg, MD, USA, February 13-14 1997.

[6] Z. P. Bazant. Concrete creep at high temperature and its interaction with fracture: recent progress. In G. Pijaudier-Cabot, B. Gerard, and P. Acker, editors, *Proceedings of the 7th International Conference on Creep, Shrinkage and Durability of Concrete and Concrete Structures*, pages 449–460. Hermes Science, 2005.

[7] Z.P. Bazant and M.F. Kaplan. *Concrete at High Temperatures: Material properties and mathematical models*. Longman, 1996.

[8] J. Bear. *Dynamics of fluids in porous media*. Environmental Science Series. American Elsevier, 1972.

Bibliography

[9] J. Bear and Y. Bachmat. *Introduction to Modelling of Transport Phenomena in Porous Media.* Kluwer Academic Publisher, 1990.

[10] A.V. Bishop. The principle of effective stress. *Teknisk Ukeblad*, 39:859–863, 1959.

[11] Y. A. Cengel. *Heat Transfer: A Practical Approach.* McGraw-Hill, New York, 2nd edition, 2003.

[12] J. H. Chung and G. R. Consolazio. Numerical modelling of transport phenomena in reinforced concrete exposed to elevated temperatures. *Cement and Concrete Research*, 35(3):597–608, 2005.

[13] O. Coussy. *Mechanics of Porous Continua,.* Wiley, 1995.

[14] C. T. Davie, C. J. Pearce, and N. Bicanic. Effect of fluid transport on the structural integrity of concrete nuclear pressure vessels. *Proceedings of 13th Annual Conference of the Association for Computational Mechanics in Engineering - UK*, 2005.

[15] C. T. Davie, C. J. Pearce, and N. Bicanic. Coupled heat and moisture transport in concrete at elevated temperatures - effect of capillary pressure and adsorbed water. *Numerical Heat Transfer, Part A*, 49(8):733–763, 2006.

[16] R. de Borst and P. P. J. M. Peeters. Analysis of concrete structures under thermal loading. *Computer Methods In Applied Mechanics And Engineering*, 77(3):293–310, December 1989.

[17] R. K. Dhir, P. C. Hewlett, and Y. N. Chan. Near surface characteristics of concrete: intrinsic permeability. *Magazine of Concrete Research*, 41(147):87–97, 1989.

[18] M.B. Dwaikat and V.K.R. Kodur. Hydro thermal model for predicting fire-induced spalling in concrete structural systems. *Fire Safety Journal*, 44:425–434, 2009.

[19] R. Felicetti and P.G. Gambarova. Heat in concrete: Special issues in materials testing. *Studies and Researches, Politechnico di Milano*, 24:121–38, 2003.

Bibliography

[20] F. Feyel. A multilevel finite element method (fe) to describe the response of highly non-linear structures using generalized continua. *Computer Methods in Applied Mechanics and Engineering*, 192:3233–3244, 2003.

[21] D. J. Furbish. *Fluid Physics in Geology. An introduction to fluid motion on earth surface and within its crust.* Oxford University Press, 1997.

[22] D. Gawin, C. E. Majorana, and B. A. Schrefler. Numerical analysis of hygro-thermal behaviour and damage of concrete at high temperature. *Mechanics of Cohesive-Frictional Materials*, 4(1):37–74, 1999.

[23] D. Gawin, F. Pesavento, and B. A. Schrefler. Modelling of deformations of high strength concrete at elevated temperatures. *Materials and Structures/Materiaux et Constructions*, 37(268):218–236, 2004.

[24] D. Gawin, F. Pesavento, and B. A. Schrefler. Hygro-thermo-chemo-mechanical modelling of concrete at early ages and beyond. part i: hydration and hygro-thermal phenomena. *International Journal for Numerical Methods in Engineering*, 67(3):299–331, 2006. 10.1002/nme.1615.

[25] D. Gawin, F. Pesavento, and B. A. Schrefler. Hygro-thermo-chemo-mechanical modelling of concrete at early ages and beyond. part ii: shrinkage and creep of concrete. *International Journal for Numerical Methods in Engineering*, 67(3):332–363, 2006. 10.1002/nme.1636.

[26] D. Gawin, F. Pesavento, and B. A. Schrefler. Towards prediction of the thermal spalling risk through a multi-phase porous media model of concrete. *Computer Methods in Applied Mechanics and Engineering*, 195(41-43):5707–5729, 2006.

[27] D. Gawin, F. Pesavento, and B. A. Schrefler. Modelling creep and shrinkage of concrete by means of effective stresses. *Materials and Structures*, 40(6):579–591, 07 2007.

[28] M.G.D. Geers. Continuum damage mechanics: Fundamentals, higher-order theories and computational aspects. Lecture notes - course 4K060, 1998.

174

Bibliography

[29] T. Z. Harmathy. Thermal properties of concrete at elevated temperatures. *ASTM Journal of MAterials*, 5(1):47–74, 1970.

[30] R. W. Hyland and A. Wexler. Formulations for the thermodynamic properties of the saturated phases of h2o from 173.15k to 473.15k. *ASHRAE Trans*, 89(2A):500–519, 1983.

[31] L. Jason. *Relation endomanagement - perméabilité pour les bétons - application au calcul de structures*. PhD thesis, Ecole Centrale de Nantes, France, 2004.

[32] P. Kalifa, G. Chene, and C. Galle. High-temperature behaviour of hpc with polypropylene fibres: From spalling to microstructure. *Cement and Concrete Research*, 31(10):1487–1499, 2001.

[33] P. Kalifa, F.D. Menneteau, and D. Quenard. Spalling and pore pressure in hpc at high temperatures. *Cement and Concrete Research*, 30(12):1915–1927, 2000.

[34] T. Kelley. Flow through porous media. Technical report, North Carolina State University, 2004.

[35] G. A. Khoury. Strain of heated concrete during two thermal cycles. part 1: Strain over two cycles, during first heating and at subsequent constant temperature. *Magazine of Concrete Research*, 58(6):367–385, 2006.

[36] G. A. Khoury. Polypropylene fibres in heated concrete. part 2: Pressure relief mechanisms and modelling criteria. *Magazine of Concrete Research*, 60(3):189–204, April 2008.

[37] G. A. Khoury, B. N. Grainger, and P. J. E. Sullivan. Strain of concrete during 1st heating to 600-degrees-c under load. *Magazine Of Concrete Research*, 37(133):195–215, December 1985.

[38] G. A. Khoury, B. N. Grainger, and P. J. E. Sullivan. Transient thermal strain of concrete - literature-review, conditions within specimen and behavior of individual constituents. *Magazine Of Concrete Research*, 37(132):131–144, 1985.

Bibliography

[39] G. A. Khoury and C. E. Majorana. Spalling. In G. Khoury and C. E. Majorana, editors, *Effect of Heat on Concrete*, pages 1–11, Udine, 2003.

[40] G. A. Khoury, C. E. Majorana, F. Pesavento, and B. A. Schrefler. Modelling of heated concrete. *Magazine of Concrete Research*, 54(2):77–101, 2002.

[41] G. A. Khoury and B. Willoughby. Polypropylene fibres in heated concrete. part 1: Molecular structure and materials behaviour. *Magazine of Concrete Research*, 60(2):125–136, March 2008.

[42] L. J. Klinkenberg. The permeability of porous media to liquids and gases. *Drilling and Production Practice*, 1:200–211, 1941.

[43] V. K. R. Kodur and M. A. Sultan. Effect of temperature on thermal properties of high-strength concrete. *Journal of Materials in Civil Engineering*, 15(2):101–107, 2003.

[44] K. Kukla. Numerical analysis of selected concrete mechanic problems using a gradient damage model. Master's thesis, Cracow University of Technology, 2003.

[45] M. C. Leverett. Capillary behavior in porous solids. *Trans. AIME*, 142:152–169, 1941.

[46] R. W. Lewis and B. A. Schrefler. *The Finite Element Method in the Static and Dynamic Deformation and Consolidation of Porous Media*. Wiley, 2nd ed. edition, 1998.

[47] J. H. Lienhard IV and J. H. Lienhard V. *Heat transfer textbook*. Phlogiston Press, 2005.

[48] M. Mainguy, O. Coussy, and V. Boroghel-Bouny. Role of air pressure in drying of weakly permeable materials. *Journal of Engineering Mechanics*, 127(6):582–592, 2001.

[49] J. P. Monlouis-Bonnaire, J. Verdier, and B. Perrin. Prediction of the relative permeability to gas flow of cement-based materials. *Cement and Concrete Research*, 34(5):737–744, 2004.

Bibliography

[50] E. G. Navy. *Fundamentals of High Strength High Performance Concrete.* Longman, 1996.

[51] S. Nemat-Nassar and M. Mori. *Micromechanics: Overall properties of heterogeneous materials.* North-Holland, Elsevier Science Publishers, Amsterdam, The Netherlands, 1993.

[52] A. M. Neville. *Properties of Concrete.* Pearson Education, forth edition, 2007.

[53] C. Nielsen and N. Bicanic. Residual fracture energy of high-performance and normal concrete subject to high temperatures. *Materials and Structures*, 36(8):515–521, October 2003.

[54] C. V. Nielsen, C. J. Pearce, and N. Bicanic. Theoretical model of high temperature effects on uniaxial concrete member under elastic restraint. *Magazine of Concrete Research*, 54(4):239–249, 2001.

[55] C. V. Nielsen, C. J. Pearce, and N. Bicanic. Improved phenomenological modelling of transient thermal strains for concrete at high temperatures. *Computers & Concrete*, 1:189–209, 2004.

[56] NIREX. The-nirex-repository-concept: Evaluating-performance. Report-N-011, October 2000.

[57] C. J. Pearce, K. Kukla, N. Bicanic, and C.T. Davie. Modelling of transport processes in concrete at elevated temperatures - an alternative formulation for sorption isotherms. In G.Meshke, R. de Borst, H.Mang, and N.Bicanic, editors, *Computational Modeling of CONCRETE STRUCTURES*, Euro-C, pages 623–632. Proceedings of Euro-C 2006, 27-30 March 2006, Mayrhofen, Tirol, Austria, 2006.

[58] R. H. J. Peerlings, R. de Borst, W. A. M. Brekelmans, and M. G. D. Geers. Gradient-enhanced damage modelling of concrete fracture. *Mechanics Of Cohesive-Frictional Materials*, 3(4):323–342, October 1998.

[59] F. Pesavento. *Non-linear modelling of concrete as multiphase porous material in high temperature conditions.* PhD thesis, University of Padova, 2000.

[60] J.A. Purkiss. *Fire Safety Engineering Design of Structures.* Butterworth-Heinemann, 2nd edition edition, 2007.

[61] U. Schneider. *Properties of materials at high temperature, concrete.* RILEM Technical Committee 44-PHT, Technical University of Kassel, Germany, 2nd edition edition, 1986.

[62] U. Schneider and H. J. Herbst. Permeabilitaet und porositaet von beton bei hohen temperaturen. *Deutscher Ausschuss Stahlbeton*, 403:23–52, 1989.

[63] B. A. Schrefler, P. Brunello, D. Gawin, C. E. Majorana, and F. Pesavento. Concrete at high temperature with application to tunnel fire. *Computational Mechanics*, V29(1):43–51, 2002. 10.1007/s00466-002-0318-y.

[64] J. T. Stabler. *Computation Modelling of Thermo-Mechanical Damage and Plasticity in Concrete.* PhD thesis, The University of Queensland, 2000.

[65] R. T. Tenchev, L. Y. Li, and J. A. Purkiss. Finite element analysis of coupled heat and moisture analysis of coupled heat and moisture transfer in concrete subjected to fire. *Numerical Heat Transfer, Part A*, 39(7):685–710, 2001.

[66] S. Thelandersson. Modelling of combined therma and mechanical action in concrete. *Journal of Engineering Mechanics ASCE*, 113(6):893–906, 1987.

[67] F.-J. Ulm, O. Coussy, and Z. Bazant. The "chunnel" fire. i. chemoplastic softening in rapidly heated concrete. *J. Engrg. Mech. ASCE*, 125(3):272–282, 1999.

[68] M. Th van Genuchten. Closed-form equation for predicting the hydraulic conductivity of unsaturated soils. *Soil Science Society of America Journal*, 44(5):892–898, 1980.

[69] D. Whiting. Permeability of selected concretes. *ACI Special Publication*, 108:195–222, 1988.

Bibliography

[70] Wikipedia. Phase transition.

[71] M. Zeiml and R. Lackner. Experimental investigation on spalling mechanisms in heated concrete. In A. Carpinteri, P.G. Gambarova, G. Ferro, and G.A. Plizzari, editors, *Proceedings of the 6th International Conference on Fracture Mechanics of Concrete and Concrete Structures*, pages 1723–1728. Taylor & Francis, London, 2007.

[72] M. Zeiml, D. Leithner, R. Lackner, and H. A. Mang. How do polypropylene fibers improve the spalling behavior of in-situ concrete? *Cement and Concrete Research*, 36(5):929–942, 2006.

[73] B. Zhang, N. Bicanic, C. J. Pearce, and G. Balabanic. Residual fracture properties of normal- and high-strength concrete subject to elevated temperatures. *Magazine Of Concrete Research*, 52(2):123–136, April 2000.

[74] O. C. Zienkiewicz and R. L Taylor. *The Finite Element Method For Solid and Structural Mechanics*. Elsevier Butterworth-Heinemann, 2005.

List of Figures